

Simulation of Non-Equilibrium Quantum Dynamics in Monitored and Quenched Systems

Brian Jia Jiunn Khor

Petaling Jaya, Malaysia

MMathPhys, University of Oxford, 2018

*A Dissertation presented to the Graduate Faculty of the University of Virginia
in Candidacy for the degree of Doctor of Philosophy*

Department of Physics

UNIVERSITY OF VIRGINIA

April, 2025

Committee Members:

Israel Klich

Jeffrey Chi Yan Teo

Gia-Wei Chern

John Imbrie

Abstract

Understanding the interaction and dynamics of quantum many-body systems is a longstanding research interest that has led to numerous theoretical, experimental and technological advances. However, the quantum Hilbert space of quantum many-body systems scales exponentially with the number of degrees of freedom, making direct brute-force approaches intractable to understand the non-equilibrium quantum dynamics exhibited in these systems. Furthermore, the study of out-of-equilibrium quantum dynamics is further enriched by taking into account external interactions and manipulations on an otherwise closed quantum systems. In this dissertation, we investigate and simulate the non-equilibrium quantum dynamics of both closed and open quantum systems, where we study quenched dynamics in the former case, and the effect of quantum measurements for the latter case.

We first examine non-interacting fermionic lattice systems subject to quantum measurements (as well as other quantum operations such as particle injection). Repeated, periodic sequence of quantum measurements can induce effective new non-equilibrium dynamics in matter with chiral edge transport via measurement alone [1]. We consider the additional diffusion transport that is present in these systems with measurement-induced chiral transport, providing analytical and numerical treatments to describe these diffusive modes. In addition, we consider the effects of various types of disorder in these systems: site dilution, lattice distortion, and disorder in onsite chemical potential. In the quantum Zeno limit, the effective descriptions for the disordered measurement system with lattice distortions and random onsite potential can be modelled as a classical stochastic model, and the overall effect of increasing these disorders induces a crossover from perfect flow to zero transport. On the other hand if vacancies are present in the lattice the flow of particles per measurement cycle undergoes a percolation phase transition from unity to zero with percolation threshold $p_c \approx 0.26$, with critical exponent $\nu \approx 1.35$. We also present numerical results away

from Zeno limit and note that the overall effect of moving away from the Zeno effect is to reduce particle flow per cycle when the measurement frequency in our protocol is reduced.

In the second part of this thesis, we attempt to simulate quark confinement dynamics in low-dimensional systems by framing the problem in a condensed matter setting. More precisely, we provide an analogous description of quark confinement by studying the quenched dynamics of domain walls in the Mixed Field Ising Model. We explore the interplay of confinement, string breaking and entanglement asymmetry in this setting. First, we consider the evolution of an initial domain wall and show that, surprisingly, while the introduction of confinement through a longitudinal field typically suppresses entanglement generation, it can also serve to increase it beyond a bound set for free particles. Our model can be tuned to conserve the number of domain walls, which gives an opportunity to explore entanglement asymmetry associated with link variables. We study two approaches to deal with the non-locality of the link variables, either directly or following a Kramers-Wannier transformation that maps bond variables (kinks) to site variables (spins). We develop a numerical procedure for computing the asymmetry using tensor network methods and use it to demonstrate the different types of entanglement and entanglement asymmetry.

List of Publications

First-authored Publications discussed in this thesis:

1. **Khor, B.**, Wampler, M., Refael, G., Klich, I., Measurement-induced chirality: Diffusion and disorder. **Phys. Rev. B** 108, 214305, **2023** [2]
2. **Khor, B. J. J.**, Kürkçüoğlu, D. M., Hobbs, T. J., Perdue, G. N., Klich, I., Confinement and Kink Entanglement Asymmetry on a Quantum Ising Chain. **Quantum** 8, 1462, **2024** [3]

In addition, the following publication (second-author collaboration) will form many of the background materials for one of the chapters in this thesis:

1. Wampler, M., **Khor, B.**, Refael, G., Klich, I., Stirring by Staring: Measurement Induced Chirality. **Phys. Rev. X** 12, 031031, **2022** [4]

Additional preprints completed during PhD study (not discussed in this thesis):

1. Swain, N., Tang, H. -K., Foo, D. C. W., **Khor, B. J. J.**, Lemarié, G., Assaad, F. F. Assaad, Sengupta, P., Adam, S., Engineering many-body quantum Hamiltonians with non-ergodic properties using quantum Monte Carlo, arXiv:2106.08587 [5]

Acknowledgements

First of all, I would like to thank my PhD supervisor Israel Klich for his support and supervision throughout my graduate study. Israel is one of the most accommodating and smart scientists I have ever met in my time as a Ph.D. student. His intuition in discerning core problems in problem solving has greatly benefited me whenever I am stuck in problem solving. He has also given me freedom to pursue other collaborations during my Ph.D. and allowed me to become a different type of physicist from him (with him being analytical and me being numerical) while complementing each other in problem solving. He is also tremendously kind, especially when he allowed me to work remotely and stay with my wife in New Haven during the final 1.5 years of my Ph.D. when my apartment in Charlottesville was flooded during a winter storm.

I also extend my gratitude to Jeffrey Teo for our extensive collaboration in the early years of my Ph.D. He has taught me bosonization, conformal field theory, and coupled wire approach to model strongly correlated systems early on in my Ph.D. Though I end up becoming a numerical (tensor network) physicist, I believe these skill sets will be useful down the line of my career. I also would like to thank Benjamin Wieder, Yichen Hu, Meng Hua, and Jeffrey Teo for our ongoing collaboration on the higher order topological insulator project.

The next team of collaborators I would like to thank includes Doğa Murat Kürkcüoğlu and Gabriel Perdue from the Superconducting Quantum Materials and Systems (SQMS) Center at Fermilab, and Timothy Hobbs from Argonne National Lab for collaboration on the confinement project. I would like to especially thank Gabriel Perdue for hosting and hiring me as a visiting graduate researcher at Fermilab for 6 months of my Ph.D. and his financial support during those 6 months in 2023.

I would also like to thank the T4 Condensed Matter and Quantum Computing Division of the Los Alamos National Laboratory for hosting me during the Quantum

Computing Summer School in 2024 for 10 weeks. My gratitude is extended especially to Lukasz Cincio and Paolo Braccia for ongoing collaboration developing two dimensional PEPS algorithm to simulate various quantum simulation experiments. I learned many things from Lukasz's intuition in numerical problems and his extensive expertise in tensor network specifically, and Paolo for his expertise in many coding practices to tackle intensive numerical problems.

Next, I would like to thank my peers at the University of Virginia. I would like to thank Matthew Wampler, my senior graduate student in Israel's group, for 2 collaborations on measurement-induced chirality. I would like to thank Akin Morrison, Lingyu Yang, Supriyo Ghosh, Youjian Chen, Matthew Walker, Saikat Bera, and my apartment roommates Ephraiem Sarabamoun and Diego Ibarra, for friendships, many conversations and laughters in my Ph.D. study.

I would like to thank my family members back in Malaysia. To my Dad Heng Chiew and my mom Yee Neo, I owe my deepest gratitude for raising me up despite many financial hardship you face in raising 3 boys in the capital city of Malaysia. To my elder brother David and younger brother Joel, I also cherish the time we grew up together before I left Malaysia for my undergrad and grad school.

Another acknowledgement will be due to my father-in-law, Yiwen Sun, and my mother-in-law, Yan Qi Han, in China, for giving their daughter in marriage to me. Last but not least, I would like to thank my wife Zekun Sun, whom I met during my Ph.D. study here in the US. Her encouragement, support and love has supported me through the toughest times of my Ph.D., especially when I feel discouraged during the initial phase of my postdoc and job search. Her wisdom to handling difficult situations and her faith has greatly supported and motivated me to press on in hardships, and I am a much happier person thanks to her! I love you, Zekun!

Contents

Abstract	ii
List of Publications and Preprints	iv
Acknowledgements	v
1 Introduction	1
1.1 Quantum Engineering and Quantum Dynamics	1
1.2 Open Quantum Systems	3
1.3 Confinement as Quenched Dynamics	7
1.4 Entanglement Asymmetry	10
1.5 Tensor Network Algorithm	15
1.5.1 Tensor Network Notation and Singular Value Decomposition	15
1.5.2 Matrix Product States and Schmidt Decomposition	18
1.5.3 Time-Evolving Block Decimation	24
2 Measurement Induced Chirality: Diffusion and Disorder	29
2.1 Introduction	29
2.2 Measurement Induced Chirality Protocol	32

2.3	Measurement induced diffusion	38
2.4	Site dilution and Percolation Threshold	43
2.4.1	Perfect swapping Case: Percolation Threshold	44
2.4.2	Away from Perfect swapping: Crossover	46
2.5	Lattice Distortion and Onsite Potential disorder	48
2.6	Numerical Results Away from Zeno Limit	54
2.7	Discussions and Outlook	56
	Appendix	58
2.A	Derivation for the analytical expression for the Diffusion constant	58
2.B	Extraction of the late time dynamics of the mean flow per cycle on a finite size lattice	62
2.C	Derivation of the stochastic transition matrix for the random onsite potential disorder	63
3	Confinement and Kink Entanglement Asymmetry on a Quantum Ising Chain	67
3.1	Introduction	67
3.2	Model and Entanglement Measures	68
3.3	Kink-preserving Dynamics	70
3.4	Rényi Entropy saturation, integrability and confinement	71
3.4.1	The effect of confinement and integrability breaking	73
3.5	Entanglement Asymmetry	74
3.5.1	Kink and Kramers-Wannier Entanglement Asymmetries	76
3.5.2	MPS implementation	79

3.6	Kramers-Wannier Unitary Transformation and the XY Model	82
3.7	Numerical results	84
3.8	Conclusion and Outlook	87
Appendix		89
3.A	Benchmarking exact diagonalization, two-kink dynamics and tensor network simulations	89
3.B	Construction of the reduced density matrix in the Two-Kink Subspace .	92
3.C	Rényi Entropy Evolution and Collisions: Early time and Entropy bound violation with large system size	96
3.D	Computational Complexity of the MPS Implementation	99
3.E	Upper bound on Rényi Entropy for $h = 0$ and kink-number preservation.	100
4	Conclusion	103
	Bibliography	105

Soli Deo Gloria

Chapter 1

Introduction

1.1 Quantum Engineering and Quantum Dynamics

Over the past few decades, numerous advances have been made in understanding novel phases of matter arising from quantum mechanical interactions of atoms and electrons. This has led to many important discoveries on various quantum states of matter, such as the Bose-Einstein condensations [6], high-temperature superconductivity [7], and topological phases of matter [8], with the promise to revolutionize the next generation of quantum technologies in areas such as quantum computing [9]. These important discoveries also serve as a feedback loop to further galvanize new theoretical ideas, inspire developments in powerful computational and numerical techniques, and open up new avenues for experimental efforts to help understand new emergent quantum phenomena and dynamics. These new developments have made it possible not only to investigate and prepare new quantum states of matter but also to provide external control over quantum many-body systems. This provides the possibility to not only simulate and probe quantum dynamics in closed quantum many-body systems, but also to engineer new quantum dynamics in open quantum systems by external manipulations such as quantum measurements.

Conventional methods to understand emergent behavior of quantum materials

have mostly been focused on isolated systems near equilibrium [10], and the number of numerical and analytical toolkits available to tackle non-equilibrium quantum dynamics and behavior is far more restrictive. Understanding out-of-equilibrium quantum dynamics in both closed and open quantum systems poses great theoretical and numerical challenges due to the exponential scaling of the dimension of the Hilbert space with respect to physical degrees of freedom (such as the number of qubits, spins, etc). Numerous theoretical and computational tools have been developed over the years to help simulate these dynamics in both closed and open quantum systems. In this chapter, we will introduce some of the theoretical formalisms and numerical tools that are relevant to the non-equilibrium systems of interest, namely, free fermionic lattice under periodic measurements [1, 2], and quenched dynamics of the quantum Ising chain [3]. We will also provide pedagogical introductions by giving various background materials relevant to the subsequent chapters in this dissertation.

In chapter 2, we consider diffusion and the effect of disorder in free fermionic systems under periodic measurements. This open quantum system setting requires theoretical tools developed from the Lindbladian formalism to deal with density matrices, and a great simplification arises when we consider a subset of Krauss operators that close the hierarchy on the two-point correlation function [11]. The tools will be introduced in Sec 1.2 below. The closed hierarchy formalism will be needed to describe various aspects of the measurement-induced chirality in chapter 2.

Chapter 3 will then investigate confinement and entanglement dynamics in a quantum Ising chain. The problem of understanding quark confinement dynamics and quantum chromodynamics is notoriously difficult due to asymptotic freedom at low energy effective field theory of these systems. This provides a motivation to study the problem of confinement in a low-dimensional, condensed matter analogue system, and we discuss this in Sec 1.3.

After introducing the basic motivation behind using quantum Ising chain as a toy

model to study low-dimensional confinement, we will proceed to introduce an aspect of quantum entanglement that has been hotly researched in the last two years, namely, the entanglement asymmetry [12]. We will discuss the motivation behind the entanglement asymmetry, give an intuition about what this quantity represents, and briefly mention the quantum Mpemba effect as a recent quantum dynamical phenomena that is observed in the setting of entanglement asymmetry.

Finally, we will introduce the tensor network algorithm [13, 14] as a powerful numerical tool to tackle our quenched dynamics of interest in Sec 1.5. We will focus primarily on the matrix product states (MPS) and time evolving block decimation (TEBD) algorithm as a classically efficient method of simulating quantum many-body systems in one dimension. The key idea behind tensor network algorithms is to approximate the target quantum state by throwing away degrees of freedom encoded in the quantum state that will not introduce significant errors in the simulations. More details about how tensor network works will be provided in Sec 1.5 below.

For ease of presentation, each chapter contains the main results and ideas in its body with many of the technical details included in the corresponding appendix.

1.2 Open Quantum Systems

In a closed quantum system, the quantum state $|\psi\rangle$ with is typically described by a statevector of dimension \mathbb{C}^{Nd} , where d is the dimension of each degrees of freedom and N is the total number of physical degrees of freedom (for a spin-1/2 or a qubit, $d = 2$). Its time evolution given a Hamiltonian H is typically described by a unitary evolution $U = \exp(-iHt)$ of dimension $\mathbb{C}^{Nd} \times \mathbb{C}^{Nd}$ for real time evolution $t \in \mathbb{R}$.

Dealing with open quantum systems typically involves non-unitary operations acting on our quantum state, and these operations can arise from various sources, such

as system-environment interactions, quantum measurements, etc. The general way to describe a quantum state in an open quantum system is given by a density matrix $\rho = \sum_k p_k |\psi_k\rangle\langle\psi_k|$, where $\{\psi_k\}$ is an orthonormal basis spanning the quantum state space and p_k is classical probability that sums to 1. The general evolution of density matrices can be described using the Krauss operator formalism

$$\rho \longrightarrow \mathcal{L}(\rho) = \sum_{\nu} A_{\nu} \rho A_{\nu}^{\dagger}; \quad \sum_{\nu} A_{\nu}^{\dagger} A_{\nu} = 1. \quad (1.1)$$

This form ensures that ρ remains non-negative (i.e., its eigenvalues are not negative, or equivalently $\langle\psi|\rho|\psi\rangle \geq 0$ for any statevector $|\psi\rangle$) and the normalization condition on the Kraus operators A_{ν} preserves $\text{Tr}\{\rho\} = 1$. We will refer readers for more in-depth discussions on open quantum systems in [15].

Explicitly working in the general Krauss operator formalism is often intractable, and one typically imposes certain restrictions or approximations to make the Krauss operator formalism more tractable. A popular choice is to use the Lindblad formalism, with the basic assumptions that (1) the system is weakly coupled to the bath (environment), and (2) the time scales for dynamics in the bath and the bath-system coupling are both much faster than the typical time scales for evolution in the system itself. Under these assumptions, it is possible to make the Markovian approximation to simplify the Krauss map on ρ into the Lindblad form. We refer interested readers to the excellent Preskill's lecture notes [16] for more details. The system is then Markovian and has no memory of the state of the system from the distant past, and this in turns imply that the density matrix $\rho(t + \delta t)$ can be written completely in terms of the density matrix $\rho(t)$ for short time interval δt . The evolution of the density matrix can then be written as a first order linear differential equation (known as the Lindblad master equation) with respect to time t .

In this dissertation, however, we will introduce another approach that is more

relevant to our problem in Chapter 2. We will restrict ourselves to a class of Krauss operators where dynamics is more tractable but still exact [11]. To motivate the class of dynamics that is relevant to our discussion, we first look at the evolution of a general correlation function

$$\left\langle a_{i_1}^\dagger \dots a_{i_{\ell_1}}^\dagger a_{i_{(\ell_1+1)}} \dots a_{i_{(\ell_1+\ell_2)}} \right\rangle = \text{Tr} \left\{ \rho a_{i_1}^\dagger \dots a_{i_{\ell_1}}^\dagger a_{i_{(\ell_1+1)}} \dots a_{i_{(\ell_1+\ell_2)}} \right\} \quad (1.2)$$

given by

$$\begin{aligned} \left\langle a_{i_1}^\dagger \dots a_{i_{\ell_1}}^\dagger a_{i_{(\ell_1+1)}} \dots a_{i_{(\ell_1+\ell_2)}} \right\rangle &\longrightarrow \left\langle a_{i_1}^\dagger \dots a_{i_{\ell_1}}^\dagger a_{i_{(\ell_1+1)}} \dots a_{i_{(\ell_1+\ell_2)}} \right\rangle \\ &+ \sum_{\nu} \text{Tr} \left\{ \rho A_{\nu}^\dagger \left[a_{i_1}^\dagger \dots a_{i_{\ell_1}}^\dagger a_{i_{(\ell_1+1)}} \dots a_{i_{(\ell_1+\ell_2)}} \right], A_{\nu} \right\} \end{aligned} \quad (1.3)$$

where we have used the normalization condition of A_{ν} , i.e., $\sum_{\nu} A_{\nu}^\dagger A_{\nu} = 1$. The $\ell_1 + \ell_2$ correlation function is, in general, taken to a higher-order correlation function by this evolution, leading to a hierarchy of equations which quickly becomes intractable. However, a subset of this general evolution can be found by considering just the two-point function $G_{ij} \equiv \langle a_i^\dagger a_j \rangle$, and asking under what set of Krauss operators does the hierarchy close, i.e., what set of Krauss operators map two-point functions to two-point (and not higher) correlation functions $G \rightarrow G' = \mathcal{K}(G)$.

In [11], it is shown that, for fermions on a lattice, the following Krauss operators form a set of possible operations that close the hierarchy on the two point function

level:

$$\text{Non-interacting Evolution:} \quad \mathcal{L}_u(\rho) = \mathcal{U}\rho\mathcal{U}^\dagger \quad (1.4a)$$

$$\text{Particle Detection:} \quad \mathcal{L}_{D,i}(\rho) = n_i\rho n_i + (1 - n_i)\rho(1 - n_i) \quad (1.4b)$$

$$\begin{aligned} \text{Soft Particle Injection:} \quad \mathcal{L}_{in,i,\epsilon}(\rho) &= \epsilon(2 - \epsilon)a_i^\dagger\rho a_i \quad (1.4c) \\ &+ (1 - \epsilon(1 - n_i))\rho(1 - \epsilon(1 - n_i)) \end{aligned}$$

$$\begin{aligned} \text{Soft Particle Extraction:} \quad \mathcal{L}_{out,i,\epsilon}(\rho) &= \epsilon(2 - \epsilon)a_i\rho a_i^\dagger \quad (1.4d) \\ &+ (1 - \epsilon n_i)\rho(1 - \epsilon n_i) \end{aligned}$$

Here, ϵ is a real number between 0 and 1 and \mathcal{U} describes the non-interacting evolution under which fermionic operators transform as $\mathcal{U}^\dagger a_i^\dagger \mathcal{U} = U_{ij} a_j^\dagger$, where U is called a single-particle evolution. We can then compute the corresponding transformations on the two point function by applying the anti-commutation relations of a^\dagger, a :

$$\text{Non-interacting Evolution:} \quad \mathcal{K}_U(G)_{ij} = (UGU^\dagger)_{ij} \quad (1.5a)$$

$$\text{Particle Detection:} \quad \mathcal{K}_{D,i}(G) = P_i G P_i + (1 - P_i) G (1 - P_i) \quad (1.5b)$$

$$\text{Soft Particle Injection:} \quad \mathcal{K}_{in,i,\epsilon}(G) = (1 - P_i) G (1 - P_i) \quad (1.5c)$$

$$\begin{aligned} &+ (1 - \epsilon) P_i G (1 - P_i) + (1 - \epsilon)(1 - P_i) G P_i \\ &+ (1 - \epsilon)^2 P_i G P_i + \epsilon(2 - \epsilon) P_i \end{aligned}$$

$$\text{Soft Particle Extraction:} \quad \mathcal{K}_{out,i,\epsilon}(G) = \mathcal{K}_{in,i,\epsilon}(G) - \epsilon(2 - \epsilon) P_i \quad (1.5d)$$

Here, $P_i = |i\rangle\langle i|$ is the (single particle) projector onto site i .

We emphasize that no approximations are used in the derivation of Eq. (1.5). Great simplification arises due to the restricted set of Krauss operations allowed in our consideration. If we are only interested in transport or particle density properties of a system which may be written completely in terms of the two-point function, the closed-hierarchy formalism thus allows for the exact solution of the dynamics via a function

which scales polynomially (the two-point function) instead of a function which scales exponentially (the density matrix) in system size. We will use the closed hierarchy formalism in the the next chapter and study the particle flow in an open system subject to non-interacting evolution and particle detection.

1.3 Confinement as Quenched Dynamics

In this section, we will provide the motivation to simulate confinement in condensed matter physics setting. The phenomenon of low-energy quantum chromodynamics (QCD) in three dimension is difficult to understand due to the phenomenon of asymptotic freedom in 3-dimensional non-Abelian gauge field theory exhibiting QCD [17–19]. Roughly speaking, when a field theory flows from its high-energy, ultraviolet limit to its low-energy, infrared limit in a renormalization group sense, the coupling strengths in the non-Abelian gauge field theory describing QCD and confinement in quarks also grow in this instance. This makes the phenomenon of quark confinement and QCD highly non-perturbative at low-energy scales, and hence difficult to treat analytically in its native, field theoretic setting.

One approach to get around the analytical difficulty of simulating and understanding the low-energy dynamics and physics of the non-Abelian gauge field theory is to write down discrete version of the non-Abelian gauge theory by putting it on a lattice. This effort was initially spearheaded by Kogut and Susskind and one of the earliest models in the study of lattice gauge theory is the Kogut-Susskind Hamiltonian [20, 21]. Lattice gauge theories then provide toy models platforms to tackle the problem of QCD and confinement using numerical simulations.

In this vein, the simplest lattice gauge theory that one could study is the \mathbb{Z}_2 lattice gauge theory. One famous example of the \mathbb{Z}_2 lattice gauge theory is the Kitaev Toric

code model [22]. However, in this dissertation, we will consider another famous condensed matter toy model that, while not considered strictly a \mathbb{Z}_2 lattice gauge theory, nonetheless mimics many aspects of the confinement dynamics in QCD in low dimension.

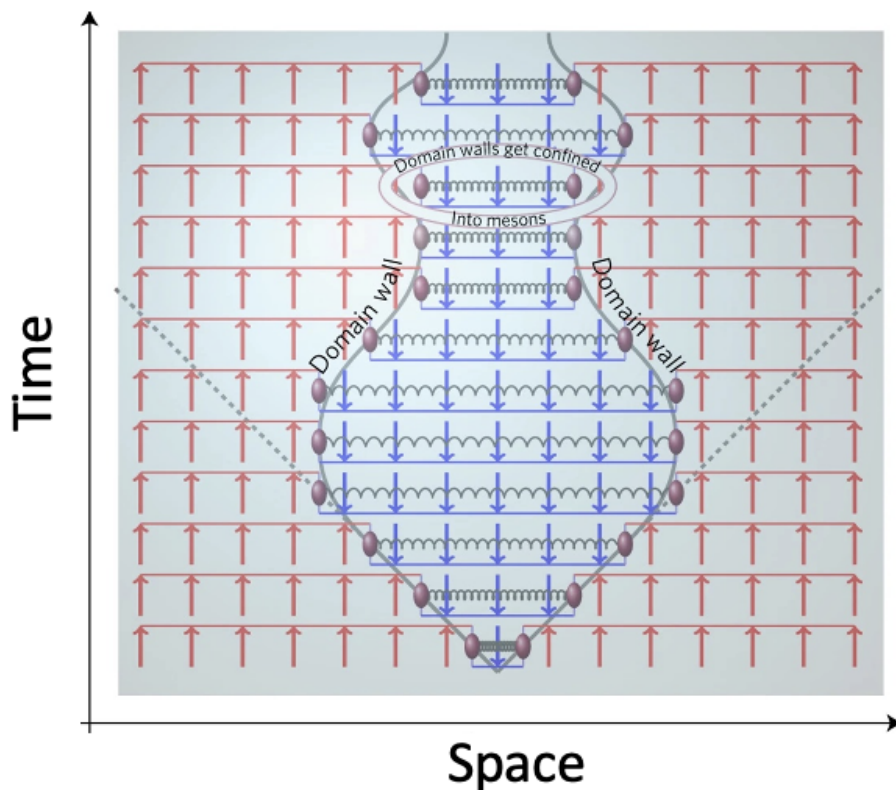


FIGURE 1.1: Two counter-propagating domain walls bounce back and forth due to the confining potential. Figure is taken from [23].

We will consider the Mixed Field Ising model (MFIM), and in chapter 3, we will add an additional three-body spin interaction term. For pedagogical reason, however, we will consider the simpler version of the problem, with the following one-dimensional MFIM on an open spin chain

$$H = -J_0 \sum_{i=1}^{L-1} \sigma_i^z \sigma_{i+1}^z - g \sum_{i=1}^L \sigma_i^x - h \sum_{i=1}^L \sigma_i^z. \quad (1.6)$$

To simulate confinement dynamics in the Ising model setting, one will turn the problem to a quantum quenched dynamics problem, an approach that is spearheaded in [23]. In this setting, mesons (a composite particle of a quark and an anti-quark) is represented by a domain wall/kink in the Ising spin chain, i.e., by a spin slip $|\dots \uparrow \downarrow \dots\rangle$ in the spin chain. We will initialize a chain of spin-1/2 system with the following initial state, representing two mesons with two domain walls:

$$|j, n\rangle = |\uparrow_1 \dots \uparrow_{j-1} \downarrow_j \dots \downarrow_{j+n-1} \uparrow_{j+n} \dots \uparrow_L\rangle. \quad (1.7)$$

Although a detailed treatment of the semi-classical treatment will not be discussed in this Introduction, a rough physical description will be given to help the readers understand the physics behind confinement of the domain wall dynamics. The longitudinal field terms with coupling strength h acts to confine the propagation of the domain walls, which is illustrated in the semi-classical picture in Fig 1.1.

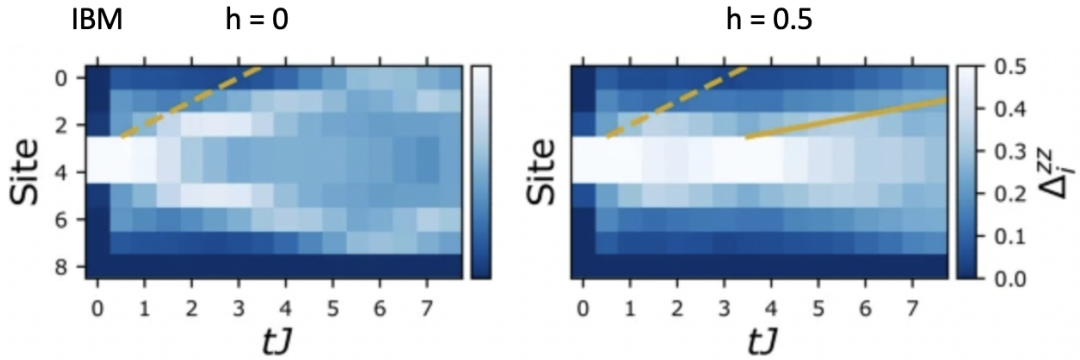


FIGURE 1.2: Time evolution of probability dynamics of kinks simulated on real IBM superconducting qubits, without ($h = 0$, Left) and with ($h = 0.5$, Right) confining potential. The yellow dashed and solid lines are added to display the propagating velocity of the domain walls, and introducing confining field reduces the propagation velocity in the IBM quantum simulation experiment. Figure is taken from [24].

We can understand this more systematically in the following way. Consider the two-kink projection of the Hamiltonian in Eqn 1.3, $H_2 = P^{-1}HP$, for basis written in

Eqn 1.3 $|j, n\rangle$, the two-kink subspace of the MFIM can be written as [24]

$$H_2 = \sum_{\substack{0 \leq j < L-1 \\ 0 < n < L-j-1}} 2hn|j, n\rangle\langle j, n| - g\left(|j-1, n+1\rangle + |j+1, n-1\rangle + |j, n-1\rangle + |j, n+1\rangle\right)\langle j, n|. \quad (1.8)$$

Within the two-kink subspace (polynomially large) of the exponentially large Hilbert space, this projected two-kink Hamiltonian then displays more clearly that the longitudinal term acts as a confining potential that increases with the separation distance of the domain wall.

This confinement dynamics has also been demonstrated recently on real, noisy IBM quantum superconducting qubits [24]. In Fig 1.2, 10 qubits are selected to initialize a two domain wall states $|\uparrow\uparrow\uparrow\uparrow\downarrow\downarrow\uparrow\uparrow\uparrow\rangle$. One then runs through trotterized time evolution to evolve the qubits to simulate the quenched dynamics of the domain wall propagations.

With both theoretical investigation and quantum simulation experiments demonstrating the confinement dynamics of domain walls in MFIM, we will proceed to introduce other background ideas, namely, the concepts of entanglement asymmetry and tensor network algorithms, in the remaining sections of this chapter.

1.4 Entanglement Asymmetry

In this section, we will introduce the motivation and concept of entanglement asymmetry to familiarize the readers for many of the contents in Chapter 3. Background materials in this chapter will be based on pioneering works by Klich and Levitov [25] and Ares *et. al.* [12].

The motivation to formulate the concept of the entanglement asymmetry arises from the motivation to understand the effect of symmetry and conservation laws on

the amount of entanglement generated in a quantum many-body system. In Klich and Levitov [25], the authors explore the constraint particle number conservation imposes on the amount of entanglement entropy one can measure a fermionic system when one is restricted to detect entanglement with local experimental probes. This motivates further study on the relation between conservation laws and entanglement entropy, and Ares *et. al.* proposes the notion of entanglement asymmetry in their recent work to quantify this connection more clearly [12].

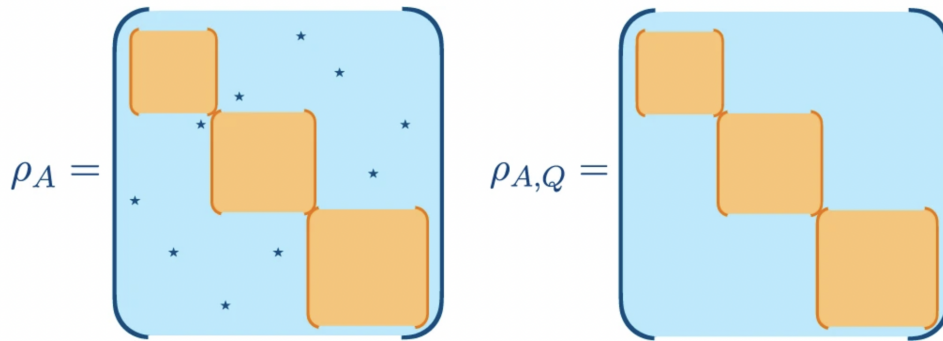


FIGURE 1.3: In the eigenbasis of the subsystem charge Q_A , the action of projector Π_q projects the density matrix ρ_A onto the eigenspace of Q_A with integer eigenvalue $q \in \mathbb{Z}$. This results in the elimination of off-diagonal charge sector blocks with different charge eigenvalues q . The entanglement asymmetry is then the difference in entanglement entropies from these density matrices. Figure is taken from [12].

We define the entanglement asymmetry as the difference between the entropy arising from symmetry-projected reduced density matrix $\rho_{A,Q}$ and the entropy from regular reduced density matrix ρ_A [12]

$$\Delta S_A^{(n)} \equiv S^{(n)}(\rho_{A,Q}) - S^{(n)}(\rho_A). \quad (1.9)$$

with the entanglement entropies defined by

$$S^{(n)}(\rho_A) = \frac{1}{1-n} \log(\text{Tr}(\rho_A^n)). \quad (1.10)$$

Here, the symmetry-projected reduced density matrix is defined by

$$\rho_{A,Q} = \sum_{q \in \mathbb{Z}} \Pi_q \rho_A \Pi_q, \quad (1.11)$$

where the density matrices are illustrated in the eigenbasis of subsystem charge operator Q_A in Fig 1.3. In numerical simulation, it will be more expedient to use the following form of the symmetry-projected reduced density matrix

$$\rho_{A,Q} = \int_{-\pi}^{\pi} \frac{d\alpha}{2\pi} e^{-i\alpha Q_A} \rho_A e^{i\alpha Q_A}. \quad (1.12)$$

In practice, the integration is carried out by using various numerical method, for example, the trapezoidal rule, to approximately projects out the off-diagonal symmetry sectors, and this will be used in Chapter 3.

A few remarks are in order on the entanglement asymmetry. First of all, the entanglement asymmetry is a measure of explicit symmetry breaking and not spontaneous symmetry breaking. In the conventional quantum phase transition and condensed matter settings, order parameters are used to detect phase transition and spontaneous symmetry breaking [10]. The entanglement asymmetry should not be understood in this sense. Rather, in a very rough physical sense, it is an entanglement measure that quantifies the distance of our quantum state to the nearest symmetric quantum state (with respect to some charge Q).

Another remark is that the quantity $\Delta S_A^{(n)}$ can be shown to possess 2 properties that allow it to quantify explicit symmetry breaking. (1) $\Delta S_A = \lim_{n \rightarrow 1} \Delta S_A^{(n)} = \text{Tr}(\rho_{A,Q} \log \rho_{A,Q} - \rho_A \log \rho_A) = \text{Tr}(\rho_A (\log \rho_{A,Q} - \log \rho_A)) \geq 0$ is non-negative [26]. This can be seen most easily in the case of $\Delta S_A = \lim_{n \rightarrow 1} \Delta S_A^{(n)}$, although in the more general case treatment $\Delta S_A^{(n)} \geq 0$ has also been made in [12]. (2) $\Delta S_A^{(n)} = 0$ if and only if the state is symmetric with respect to the subsystem charge operator Q_A , and ρ_A is block diagonal in the eigenbasis of Q_A and $\rho_A = \rho_{A,Q}$.

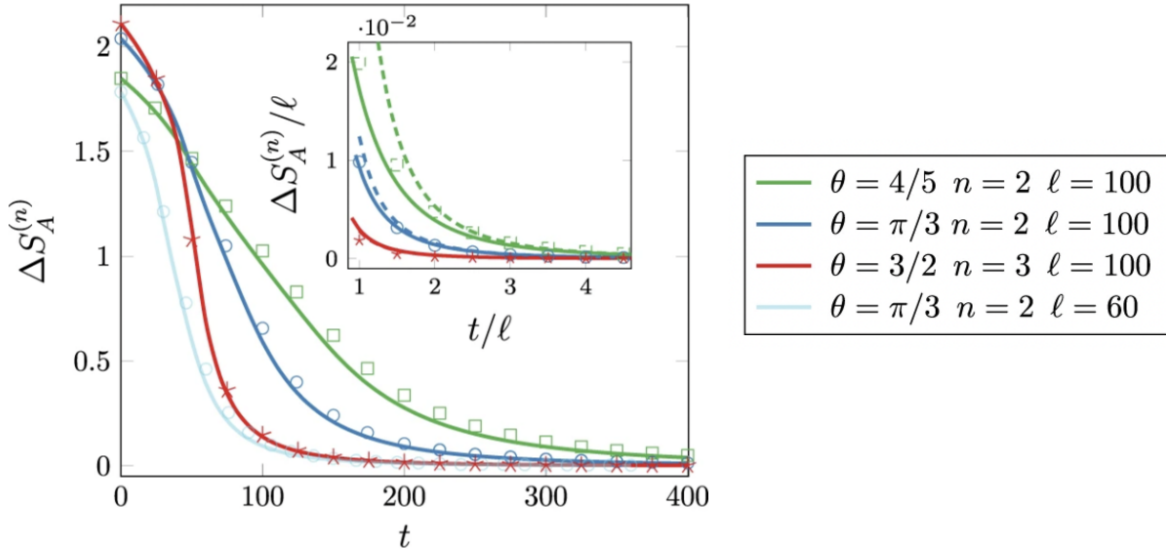


FIGURE 1.4: The symbols are the numerical results for various values of the subsystem length l , the replica index n (for n -th order entanglement asymmetry), and the initial tilting angle θ . The continuous lines are our prediction obtained from analytical calculations obtained in [12]. The inset displays the asymptotic behaviors from analytical predictions for large $t/$.

Figure is taken from [12].

An interesting phenomenon made manifest by the entanglement asymmetry is the quantum Mpemba effect [12]. Roughly speaking, the quantum Mpemba effect is a counter-intuitive phenomenon in which the more a quantum state initially breaks a symmetry, the faster the symmetry is restored when the quantum state evolves under the real time evolution of a Hamiltonian that preserves the symmetry. We will briefly illustrate this with an example from [12].

In [12], consider the initial *cat* state of the following form

$$|\Psi(0)\rangle = \frac{|\theta; \nearrow \nearrow \dots\rangle - |-\theta; \nearrow \nearrow \dots\rangle}{\sqrt{2}}, \quad (1.13)$$

where the states in superposition is understood to be the tilted ferromagnetic product state of an infinite spin chain of the following form (not aligned in the z -axis)

$$|\theta; \nearrow \nearrow \dots\rangle = e^{-i\frac{\theta}{2}\sum_j \sigma_j^z} |\uparrow\uparrow \dots\rangle. \quad (1.14)$$

For $\theta \neq \pi m$, $m \in \mathbb{Z}$, this tilted ferromagnetic product state in Eqn 1.4 (and also the cat version of the state in Eqn 1.4) breaks the $U(1)$ symmetry associated to the conservation of the total z -axis magnetization $Q = \frac{1}{2}\sum_j \sigma_j^z$.

The state in Eqn 1.4 is then evolved under the quenched dynamics according to

$$|\Psi(t)\rangle = e^{-iHt}|\Psi(0)\rangle, \quad (1.15)$$

where our Hamiltonian of interest is the symmetric XX Hamiltonian preserving the total z -axis magnetization, $[H, Q] = 0$,

$$H = -\frac{1}{4} \sum_{j=-\infty}^{\infty} \left[\sigma_j^x \sigma_{j+1}^x + \sigma_j^y \sigma_{j+1}^y \right]. \quad (1.16)$$

We now look at the quantum Mpemba effect by observing the relaxation behaviour of initial quantum states $|\Psi(0)\rangle$ with various tilt angles θ in Fig 1.4. We will focus on the main Figure and not the inset since we are interested at how rapidly the total magnetization symmetry Q is restored for various initial cat states Eqn 1.4 breaking the total magnetization symmetry. In Fig 1.4, we notice that for the same $n = 2$ comparison, the state with higher entanglement asymmetry ΔS_A^2 relaxes to zero more quickly than the state with lower entanglement asymmetry ΔS_A^2 . This counterintuitive phenomenon, occurring in this example and also other examples (see, for instance, [27]), is called the quantum Mpemba effect, and this effect is illustrated effectively when we define a symmetry breaking entanglement measure (the entanglement asymmetry) to quantify and illustrate this effect. Recent trapped ion quantum simulation experiment

has also demonstrated the quantum Mpemba effect [28]. For our dissertation, however, we will not look into the quantum Mpemba effect, but use it merely to motivate the study of entanglement asymmetry itself.

1.5 Tensor Network Algorithm

We now turn to our final ingredient required to understand the materials in this thesis, namely the tensor network algorithms, in this section. We will introduce the matrix product state (MPS) as a way to efficiently represent one-dimensional quantum state, and the time evolving block decimation (TEBD) algorithm as an approximation to apply the Trotterized time evolution of the Hamiltonian to our MPS. Tensor network algorithms introduced here will be used in Chapter 3.

Tensor network algorithms are a class of classically efficient approaches to represent and simulate quantum many-body systems. Writing up a thorough introduction to the vast literature and background of the available tensor network algorithms will be a daunting task, so we will only skim through the bare minimum needed to understand the small subset of tensor network approaches needed to understand Chapter 3 in this dissertation. We refer interested readers to [13, 14] for more in-depth introductions to tensor network theory.

1.5.1 Tensor Network Notation and Singular Value Decomposition

We begin by introducing the tensor network notation and the basic ingredient behind the tensor network compression schemes: the singular value decomposition (SVD). In tensor network notation, a scalar is represented by a block without any tensor leg, while the number of legs of a tensor represents the rank of a tensor. This is best visualized in Fig 1.5 below. The introductory note in this subsection is taken largely from [13].

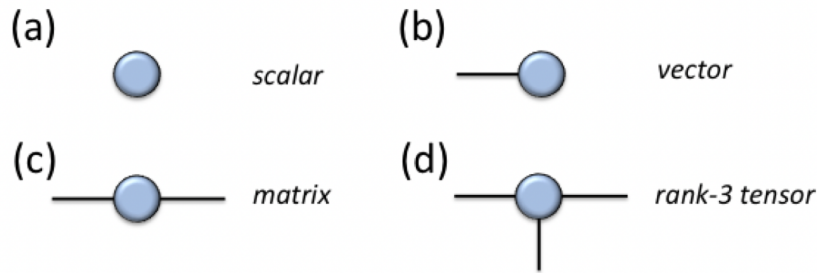


FIGURE 1.5: (a) A scalar, (b) a vector, (c) a matrix, and (d) a rank-3 tensor in tensor network notation. Figure is taken from [14].

In tensor network notation, a leg connecting two tensors represents a tensor contraction, with the shared index representing the connecting/common leg of the 2 tensors. In this notation, taking a trace of a matrix involve connecting 2 legs of a matrix in a loop. A summary of useful tensor network notations for tensor contraction is illustrated in Fig 1.6 below.

Figure 1.6 illustrates various tensor contractions: (a) Matrix-like contractions: a matrix (green circle) with legs i and j contracted with a vector (purple circle) with leg j yields $\sum_j M_{ij} v_j$; a matrix (green circle) with legs i and j contracted with another matrix (orange circle) with legs j and k yields $A_{ij} B_{jk} = AB$; a matrix (green circle) with legs i and j contracted with another matrix (red circle) with legs j and i yields $A_{ij} B_{ji} = \text{Tr}[AB]$. (b) Tensor contraction with more than 2 legs: a matrix (blue circle) with legs i and j contracted with a rank-3 tensor (green circle) with legs j , l , and k yields $\sum_j M_{ij} N_{jkl}$. (c) More convoluted tensor contractions: a rank-3 tensor (blue circle) with legs i , j , and k contracted with another rank-3 tensor (red circle) with legs k , l , and m yields $\sum_k T_{ijk} V_{klm}$; a chain of four tensors (blue, green, red, blue) with legs $\alpha_1, \alpha_2, \alpha_3$ at the ends yields $\sum_{\alpha_1, \alpha_2, \alpha_3} A_{\alpha_1}^{s_1} B_{\alpha_1 \alpha_2}^{s_2} C_{\alpha_2 \alpha_3}^{s_3} D_{\alpha_3}^{s_4}$.

FIGURE 1.6: (a) Matrix-like contractions involving a single leg connection between tensors with at most two legs (matrices). Here, the top figure represents a matrix-vector contraction, the middle figure represents a matrix-matrix multiplication, and the bottom figure represents taking the trace from the resulting matrix. (b) and (c) show tensor contractions involving contractions between tensors with more than 2 legs. (b) illustrates the indices written out on tensor legs more explicitly. The top and bottom figures in (c) represents more convoluted tensor contractions.

The diagrammatic notation of the tensor network also allows us to visualize and quickly estimate the computational complexity of a tensor network algorithm/contraction

rather easily. For instance, the top figure of Fig 1.6 (a) represents a matrix-vector contraction, and assuming each index (i.e., leg) of the matrix and vector is of dimension d , this contraction will be of order $\mathcal{O}(d^3)$. The general rule for estimating the computational complexity of a tensor contraction therefore involves multiplying the dimension of each leg of the 2 tensors involved in the contraction, taking care not to repeat the shared index (or indices) twice. In other words, the tensor network notation simplifies the estimation of complexity of tensor contractions into a simple leg counting exercise.

One basic ingredient on how tensor network manipulation can allow for great computational simplification involves the singular value decomposition (SVD) procedure. The SVD is the basic engine and backbone of data compression in approximating the exponentially large wavefunction into a wavefunction with polynomially large number of coefficients. This point will be illustrated using the Matrix Product State (MPS) in the next subsection. In addition, the SVD is also rapidly used when a unitary matrix is applied to an MPS to rapidly truncate the relevant dimensions of wavefunction. Again we will postpone the discussion of this to the subsection dealing with the Time-Evolving Block Decimation (TEBD) algorithm.

We will briefly discuss the SVD here. The SVD guarantees for an arbitrary (rectangular) matrix M of dimensions $N_A \times N_B$ the existence of a decomposition

$$M = USV^\dagger, \quad (1.17)$$

where U is an $N_A \times N_A$ matrix ($U^\dagger U = I$) with orthonormal columns (left singular vectors), V^\dagger is an $N_B \times N_B$ matrix ($V^\dagger V = I$) with orthonormal rows (right singular vectors), and S is an $N_A \times N_B$ rectangular diagonal matrix with non-negative real numbers on the diagonal. The diagonals of S , which we denote as $\{\sigma_i\}_{i=1, \dots, \min(N_A, N_B)}$, is the singular values of M , while $\{u_i\}_{i=1, \dots, N_A}$ and $\{v_i\}_{i=1, \dots, N_B}$ form two sets of orthonormal bases.

It is customary to construct U and V^\dagger such that the singular values $\{\sigma_i\}$ are arranged from the highest value to the lowest value. In this way, we can write the SVD as

$$M = \sum_{i=1}^{\min(N_A, N_B)} \sigma_i u_i v_i^*. \quad (1.18)$$

Here we briefly remark that the SVD is not unique. In tensor network compression scheme, we compress information contained in a quantum state (wavefunction) (1) either by fixing a set maximum number of allowed singular values we keep (we will call this maximum the **bond dimension**), (2) or truncating a number of singular values (the number of singular values thrown away is flexible) as long as the sum of the squared singular values being thrown away, i.e., $\sum_{i=k}^{\min(N_A, N_B)} \sigma_i^2 \leq \delta$, is less than some threshold error rate δ .

1.5.2 Matrix Product States and Schmidt Decomposition

Having introduced the tensor network notation and a brief foray into the SVD, we are now ready to discuss the simplest tensor network representation of a quantum state wavefunction in one dimension: the Matrix Product States (MPS).

Consider a one dimensional lattice of L sites with d dimensional local state space $\{s_i\}$ on sites $i = 1, \dots, L$. The most generic form of the quantum state is of the form

$$|\psi\rangle = \sum_{s_1, \dots, s_L} c_{s_1, \dots, s_L} |s_1, \dots, s_L\rangle. \quad (1.19)$$

A notation that gives a more local notion of the state and helps to break down the wavefunction into parts effectively is the MPS. There are 3 different forms of the MPS: (1) The left-canonical MPS, (2) The right-canonical MPS, and (3) the mixed-canonical MPS. We will introduce each type of MPS below. We will restrict our discussion to open boundary condition in this subsection since the MPS we will consider in Chapter

3 will have open boundary condition.

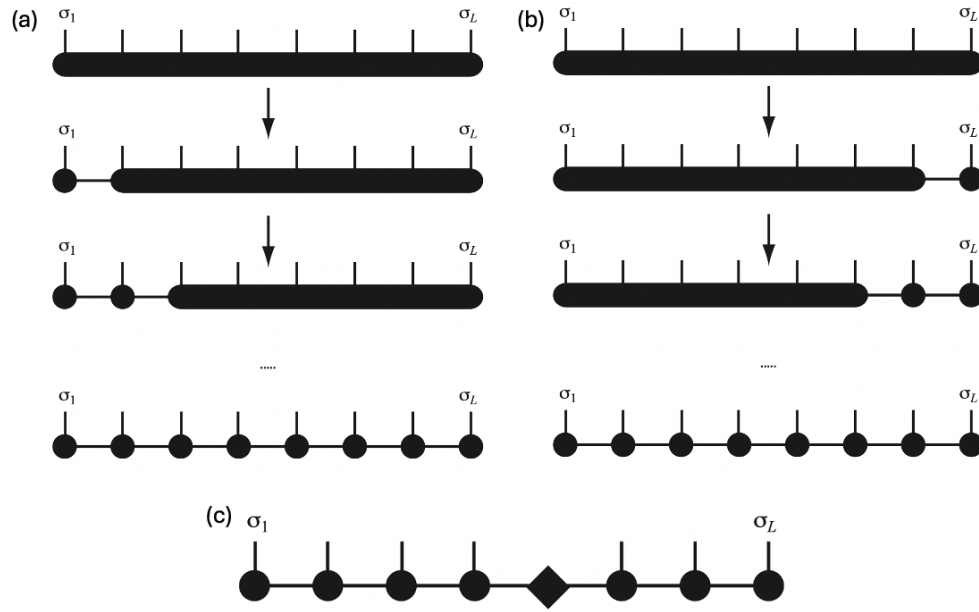


FIGURE 1.7: (a) An iterative procedure to cast a wavefunction into the left-canonical MPS, done by applying successive SVD on the wavefunction starting from left to right. (b) This represents the wavefunction being cast into the right-canonical MPS, by performing successive SVD from the right end instead. (c) This is the form of the mixed-canonical MPS, by applying successive SVD from both ends of the wavefunction. Figures are taken from [13].

(a) *Left-canonical MPS*. In the first step, we reshape a state vector with d^L components into a matrix of dimension $d \times d^{L-1}$, where the coefficients before and after the reshaping are related by

$$\Psi_{s_1, (s_2, \dots, s_L)} = c_{s_1, s_2, \dots, s_L}. \quad (1.20)$$

Performing an SVD on Ψ gives

$$c_{s_1, s_2, \dots, s_L} = \Psi_{s_1, (s_2, \dots, s_L)} = \sum_{a_1}^{r_1} U_{s_1, a_1} S_{a_1, a_1} (V^\dagger)_{a_1, (s_2, \dots, s_L)} \equiv \sum_{a_1}^{r_1} U_{s_1, a_1} c_{a_1, (s_2, \dots, s_L)}, \quad (1.21)$$

where in the last step we multiplied S and V^\dagger . The rank (hereby we shall call it the **bond dimension**) r_1 is taken to be $r_1 \leq d$, where equality holds when there is no truncation

after SVD. Reshaping $U_{s_1, a_1} = A_{a_1}^{s_1}$ and $c_{a_1, (s_2, \dots, s_L)}$ as $\Psi_{(a_1, s_2), (s_3, \dots, s_L)}$ of dimension $r_1 d \times d^{L-2}$, we have

$$c_{s_1, \dots, s_L} = \sum_{a_1}^{r_1} A_{a_1}^{s_1} \Psi_{(a_1, s_2), (s_3, \dots, s_L)}. \quad (1.22)$$

We subject the new Ψ matrix into another SVD and get (repeating the procedure above)

$$c_{s_1, \dots, s_L} = \sum_{a_1}^{r_1} \sum_{a_2}^{r_2} A_{a_1}^{s_1} A_{a_1, a_2}^{s_2} \Psi_{(a_2, s_3), (s_4, \dots, s_L)}, \quad (1.23)$$

and the new Ψ now has dimension $r_2 d \times d^{L-3}$, where $r_2 \leq r_1 d \leq d^2$. Upon further SVDs, we eventually get

$$c_{s_1, \dots, s_L} = \sum_{a_1, \dots, a_{L-1}} A_{a_1}^{s_1} A_{a_1, a_2}^{s_2} \dots A_{a_{L-2}, a_{L-1}}^{s_{L-1}} A_{a_{L-1}}^{s_L}, \quad (1.24)$$

or, more compactly,

$$c_{s_1, \dots, s_L} = A^{s_1} A^{s_2} \dots A^{s_{L-1}} A^{s_L}. \quad (1.25)$$

Thus, we have expressed a wavefunction into the *left-canonical MPS* form

$$|\psi\rangle = \sum_{s_1, \dots, s_L} A^{s_1} A^{s_2} \dots A^{s_{L-1}} A^{s_L} |s_1, \dots, s_L\rangle. \quad (1.26)$$

The procedure of repeated SVD is summarized graphically in Fig 1.7 (a). If no truncation ever occurs, the **bond dimension** $\{a_i\}$ each tensor A (not to be confused with physical local dimension $\{s_i\}$) has the maximum bound of $(1, d), (d, d^2), \dots, (d^{L/2-1}, d^{L/2}), (d^{L/2}, d^{L/2-1}), \dots, (d^2, d), (d, 1)$, going from the first to the last site. Of course, in tensor network algorithms and computation, we often set a maximum **bond dimension** so as to keep the dimension from growing exponentially. If we set a maximum bond dimension to be D , counting the number of parameters in an MPS will then give an estimate of order

$$LdD^2, \quad (1.27)$$

rather than d^L if there is no truncation of the singular values after SVD.

Another important remark is of interest here. It is so-called left-canonical because, at each step of the SVD, when we redefine U 's into A 's, we note that the set of A -matrices are *left-normalized*, i.e., from the property $U^\dagger U = I$ (left singular vectors in SVD), we have

$$\sum_{s_i} (A^{s_i})^\dagger A^{s_i} = I. \quad (1.28)$$

We will proceed next to the *right-canonical MPS*.

(b) *Right-canonical MPS*. We could equally start from the right end of a chain for the iterative SVD proceed to cast the quantum state into the right-canonical MPS. Doing this, we have

$$\begin{aligned} c_{s_1, \dots, s_L} &= \Psi_{(s_1, \dots, s_{L-1}), s_L} \\ &= \sum_{a_{L-1}} U_{(s_1, \dots, s_{L-1}), a_{L-1}} S_{a_{L-1}, a_{L-1}} (V)_{a_{L-1}, s_L}^\dagger \\ &= \sum_{a_{L-1}} \Psi_{(s_1, \dots, s_{L-2}), (s_{L-1}, a_{L-1})} B_{a_{L-1}}^{s_L} \\ &= \sum_{a_{L-2}, a_{L-1}} U_{(s_1, \dots, s_{L-2}), a_{L-2}} S_{a_{L-2}, a_{L-2}} (V)_{a_{L-2}, (s_{L-1}, a_{L-1})}^\dagger B_{a_{L-1}}^{s_L} \\ &= \sum_{a_{L-2}, a_{L-1}} \Psi_{(s_1, \dots, s_{L-3}), (s_{L-2}, a_{L-2})} B_{a_{L-2}, a_{L-1}}^{s_{L-1}} B_{a_{L-1}}^{s_L} = \dots \\ &= \sum_{a_1, a_{L-1}} B_{a_1}^{s_1} B_{a_1, a_2}^{s_2} \dots B_{a_{L-2}, a_{L-1}}^{s_{L-1}} B_{a_{L-1}}^{s_L}, \text{ and} \\ |\psi\rangle &= \sum_{s_1, \dots, s_L} B^{s_1} \dots B^{s_L} |s_1, \dots, s_L\rangle. \end{aligned} \quad (1.29)$$

Here, we deduce, from the property $V^\dagger V = I$, that the B -matrices are *right-normalized* (hence it is called the *right-canonical MPS*)

$$\sum_{s_i} B^{s_i} (B^{s_i})^\dagger = I. \quad (1.30)$$

The procedure of the iterative SVD from the right is illustrated in Fig 1.7(b).

(c) *Mixed-canonical MPS*. We can also start from both ends and perform the SVD down to the site l , ending up with a mixed-canonical MPS illustrated in Fig 1.7(c).

We perform SVD from the left up to the site l , ending up with

$$c_{s_1, \dots, s_L} = \sum_{a_l} (A^{s_1} \dots A^{s_l})_{a_l} S_{a_l, a_l} (V)_{a_l, (s_{l+1}, \dots, s_L)}^\dagger. \quad (1.31)$$

Reshaping V^\dagger and performing successive SVD from the right, we obtain

$$(V)_{a_l, (s_{l+1}, \dots, s_L)}^\dagger = \sum_{a_{l+1}, \dots, a_{L-1}} B_{a_l, a_{l+1}}^{s_{l+1}} \dots B_{a_{L-1}}^{s_L}. \quad (1.32)$$

All A-matrices are *left-normalized* while all B-matrices are *right-normalized*. We hence end up with a decomposition

$$c_{s_1, \dots, s_L} = A^{s_1} \dots A^{s_l} S B^{s_{l+1}} \dots B^{s_L}, \quad (1.33)$$

with singular values on the bond $(l, l + 1)$ as illustrated in Fig 1.7 (c).

The mixed-canonical MPS also gives us the *Schmidt decomposition* of an MPS into parts A and B automatically. Introducing the (normalized) vectors

$$|a_l\rangle_A = \sum_{s_1, \dots, s_l} (A^{s_1} \dots A^{s_l})_{1, a_l} |s_1, \dots, s_l\rangle, \quad (1.34)$$

$$|a_l\rangle_B = \sum_{s_{l+1}, \dots, s_L} (B^{s_{l+1}} \dots B^{s_L})_{a_l, 1} |s_{l+1}, \dots, s_L\rangle, \quad (1.35)$$

then we see the Schmidt decomposition of an MPS more explicitly (write $s_a = S_{a,a}$)

$$|\psi\rangle = \sum_{a_l} s_{a_l} |a_l\rangle_A |a_l\rangle_B. \quad (1.36)$$

The states on A and B are orthonormal respectively. Thus, the mixed-canonical MPS (with *gauge center* at site l) gives us Schmidt decomposition by construction.

One particular advantage of the bipartition structure of the Schmidt decomposition by the mixed-canonical MPS is that we can calculate n -th order Renyi entropy rather easily in this form of MPS. In fact, the sum of individual singular values s_a raised to the $2n$ -th gives us the n -th order Renyi entropy easily. To see this, we note that, first of all, the reduced density matrix of a mixed-canonical MPS for left part A of the system is

$$\begin{aligned}\rho_A &= \text{Tr}_B(\rho) = \sum_{a_l} \sum_{a_{l'}} \text{Tr}_B(s_{a_l} s_{a_{l'}} |a_l\rangle_A |a_l\rangle_B {}_A\langle a_{l'}| {}_B\langle a_{l'}|) \\ &= \sum_{a_l} \sum_{a_{l'}} s_{a_l} s_{a_{l'}} |a_l\rangle_A {}_A\langle a_{l'}| \delta_{a_l, a_{l'}} = \sum_{a_l} s_{a_l}^2 |a_l\rangle_A {}_A\langle a_l|,\end{aligned}\quad (1.37)$$

where we trace out the right partition B via $\text{Tr}_B(|a_l\rangle_B {}_B\langle a_{l'}|) = \delta_{a_l, a_{l'}}$ via the orthonormality of the set of basis $|a_l\rangle_B$. For n -th order Renyi entropy, we can then make use of the orthonormal property of $|a_l\rangle_A$ to compute ρ_A^n easily and this will give us

$$\begin{aligned}S_A^{(n)}(\rho_A) &= \frac{1}{1-n} \log(\text{Tr}_A(\rho_A^n)) \\ &= \frac{1}{1-n} \log\left(\sum_{a_{l_1}, \dots, a_{l_n}} \text{Tr}_A(s_{a_{l_1}} \dots s_{a_{l_n}} |a_{l_1}\rangle_A {}_A\langle a_{l_1}| \dots |a_{l_n}\rangle_A {}_A\langle a_{l_n}|)\right).\end{aligned}$$

The trace will give us many Kronecker delta's owing to orthonormality of the basis $\{|a_l\rangle_A\}$, enforcing $a_{l_1} = \dots = a_{l_n}$, and will then give us this nice final expression

$$S_A^{(n)}(\rho_A) = \frac{1}{1-n} \log\left(\sum_{a_l} s_{a_l}^{2n}\right).\quad (1.38)$$

Thus, once we cast the MPS into a mixed-canonical form, we can obtain the n -th order bipartite Renyi entropy easily via Eqn 1.38 above.

We note that while Eqn 1.38 is useful to obtain the regular Renyi entropy from ρ_A without computing the reduced density matrix ρ_A explicitly, computing the symmetry-resolved Renyi entropy in Sec 1.4 from $\rho_{A,Q}$ is not that straightforward. To date, the

author is only aware of the method to compute entropy from $\rho_{A,Q}$ via ‘brute-force’ approach of obtaining $\rho_{A,Q}$ directly rather than extracting the singular values of the mixed-canonical MPS. In Chapter 3, the normal entropy from ρ_A is calculated via the simple SVD approach above after casting MPS into the mixed-canonical form, while the symmetry-resolved version is computationally more expensive and requires one to obtain ρ_A explicitly and perform the projection numerically before extracting the symmetry-resolved Renyi entropy.

1.5.3 Time-Evolving Block Decimation

We end our discussion on the tensor network algorithm with a discussion on the numerical method used to perform real time evolution of the Hamiltonian. For illustrative purposes, let us consider the one-dimensional spin- $\frac{1}{2}$ Heisenberg Hamiltonian¹

$$H = \sum_{j=1}^{L-1} h_{j,j+1} = \sum_{j=1}^{L-1} S_j^x S_{j+1}^x + S_j^y S_{j+1}^y + S_j^z S_{j+1}^z. \quad (1.39)$$

The exact real-time unitary evolution is given by

$$U^{exact}(\delta) = e^{-i\delta H}. \quad (1.40)$$

If we represent this as a tensor without breaking this down into smaller tensor blocks, we will end up with a tensor with L incoming legs and L outgoing legs, and the unitary matrix itself will scale exponentially as $d^L \times d^L$. We clearly need to break this down for large system size L beyond the reach of the exact diagonalization method (capable for size up to $L \sim 16$) and perform **trotterized time evolution** to avoid prohibitive exponential scaling.

¹Other Hamiltonians involving summation of both one- and three-body terms Hamiltonian can be adapted accordingly.

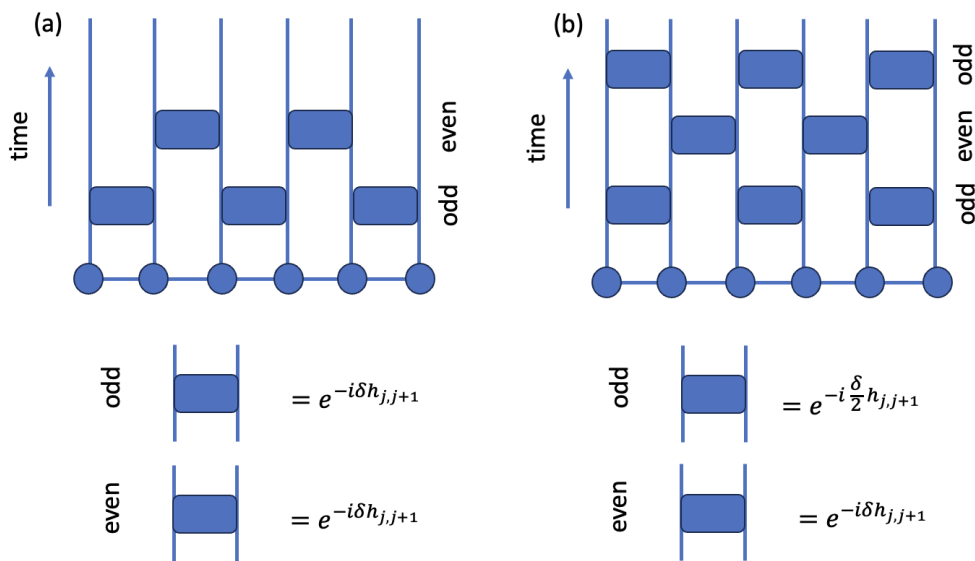


FIGURE 1.8: (a) First order TEBD, and (b) Second order TEBD, for Hamiltonians with 2 qubits gates. 3 qubits gates can be generalized accordingly by having 3 sets of gates instead, labelling set 1 $\{3j - 2, 3j - 1, 3j\}$, set 2 $\{3j - 1, 3j, 3j + 1\}$, and set 3 $\{3j, 3j + 1, 3j + 2\}$, instead of odd $\{2j - 1, 2j\}$ and even $\{2j, 2j + 1\}$ sets for 2 qubits gates.

Instead, we will introduce the Time-Evolving Block Decimation (TEBD) method. Roughly speaking, we will break down the exact unitary real-time evolution operator U^{exact} into smaller, trotterized blocks of unitary real-time evolution operators consisting of individual $h_{j,j+1}$ terms in the Hamiltonian H .

For Hamiltonian with 2-qubits gates, we break down the Hamiltonian sum into its odd and even parts

$$H_{\text{even}} = \sum_{j \text{ even}} h_{j,j+1}, \quad (1.41)$$

$$H_{\text{odd}} = \sum_{j \text{ odd}} h_{j,j+1}, \quad (1.42)$$

$$H = H_{\text{odd}} + H_{\text{even}}. \quad (1.43)$$

From the Baker–Campbell–Hausdorff (BCH) formula

$$\begin{aligned} e^Z &= e^X e^Y, \\ Z &= X + Y + \frac{1}{2}[X, Y] + \frac{1}{12}[X, [X, Y]] - \frac{1}{12}[Y, [X, Y]] + \dots, \end{aligned}$$

we can approximate the exact unitary as

$$\begin{aligned} U^{exact}(\delta) &= e^{-i\delta H} \\ &\approx e^{-i\delta H_{\text{even}}} e^{-i\delta H_{\text{odd}}} e^{-i\delta^2 [H_{\text{even}}, H_{\text{odd}}]} \\ &\approx e^{-i\delta H_{\text{even}}} e^{-i\delta H_{\text{odd}}} \equiv U^{\text{TEBD1}}(\delta). \end{aligned} \tag{1.44}$$

Both $e^{-i\delta H_{\text{even}}}$ and $e^{-i\delta H_{\text{odd}}}$ are easy to evaluate, since all terms within each summation now commute with each other. We note that, for instance,

$$e^{-i\delta H_{\text{odd}}} = e^{-i\delta \sum_{j \text{ odd}} h_{j,j+1}} = \prod_{j \text{ odd}} e^{-i\delta h_{j,j+1}}.$$

Therefore, the **first order TEBD** is given by the form below and is represented diagrammatically in Fig 1.8 (a),

$$U^{\text{TEBD1}}(\delta) = \prod_{j \text{ even}} e^{-i\delta h_{j,j+1}} \prod_{j \text{ odd}} e^{-i\delta h_{j,j+1}}. \tag{1.45}$$

The order of error, for small δ , is $U^{exact}(\delta) = U^{\text{TEBD1}}(\delta) + \mathcal{O}(\delta^2)$ (due to the approximation $e^{-i\delta^2 [H_{\text{even}}, H_{\text{odd}}]} \approx I - i\delta^2 [H_{\text{even}}, H_{\text{odd}}]$). Consider a long time interval T , which we divide into $\frac{T}{\delta}$ smaller intervals. In this case, the error accumulates to $\frac{T}{\delta} \mathcal{O}(\delta^2) = \mathcal{O}(\delta)$. The error for long time interval T using the TEBD scheme in Fig 1.8 is thus of first order (and hence its name).

A better way to perform the trotterization is to decompose the trotterization symmetrically as illustrated in Fig 1.8 (b). In that case, we introduce the **second order TEBD**

of the form

$$U^{\text{TEBD2}}(\delta) = \prod_{j \text{ odd}} e^{-i\frac{\delta}{2}h_{j,j+1}} \prod_{j \text{ even}} e^{-i\delta h_{j,j+1}} \prod_{j \text{ odd}} e^{-i\frac{\delta}{2}h_{j,j+1}}, \quad (1.46)$$

which has the third-order error per step

$$U^{\text{exact}}(\delta) = U^{\text{TEBD2}}(\delta) + \mathcal{O}(\delta^3), \quad (1.47)$$

and hence error rate of second order in longer time intervals (hence its name). This is the trotterization scheme we will use in Chapter 3, suitably readapted to include trotterization with one- and three-qubits gates.

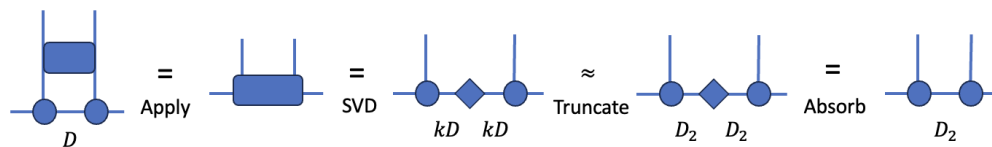


FIGURE 1.9: The process of applying a trotterized 2 qubits unitary gate as tensor onto the 2 qubits sites of an MPS. The 2 qubits gate in general multiply a particular bond by its rank k (for 2 qubits gate, the maximum rank k is 4) when applied exactly without any truncation. We then perform SVD and truncate the extra singular values so that the bond dimension of the particular MPS bond grows to D_2 instead, and finally absorbs the diagonal S tensor into the 2 tensor sites of the MPS via multiplication and redefinition.

One final remark is in order to explain how each small TEBD block works in the tensor network algorithm. The inner working of each small TEBD block on the qubits/sites acted upon is summarized pictorially in Fig 1.9. In this case, any 2-qubits gate comes with it the rank k of the gate, where k can range from 2 to 4 at most in the case of 2-qubits gates. The famous example of the unitary 2-qubits gate from the kicked Ising model is of rank 2, since $e^{-i\delta Z_i Z_{i+1}}$ can be expanded to only include identity I and $Z_i Z_{i+1}$. The spin- $\frac{1}{2}$ Heisenberg model example we have in Eqn 1.5.3, however, saturates the maximum rank k that a 2-qubits gates can multiply onto the bond dimension linking the 2-qubits of interest. In each small TEBD sub-step, we will trotterize the bond

dimension after SVD as illustrated in Fig 1.9 above. This will be used extensively to perform time evolution for the quench problem in Chapter 3.

Chapter 2

Measurement Induced Chirality: Diffusion and Disorder

2.1 Introduction

The development of engineering novel quantum systems by applying periodic (Floquet) driving has produced quantum phases without a static analog [29–37]. A prominent example is the anomalous Floquet topological insulator [33–36], where a chiral edge state emerges alongside completely trivial bulk bands, in stark contrast to standard topological insulators. The idea behind this phase is to break time reversal symmetry by sequentially modulating particle hopping on a lattice; this stirs the particles in such a way that their trajectories in the bulk trace out closed loops, whilst on the edge chiral states emerge [29]. Such dynamics has been realized experimentally in, for example, cold atom systems [38, 39], while theoretically these ideas have recently been extended to interacting systems where an even more diverse class of topological phases emerges [35, 40–42].

On the other hand, the interplay between measurements and unitary time evolution in quantum many-body systems has received renewed interest in recent years [1, 43–71]. This is, in part, due to developments on phase transitions in the entanglement

entropy of random unitary circuits with measurements (see [62] and references therein) as well as on the utility of measurements to induce non-trivial dynamics and to prepare quantum states [1, 72–76].

In [1], it was shown that periodic sequences of measurements may be used to induce chiral edge charge transport alongside trivial bulk dynamics in a way much analogous to anomalous Floquet insulators. The general intuition behind this procedure is to use measurements to control the effective particle hopping on a lattice. This may be seen most clearly in the limit of rapid measurements, the quantum Zeno limit, where dynamics is frozen within monitored sections of the lattice and hopping is eliminated between monitored and un-monitored sections of the lattice. This measurement-based control of the particle hopping may then be leveraged to recreate the periodic modulation of hopping amplitudes used to induce anomalous Floquet insulators. However, the measurement-based scheme also exhibits distinct features due to the non-unitary nature of the evolution.

In this work, we continue an investigation of the measurement-induced chirality protocol [1] by looking at the following aspects. (1) The diffusive dynamics of the measurement-induced chiral systems when the system is tuned away from the ‘perfect swapping’ limit and away from the Zeno measurement limit, and (2) the effects of various kinds of disorder on the measurement-induced chiral flow rate in our free fermion systems hopping on a Lieb lattice. In particular, we consider chiral flow in the case of site vacancy disorder, random hopping strength, and random onsite potential, both in and out of the Zeno measurement limit, and diffusive dynamics for the case of random onsite potential. Indeed, an important characterization of systems exhibiting chiral physics is their response to disorder, as have been long studied in, e.g. the context of the quantum Hall effect [77, 78], where relations to percolation physics have been explored. Disorder also plays a crucial role in the anomalous Floquet insulators mentioned above.

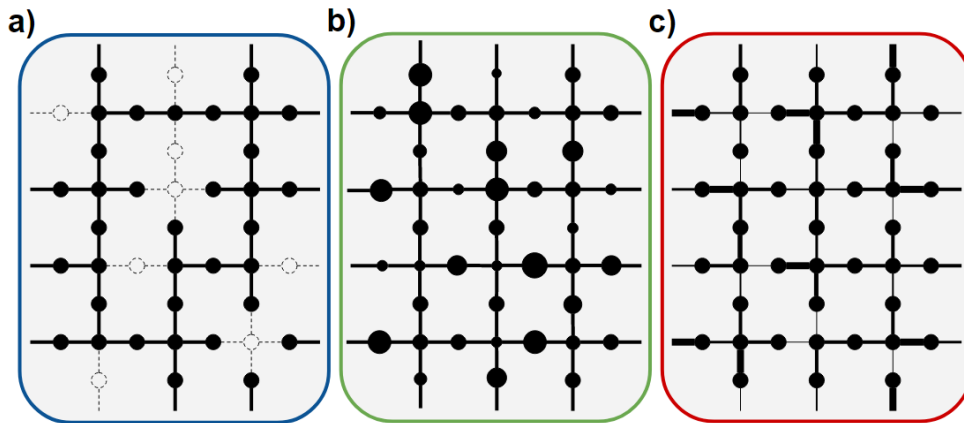


FIGURE 2.1: The three varieties of disorder considered in this work: a) Sites are randomly removed from the lattice with probability p . b) Random on-site potentials are applied to the lattice (the strength of the potential at each site is represented by the size of the vertex) c) The hopping strength between adjacent sites is given by a uniform, random distribution (represented by the size of the edge).

The approach we take in this paper will import techniques developed in [11], in similar spirit taken in our earlier work [1]. In [11], the competing effects of unitary evolution and measurements were studied using a closed hierarchy approach. This technique has also been used, for example, to describe non-equilibrium steady states of current [11] and density fluctuations (quantum wakes) following a moving particle detector and other disturbances [79].

The structure of our work is as follows. In section II, we briefly review the measurement protocols and the basic physics behind our earlier work on measurement-induced chirality [1]. This is followed by studying the diffusive dynamics of the measurement-induced chirality out of the ‘perfect swapping’ parameter and out of Zeno limit in section III. After dealing with clean systems, we proceed to study 2 varieties of disorders in subsequent sections as illustrated in Fig 2.1. In section IV, we deal with site vacancy disorder for our system in the Zeno limit, as motivated by our system. In particular, there is a percolation threshold when measurement period is tuned to ‘perfect swapping’ case with deterministic walk [80]. In section V, we numerically simulate the effect

of random hopping strength and random onsite potential on the chiral flow rate induced by measurement, still operating in the Zeno limit, and provided an analytical mean field treatment to describe the weak disorder limit. In section VI, we investigate numerically the diffusive dynamics and the chiral flow rate for our measurement-induced chiral system under all three types of disorder (vacancy, random hopping and random potential) away from the Zeno limit. We present discussions and possible outlook in section VII.

2.2 Measurement Induced Chirality Protocol

In this section, we briefly review the protocol realizing the measurement induced chirality in [1]. We consider fermions freely hopping on a Lieb lattice, subject to a cycle of local density measurements as follows.

The measurement cycle in Fig 2.2 consists of 8 steps taking an overall measurement period T . At each step, we take repeated measurements to detect particles throughout a subset of the lattice, while the system is allowed to evolve freely in between measurements with the nearest neighbour hopping Hamiltonian $\mathcal{H} = -t_{hop} \sum_{\langle i,j \rangle} c_i^\dagger c_j + \text{h.c.}$. We denote the set of sites *not* being measured at step i by A_i as marked in Fig (2.2) and enforce periodicity by setting $A_{i+8} = A_i$. Within step i , we carry out the following steps:

1. Particle densities at all sites in $(A_i \cap A_{i-1})^c$ are measured, i.e., we measure all other sites in the lattice *except* the sites circled in each step in Fig 2.2
2. Free evolution under a free hopping Hamiltonian $\mathcal{H} = -t_{hop} \sum_{\langle \mathbf{r}, \mathbf{r}' \rangle} c_{\mathbf{r}}^\dagger c_{\mathbf{r}'} + \text{h.c.}$ for a time $\tau = \frac{T}{8n}$. Here n is an integer describing the measurement frequency.
3. Particle densities at all sites in A_i^c are measured.

4. Steps 2 and 3 are repeated n times.

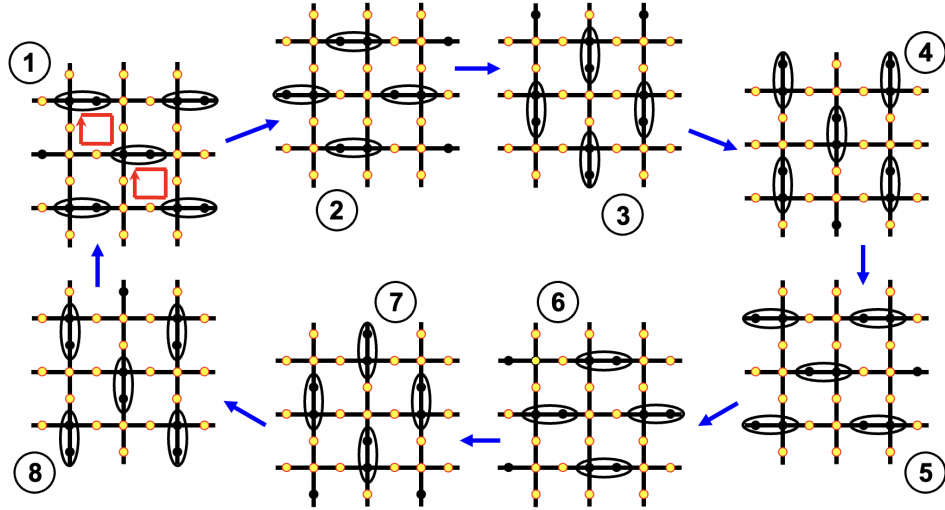


FIGURE 2.2: Measurement protocol. Yellow vertices indicate the set of repeatedly measured sites, while black sites are the unmeasured, free evolving set, A_i . The adjacent black vertices trace out a chiral path around a plaquette in the Lieb lattice. In the Zeno limit with perfect swapping parameters, particles will trace out the path as shown by the red loops in first figure.

The overall effect of the measurement protocol has been shown in [1] to exhibit protected chiral charge flow of the particles, as shown by the red loops in Fig 2.2. The physical intuition of measuring everywhere in the lattice other than the circled sites is to restrict (and in the case of rapid Zeno monitoring, freeze entirely) particle motion elsewhere other than between the circled pairs of sites. This dynamics is reminiscent of the Anomalous Floquet Topological Insulator [29] in that we selectively switch on certain links on the lattice where free evolution are allowed to take place, but also presents differences due to the non-unitary nature of the measurements.

We emphasize that the Lieb lattice was chosen for ease of comparison with the Floquet insulator dynamics of [29], however the particularities of the band structure associated with the Lieb lattice (a flat band) are not important since any coherent dynamics is quickly disrupted by measurement as we will see in detail. It is only for

reduced measurement rates that effects from the band structure may begin to emerge. We also remark that the measurement protocol is not restricted to the Lieb lattice alone. For a more thorough discussion on the geometric conditions a lattice needs to satisfy in order to carry out a measurement protocol as above, we refer interested readers to Appendix C in [1].

In order to study the charge flow, we focus on the dynamics of the two point correlation function $G(t)_{\mathbf{r}\mathbf{r}'} = \text{Tr}(\rho(t)c_{\mathbf{r}}^{\dagger}c_{\mathbf{r}'})$ under measurement and unitary time evolution. The correlation G transforms in a simple way under particle detection measurements and under non-interacting evolution, respectively (see e.g. [1, 11]):

$$G \rightarrow (1 - P_{\mathbf{r}})G(1 - P_{\mathbf{r}}) + P_{\mathbf{r}}GP_{\mathbf{r}}, \quad (2.1)$$

$$G \rightarrow UGU^{\dagger}, \quad (2.2)$$

where $P_{\mathbf{r}} = |\mathbf{r}\rangle\langle\mathbf{r}|$ is the projector onto site \mathbf{r} where a particle detection measurement is has been performed, and $U = \exp(-iHt)$ is the (single particle) unitary time evolution between consecutive measurements under the free Hamiltonian H for time t . We stress that the map (2.1) is the result of averaging over measurement outcomes.

It is informative to consider the limit of many measurements per step ($n \rightarrow \infty$), i.e. the quantum Zeno limit. The signature characteristic of this regime is the freezing of evolution in the subspace of measured sites while free evolution continues to occur between unmeasured sites. In other words, the time evolution during the i -th step of the 8 step measurement cycle may be replaced by evolution under the Hamiltonian

$$\mathcal{H}_{A_i} = -t_{hop} \sum_{\langle\mathbf{r}\mathbf{r}'\rangle \in A_i} c_{\mathbf{r}}^{\dagger}c_{\mathbf{r}'} + \text{h.c.}, \quad (2.3)$$

where now the evolution is confined to between unmeasured sites within each set A_i .

Another important aspect of the dynamics in the Zeno limit is that in this limit,

repeated application of Eq. (2.1) under our protocol, kills off-diagonal elements of G between sites in the set A_i^c , and the switch between measurement of A_i^c to the next step A_{i+1}^c eliminates any lingering off-diagonal correlations that have developed inside the set A_i during the evolution [1]. Therefore, at the beginning/end of steps we only need to keep track of the diagonal components $G_{\mathbf{r}\mathbf{r}}$. Let us combine these in a vector, $|g(t)\rangle$, where $\langle \mathbf{r} | g(t) \rangle \equiv G_{\mathbf{r}\mathbf{r}}$. Then the effective action of step i in the protocol, including the unitary evolution and measurements in the Zeno limit, is described by

$$|g(t)\rangle \rightarrow R |g(t)\rangle \quad (2.4)$$

$$R_i = \oplus_{\langle \mathbf{r}, \mathbf{r}' \rangle \in A_i} \begin{pmatrix} 1 - p_{hop} & p_{hop} \\ p_{hop} & 1 - p_{hop} \end{pmatrix} \oplus_{\text{other sites } I} I, \quad (2.5)$$

i.e. the evolution of the local particle density $|g_i(t)\rangle$ in the Zeno case is given by a periodically driven random walk. The probability for hopping between sites is related to the period of each measurement step $T/8$ by the following equation [1]

$$p_{hop} = \sin^2\left(\frac{T}{8}\right). \quad (2.6)$$

Note that when the full measurement period $T = 4\pi(2n + 1)$, $n \in \mathbb{Z}$, we have $p_{hop} = 1$ and the evolution becomes deterministic hopping/walk, a situation we call "perfect swapping". Similarly, when $T = 8\pi n$ the evolution is frozen, with $p_{hop} = 0$. We now summarize the two methods used in [1] to measure the chiral charge transport induced by the measurement protocol in the system.

In the first method, the charge flow is found numerically by making a cut through the lattice and measuring the charge flow across it, Fig. 2.3. Namely, the number of particles flowing across the slice is found by measuring the change in total particle

number below the cut, i.e. given by

$$F_{sim}(t) \equiv \sum_{\mathbf{r} \text{ below slice}} (G(t)_{\mathbf{r}\mathbf{r}} - G(t=0)_{\mathbf{r}\mathbf{r}}). \quad (2.7)$$

In order to measure the charge flow along a given edge in the system, we fill up all the sites near that edge with particles and then measure (2.7) while applying the measurement protocol. The filling of half the system with particles must be done since, if the whole system was filled, opposite edges in the system would exhibit charge transport with equal magnitude but opposite direction, thereby leading to a no net flow of particles across the cut. The details of how particles are inserted into the bulk of the system and the specific path of the cut through the lattice do not affect the charge flow per measurement cycle (beyond transient effects) [1].

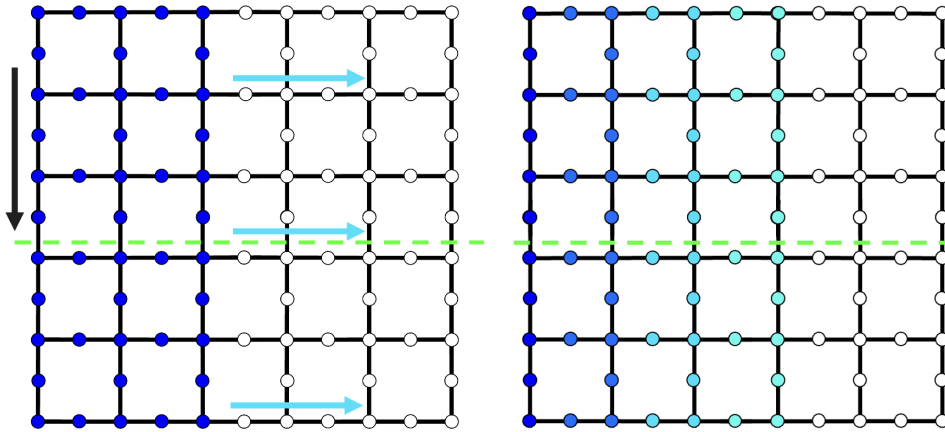


FIGURE 2.3: Left: The initial configuration and setup for studying chiral particle flow for all disorder cases considered (with left half plane filled with particles in blue). The particle exhibits both downward chiral motion (black arrow) and diffusive motion which moves the front to the right (blue arrows). Right: After running the protocol in the half-filled lattice setting, particles density increases beyond the initial configuration, where lighter blue indicates lower particle density.

The second method used to measure the chiral particle flow assume rapid measurements and relies on the counting statistics of the transport up or down in the system. We introduce a counting field $e^{i\theta}$ to each vertical link by modifying the transition

matrices R_3, R_4, R_7, R_8 to

$$R_i = \bigoplus_{\langle \mathbf{r}, \mathbf{r}' \rangle \in A_i} \begin{pmatrix} 1 - p_{hop} & e^{i\theta} p_{hop} \\ e^{-i\theta} p_{hop} & 1 - p_{hop} \end{pmatrix} \bigoplus_{\text{other sites}} I \quad (2.8)$$

whenever \mathbf{r}, \mathbf{r}' are nearest neighbours on a vertical line such that site \mathbf{r} is located above \mathbf{r}' . We will denote the transition matrix (with counting fields) of the full measurement cycle by

$$R_{cyc}(\theta) = R_8 R_7 R_6 R_5 R_4 R_3 R_2 R_1 \quad (2.9)$$

With the counting field present, we can introduce the moment generating function after N measurement cycles

$$\chi_N(\theta) = \sum_{\mathbf{r}\mathbf{r}'} [R_{cyc}(\theta)^N]_{\mathbf{r}\mathbf{r}'} G_{\mathbf{r}\mathbf{r}}(t=0) \quad (2.10)$$

which may be used to calculate the charge transport in the y direction. Namely, the flow per unit length per measurement cycle (in the long time, $N \rightarrow \infty$, limit) is given by

$$F = \lim_{N \rightarrow \infty} \frac{1}{L_y} \frac{1}{N} i\partial_\theta \chi_N(\theta)|_{\theta=0} \quad (2.11)$$

with L_y the length of the system in the y direction.

In [1], it was shown that the analytical form of the flow in the Zeno limit exhibits bulk-edge decomposition in the sense that F can be decomposed into a term that is calculated entirely with bulk operators only and another term that is computed from

the edge operators alone

$$F = F_{bulk} + F_{edge}. \quad (2.12)$$

A computation performed in [1] shows the flow F_{edge} depends on p_{hop} via

$$F_{edge} = p_{hop}^2 + p_{hop}^3 + p_{hop}^4. \quad (2.13)$$

The other flow term F_{bulk} , on the other hand, depends on p_{hop} in a more nontrivial way, and it is best instead to express F_{bulk} in the following form in terms of the bulk operators

$$F_{bulk} = i \sum_{\alpha\beta} \left[J_B(\mathbf{k}) \frac{1}{I - R_B(\mathbf{k})} \partial_{k_y} R_B(\mathbf{k}) \right]_{\alpha\beta} \Big|_{\mathbf{k}=0}. \quad (2.14)$$

Here, $R_B(\mathbf{k}) = R_B(\mathbf{k}, \theta = 0)$ is a bulk transition operator, equivalent to $R_{cyc}(\theta)$ in Eqn (2.9) except that it comes with periodic boundary conditions instead of open boundary conditions. In equation (2.14) R_B is expressed in \mathbf{k} -space. The explicit construction of $R_B(\mathbf{k}, \theta)$ is delineated in Appendix 2.A as a 6×6 matrix in terms of p_{hop} , \mathbf{k} and the counting field θ . Here, $J_B(\mathbf{k}) = -i\partial_\theta R_B(\mathbf{k}, \theta)|_{\theta=0}$. From the expressions of $J_B(\mathbf{k})$ and $R_B(\mathbf{k})$ (as a nontrivial matrix of p_{hop}) one can then compute F_{bulk} from a given p_{hop} as a sum of the resulting matrix elements. This formalism is summarized rather briefly here and we refer readers to [1] for a more extensive discussion and proof.

2.3 Measurement induced diffusion

In [1] (as reviewed in Sec. 2.2), the focus was on the emergence of the protected, chiral transport near the edge of the system. However, it is worth analyzing further the dynamics in the bulk.

One reason is that the bulk dynamics sets the time scale over which the chiral edge transport is sustained. To see this, take for example the initial particle configuration

described in Fig. 2.3. Note that if any of the holes initially located in the right half plane of the lattice reach the left boundary of the system at some time during the evolution, then the hole may be transported along the edge in place of a particle. This would then alter (namely, reduce) the edge flow. Hence, the time scale over which the flow F is robust is set by the length of time it takes for holes initially in the bulk to reach the boundary. In this section, we study the diffusive behavior of bulk particles (and holes). We calculate the diffusion coefficient analytically in the Zeno limit of our measurement protocol and find it numerically for finite measurement frequencies.

Another reason to take a closer look at the dynamics in the bulk, is that it acts as a further probe of the interplay between the chirality of the measurement scheme and the stochastic behavior induced from the random measurement outcomes. The juxtaposition of these two effects was particularly clear when analyzing the edge dynamics. For example, working in the Zeno limit, consider replacing the chiral stochastic evolution R_{cyc} (2.9), by evolving with a randomized protocol, where in each step of the 8-steps protocol we randomly pick R_i and average over all possible outcomes. This situation is described by the averaged cycle $\overline{R_{cyc}} = \frac{R_1+R_2+R_3+R_4+R_5+R_6+R_7+R_8}{8}$. In this case, the random walk exhibits diffusive dynamics even in the perfect swapping case, in sharp contrast with the chiral protocol Fig 2.6. It is truly the chiral nature of the drive that then is responsible for the ballistic transport along the edge. In the bulk of the system, transport is diffusive as it would be without the introduction of chirality into the drive, but nonetheless the chirality does still play a role leading to different diffusion constants.

A clarifying comment is in order about different origins of the diffusive dynamics in the system. Namely, there are two distinct ways to induce diffusion discussed in this paper: through the measurements (via the tuning of the length of each measurement step away from perfect swapping or by reducing measurement frequency) which occurs already in the clean system, and through the addition of disorder (e.g. on-site

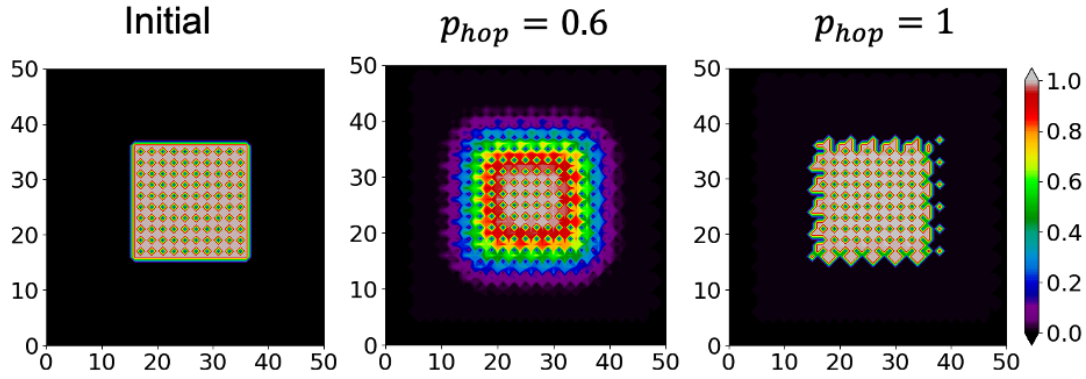


FIGURE 2.4: A finite droplet on 51×51 Lieb lattice is allowed to evolve under quantum Zeno measurement and unitary evolution. The droplet configuration for $p_{hop} = 0.6$ exhibits both outward diffusion and clockwise chiral edge transport while the droplet for $p_{hop} = 1$ exhibits clockwise chiral edge motion only. The droplet setup is employed for all calculations and simulations on the diffusion constant.

potential or hopping strength disorder). In this Section, we focus on the former, leaving a discussion of disorder-induced diffusion to Sections 2.5 and 2.6.

Transport in a system is defined as diffusive when the average squared displacement from the center of mass is linear in time, i.e.

$$\langle \Delta r^2(t) \rangle = Dt, \quad (2.15)$$

where D is the diffusion constant. In our case, starting with $G_{\mathbf{r}\mathbf{r}}(t=0) = \delta_{\mathbf{r}\mathbf{r}'}\delta_{\mathbf{r},0}$, we have

$$\begin{aligned} \langle \Delta r^2(t=NT) \rangle &\equiv \frac{\sum_{\mathbf{r}} (\mathbf{r} - \mathbf{r}_{mean}(t=NT))^2 G_{\mathbf{r}\mathbf{r}}(t=NT)}{\sum_{\mathbf{r}} G_{\mathbf{r}\mathbf{r}}(t=NT)}, \\ \mathbf{r}_{mean}(t=NT) &\equiv \frac{\sum_{\mathbf{r}} \mathbf{r} G_{\mathbf{r}\mathbf{r}}(t=NT)}{\sum_{\mathbf{r}} G_{\mathbf{r}\mathbf{r}}(t=NT)}, \\ D &= \lim_{N \rightarrow \infty} \frac{\langle \Delta r^2(t=NT) \rangle - \langle \Delta r^2(t=0) \rangle}{NT}. \end{aligned} \quad (2.16)$$

Numerical results for the diffusion constant are shown in Fig. 2.5, for both Zeno limit and finite measurement frequencies.

As one reduces the measurement frequency per measurement step away from the Zeno limit, the diffusion constant increases. The feature where diffusion transport is suppressed (or absent in the Zeno limit) at $T = 4\pi n, n \in \mathbf{Z}_+$ becomes less pronounced in low frequency limit, and eventually the diffusive transport will become ballistic without any measurement.

In the Zeno limit, the absence of diffusion at $T = 4\pi n, n \in \mathbf{Z}_+$ can be attributed either to the perfect swapping case where $n \in \text{odd}$, or the zero hopping case where $n \in \text{even}$ by inspecting Eqn 2.6, with $p_{hop} = \sin^2(\frac{T}{8})$ (setting $t_{hop} = 1$). We note that the Zeno limit diffusion constant curve exhibits 8π periodicity.

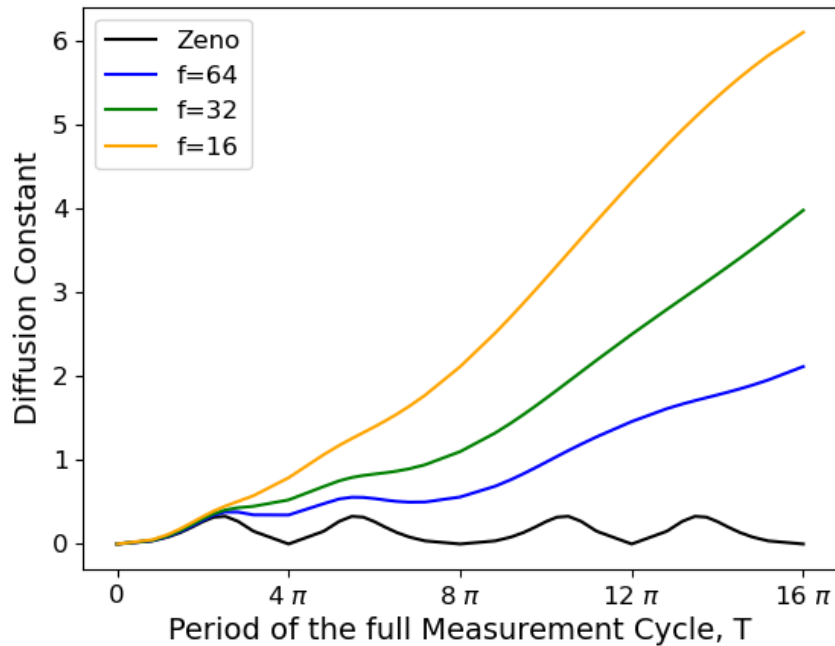


FIGURE 2.5: The diffusion constant in a measurement induced chiral Lieb lattice as a function of the period of measurement cycle T up until $T = 16\pi$, where in the Zeno limit the diffusion constant is periodic with 8π . Various measurement frequencies per measurement step, f , is shown.

We can extract the diffusion constant both analytically and numerically in the Zeno limit. Numerically, we calculate the diffusion constant on a finite lattice using Eqn 2.16 for intermediate time scale before the particle distribution hits the boundary

by having nonzero $G_{\mathbf{r}\mathbf{r}}(t) > 0$ for boundary sites \mathbf{r} . Analytically, we consider a translationally invariant system with setup considered in Appendix 2.A, placing a single particle at the position 1 of the unit cell at origin and performing the calculation in momentum space with the formula (see derivation in Appendix 2.A)

$$\begin{aligned}
D &= \lim_{N \rightarrow \infty} \frac{1}{8N} \left[\sum_{\mu=1}^6 [-\nabla_{\mathbf{k}}^2 R_B^N(\mathbf{k})|_{\mathbf{k}=0}]_{\mu,1} \right. \\
&\quad + \left. \left[\sum_{\mu=1}^6 [\partial_{k_x} R_B^N(\mathbf{k})|_{\mathbf{k}=0}]_{\mu,1} \right]^2 \right. \\
&\quad + \left. \left[\sum_{\mu=1}^6 [\partial_{k_y} R_B^N(\mathbf{k})|_{\mathbf{k}=0}]_{\mu,1} \right]^2 \right] \quad (2.17)
\end{aligned}$$

where $R_B = R_8 R_7 R_6 R_5 R_4 R_3 R_2 R_1$ is the 6×6 transition matrix in Eq 2.5 written in k -space (see Appendix 2.A for explicit form of $R_i(\mathbf{k})$) by making use of translational invariance. We see that the analytical and numerical result agree well as shown in Figure 2.6.

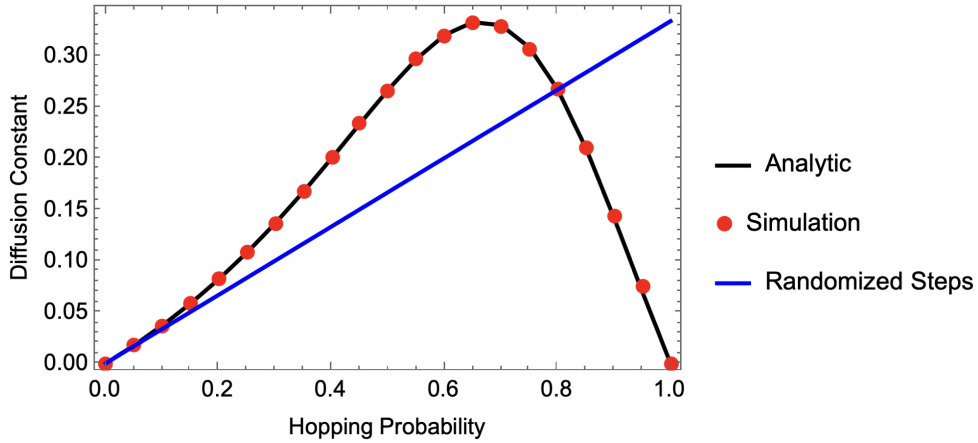


FIGURE 2.6: The diffusion constant as a function of hopping probability for measurement induced chirality in clean system, in the Zeno limit. The averaged randomized quantum Zeno measurement protocol is shown in the blue line.

Identifying the diffusion coefficient, is also helpful for the numerical calculation of the edge flow we discuss in the next section. Indeed, to correctly extract the late time

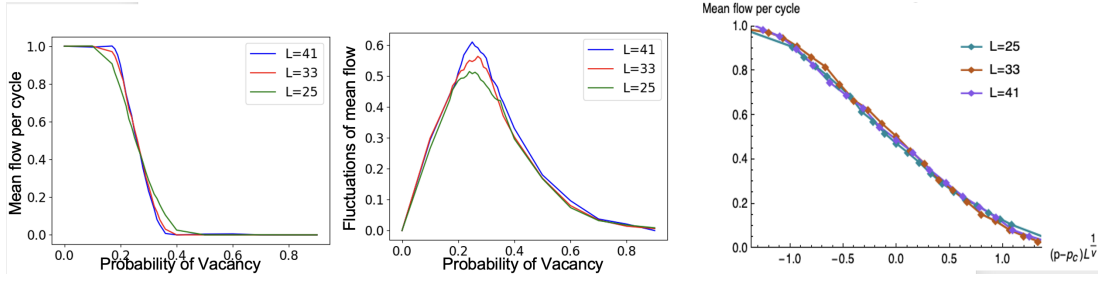


FIGURE 2.7: Left: Mean flow per cycle in the perfect swapping case $p_{hop} = 1$ plotted as a function of probability of site vacancy in the lattice p_α for various linear system sizes L_x (see Fig 2.3) over 1000 disorder realizations. Middle: The fluctuations of the mean flow per cycle across 1000 disorder realizations for various system sizes with peak around $p_c \approx 0.26$. Right: The scaling collapse with the functional form $\langle F \rangle = f((p_\alpha - p_c)L^{1/\nu})$, where $p_c \approx 0.26$ and $\nu \approx 1.35$.

dynamics of the measurement induced chiral flow, one wants to estimate the maximum time scale t_{max} for which the chiral flow counts mostly only the flow travelling to the lower half of the Lieb lattice setup in Figure 2.3 before the transverse spreading from diffusion hits the right boundary of the Lieb lattice in Figure 2.3. This is done to exclude finite size lattice boundary effects on the numerical counting of the chiral flow. By taking into account the transverse diffusive transport, we can extract the late time chiral transport for different system sizes while taking into account finite size effect systematically. We discuss how we extract the late time mean flow per cycle for the rest of the paper in appendix 2.B.

2.4 Site dilution and Percolation Threshold

In [1], the measurement induced chiral charge transport along the edge of the system was shown to be protected against edge perturbations in analogy with the protected edge flow induced in anomalous Floquet insulators. In order to investigate further the nature of the measurement-induced protection, we now turn to consider the effects of

several different varieties of disorder on the chiral flow. Furthermore, these considerations of disorder will also be useful for gaining insight into the effects of imperfections that may occur in real experimental implementations of the measurement protocol.

The first kind of disorder we consider is site vacancy disorder. Namely, as shown in Fig. 2.1a, we consider a situation where there is a probability p_α for each site on the Lieb lattice to be vacant, i.e. where particles are prohibited from hopping to or from the vacant sites. The locations of the vacant sites then stays constant throughout the measurement protocol.

In this section, we will only consider the quantum Zeno limit and postpone results away from the Zeno limit until section 2.6. In this case, there are 2 different scenarios: (1) the perfect swapping case ($p_{hop} = 1$) where we will see that the dynamics is entirely determined by geometric considerations with the flow set by the site percolation threshold p_c of the Lieb lattice, and (2) cases away from perfect swapping ($p_{hop} < 1$) where both the stochastic nature of the dynamics and site percolation effects play a role.

2.4.1 Perfect swapping Case: Percolation Threshold

With $p_{hop} = 1$, the dynamics is deterministic, with particles moving in a chiral fashion along edges while performing localized trajectories in the bulk. Importantly, the chiral flow in this case is robust against geometric deformations as shown in our previous work [1]. Therefore the flow across the system given a specific disorder realization is simply determined by whether a percolating cluster can be formed, and the disorder average flow should exhibit a percolation threshold as function of the local vacancy probability p_α . We numerically study the mean chiral flow per cycle as a function of the site vacancy probability p_α averaged over disorder realizations in the perfect swapping case. We denote chiral flow as F and mean chiral flow averaged over disorder realizations as $\langle F \rangle$.

In Fig 2.7(a), we set the linear system site to take values $L = 25, 33, 41$. We observe that at low disorder, the mean flow per cycle $\langle F \rangle$ is close to unity. Increasing the probability of site vacancy eventually causes the flow to drop sharply to zero chiral flow, with a sharper percolation threshold expected as we increase L .

The disorder averaged $\langle F \rangle$ at different linear lattice sizes intersect around $p_c \approx 0.26$ in Fig 2.7(a), roughly matching the peak fluctuations (standard deviation) in the chiral flow across disorder realization in Fig 2.7(b). To understand the critical properties of the flow near percolation threshold in the perfect swapping case, we note that since F determines whether a percolating cluster exists in a given disorder configuration, having the values 1 (if percolating cluster exists) or 0 (if no percolating cluster exists). When taken as an average over different disorder configurations, $\langle F(p_\alpha, p_{hop} = 1) \rangle$ then gives the probability that a percolating cluster exists.

The percolation threshold p_c we obtained matches with the earlier result on 2D site percolation in Lieb lattice in an earlier work [80], but there we should interpret the result by mapping $p_\alpha \rightarrow 1 - p$ as we starts with a filled Lieb lattice and adding in site vacancy when tuning up p_α , while [80] starts with empty Lieb lattice and gradually filling the lattice sites.

Given that disorder averaged $\langle F \rangle$ gives the probability that a concentration p_α gives a percolating cluster, according to the classic percolation theory [81], we then expect such quantity to exhibit finite size ansatz of the form $\langle F \rangle = f((p_\alpha - p_c)L^{1/\nu})$ to describe the percolation threshold around $p_c \approx 0.26$. We find that the critical exponent obtained is around $\nu \approx 1.35$, which roughly coincide with the 2D site percolating Lieb lattice result in [80]. The fluctuations of the mean chiral flow across disorder realizations also peak around the percolation threshold $p_c \sim 0.26$, and the size of peak increasing with system length L as shown in the middle panel in Fig 2.7.

2.4.2 Away from Perfect swapping: Crossover

Away from the perfect swapping case, the flow ceases to be robust over a finite range of disorder and drops as soon as we introduce site dilution, as shown in Figure 2.8 (a) and (b). The sharp transition feature we have observed in the perfect swapping case is therefore specific to the perfect swapping case, where we have deterministic walks rather than random walk for the case of finite hopping probability $p_{hop} < 1$, where now both random walks and site percolation affect the chiral flow rate in our study.

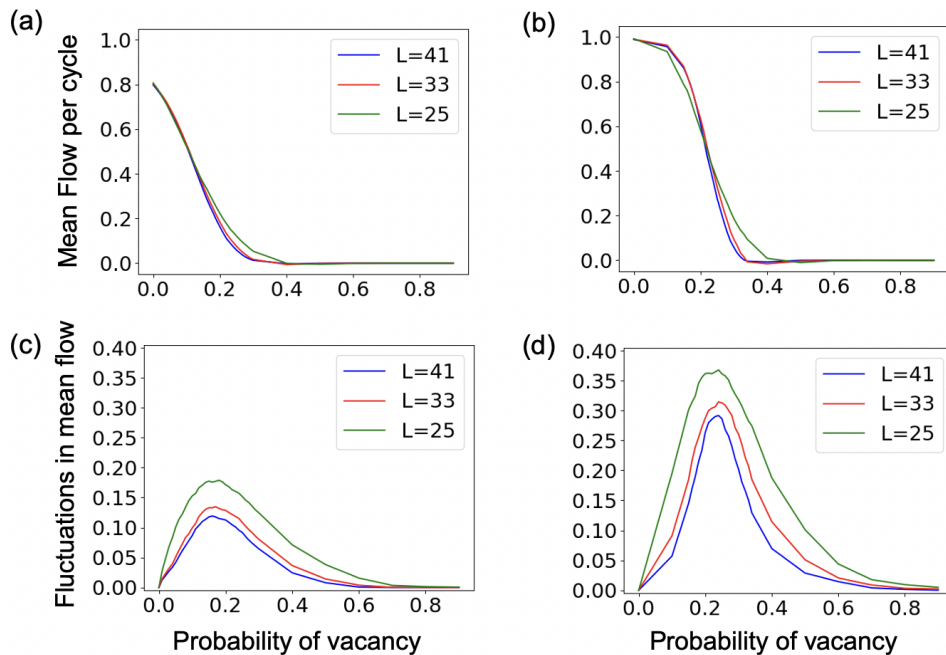


FIGURE 2.8: (a) Mean flow per cycle for $p_{hop} = 0.8$ and (b) for $p_{hop} = 0.95$, averaged over 1000 disorder configurations, (c) Fluctuations (standard deviation) of the mean flow per cycle for $p_{hop} = 0.8$ and (d) for $p_{hop} = 0.95$ over across 1000 disorder realizations for various system sizes L . Note that in contrast to the $p_{hop} = 1$ case, the fluctuation decreases as a function of system sizes, signifying a crossover. $p_{hop} < 0.8$ has similar qualitative features for the mean flow per cycle curve as that of $p_{hop} = 0.8$ and a less pronounced fluctuation.

Another distinction with the perfect swapping case can be seen from the fluctuations in the chiral flow rate across disorder realizations as shown in Figure 2.8 (c) and (d). In contrast with the perfect swapping case (where fluctuation of the flow increases

with system size), the fluctuation of the flow decreases as we increase the system size. The averaged flow across disorder no longer exhibits sharp percolating threshold, unlike the perfect swapping case.

The physical reason for the difference is that the flow is a quantity that is affected by both the hopping probability and site vacancy, and in the case of random walk $p_{hop} < 1$ both factors affect the late time chiral flow per cycle, obscuring contributions from site vacancy (geometric percolation) alone. This is not an issue for perfect swapping case, where the only factor affecting the flow is geometrical. Finally, we present a contour plot of the mean chiral flow per cycle across disorder realizations with 2 parameters of interest here in Figure 2.9: the hopping probability p_{hop} and the probability of blockade disorder p_α .

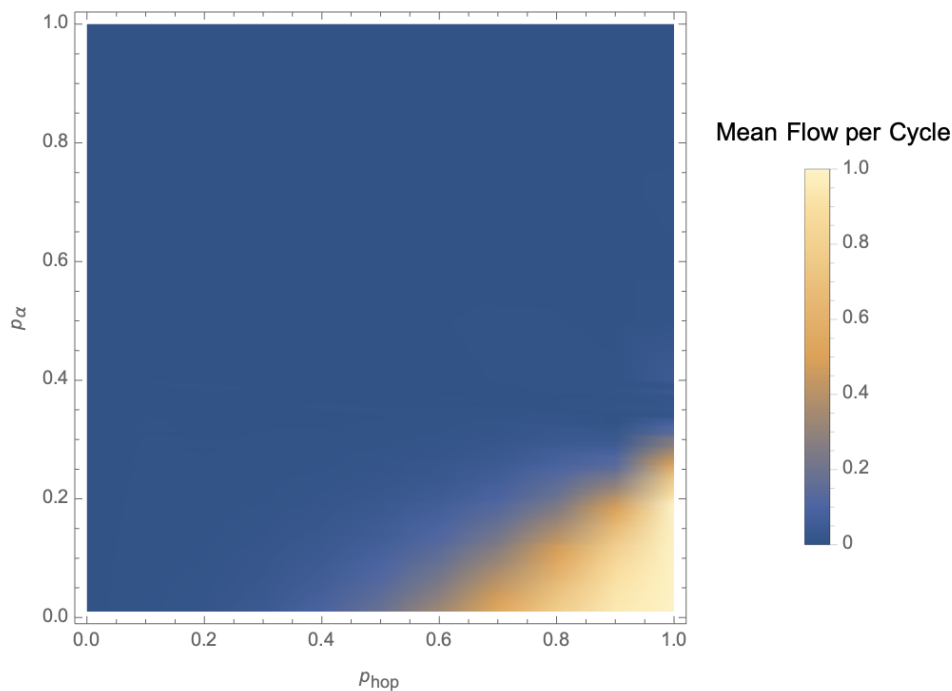


FIGURE 2.9: 2D plot of the mean chiral flow per cycle for site vacancy for a 33×33 Lieb lattice, averaged over 1000 disorder realizations. The horizontal axis represents hopping probability p_{hop} and the vertical axis is the probability of vacancy in the lattice p_α . The percolation transition happens on the line $p_{hop} = 1$.

A comment is in order for stochastic random walks on lattice with site vacancies.

In [82], particle diffusion was studied in the context of site percolation. When no percolating cluster can be formed (in our convention, $p_\alpha > p_c$), the mean square spreading $\langle r^2 \rangle = \text{const}$ in late time dynamics for a particle undergoing diffusive behaviour. In another limit when percolating cluster can always be formed ($p_\alpha < p_c$), we have normal diffusive behaviour $\langle r^2 \rangle = Dt$ in late time. However, interesting anomalous diffusive behaviour occurs right at $p_\alpha = p_c$ according to [81, 82], where $\langle r^2 \rangle \propto t^{2/3}$. While we have not investigated diffusive transport for the case of site vacancy disorder, this will constitute an interesting point to investigate.

2.5 Lattice Distortion and Onsite Potential disorder

We next investigate two additional models of disorder. Namely, we consider the case where the hopping parameter strength between sites is disordered and the case where a random on-site potential is applied to each site (represented in Figs. 2.1c and 2.1b respectively with explicit details for each model below). We will again restrict ourselves to the Zeno limit, leaving results on the effects of disorder away from the Zeno limit to Section 2.6.

The first model we consider is the application of the measurement protocol to a Lieb lattice with the random hopping Hamiltonian

$$H = - \sum_{\langle \mathbf{r}\mathbf{r}' \rangle} t_{\mathbf{r}\mathbf{r}'} a_{\mathbf{r}}^\dagger a_{\mathbf{r}'}, \quad (2.18)$$

where $t_{\mathbf{r}\mathbf{r}'}$ is now a random variable drawn from the uniform random distribution $[-\delta t + 1, \delta t + 1]$, i.e. we set the mean of $\langle t_{\mathbf{r}\mathbf{r}'} \rangle = 1$ with disorder strength δt , which we allow to be at $\max |\delta t| \leq 1$. Hopping disorder is associated with random lattice distortion, with distances between lattice sites randomly lengthened or shortened, leading to an alteration in the hopping integral t_{hop} between sites.

In the Zeno limit, we calculate the transition matrix R_i which characterizes the evolution for the i^{th} step of the measurement protocol with the random hopping disorder, replacing Eq. (2.5) with

$$R_i = \oplus_{\langle \mathbf{r}, \mathbf{r}' \rangle \in A_i} \begin{pmatrix} 1 - p_{\text{hop}, \mathbf{r}\mathbf{r}'} & p_{\text{hop}, \mathbf{r}\mathbf{r}'} \\ p_{\text{hop}, \mathbf{r}\mathbf{r}'} & 1 - p_{\text{hop}, \mathbf{r}\mathbf{r}'} \end{pmatrix} \oplus_{\text{other sites}} I \quad (2.19)$$

and the hopping probability depends on $t_{\mathbf{r}\mathbf{r}'}$ via

$$p_{\text{hop}, \mathbf{r}\mathbf{r}'} = \sin^2\left(\frac{t_{\mathbf{r}\mathbf{r}'} T}{8}\right).$$

In other words, the random hopping Hamiltonian translates to a periodic random walk where different links have different hopping probabilities.

The second disorder model we study in this section is a random on-site potential. We note that it was shown in [33] that this variety of disorder, when added to the Floquet model of Rudner et. al. [29], may prevent bulk diffusion (due to Anderson localization) while still preserving protected edge transport. Such a system is referred to as an anomalous Floquet-Anderson Insulator.

We note that, in the measurement-induced model, the diffusive behavior in the bulk is expected even when a disordered potential is present. This occurs even if the disorder is sufficient to result in Anderson localization in the absence of measurements. Indeed, Anderson localization is a wave effect that emerges due to interference within a single particle wave function as it moves through a random potential. The projective measurements rapidly collapse the wave function to single sites within the lattice, thus no interference is possible ruining Anderson localization (as long as the distance between measured sites is smaller than the expected localization length). We note, however, that Anderson localization physics may still play a role in the limit where the measurements are temporally and spatially sparse enough [72].

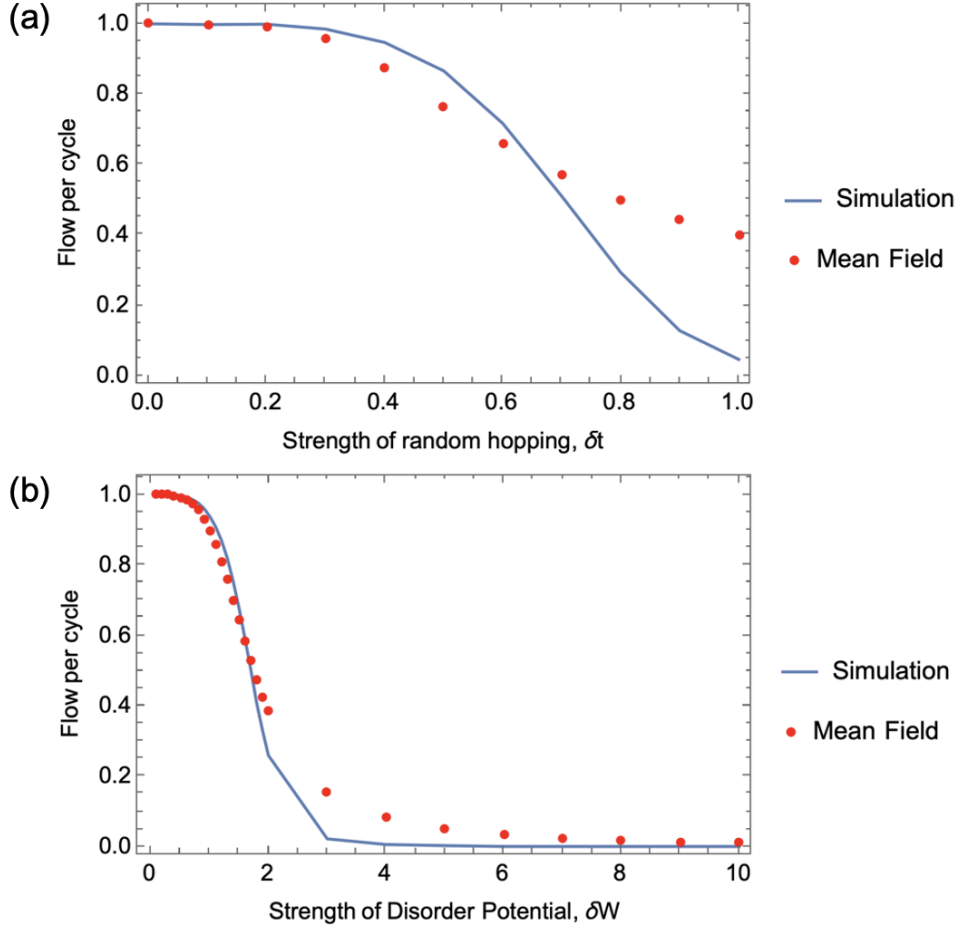


FIGURE 2.10: (a) The mean Flow per cycle for the case of random hopping strength δt and (b) The mean Flow per cycle for the case of random potential δW . Here the line represents numerical simulation taken on a 33×33 Lieb lattice averaged over 1000 disorder realization, and is compared to the mean field result (dot) outlined in the main text.

In this section, we analyze in detail the effect of the disorder on the diffusion constant as well as its effect on the chiral edge flow. We also present a mean-field type argument which approximately captures these effects.

The Hamiltonian for the case with random on-site potential takes the form

$$H = -t_{hop} \sum_{\langle \mathbf{r}\mathbf{r}' \rangle} a_{\mathbf{r}}^{\dagger} a_{\mathbf{r}'} + \sum_{\mathbf{r}} W_{\mathbf{r}} a_{\mathbf{r}}^{\dagger} a_{\mathbf{r}}, \quad (2.20)$$

where $W_{\mathbf{r}}$ is sampled from the random uniform distribution $W_{\mathbf{r}} \in [-\delta W, \delta W]$. We set

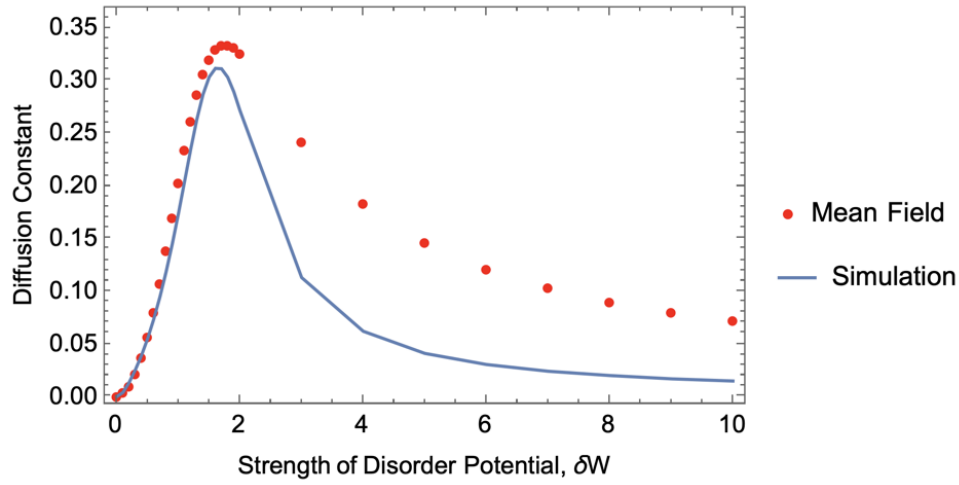


FIGURE 2.11: The mean diffusion constant as a function of the strength of disorder potential for system with random onsite potential averaged over 1000 disorder realizations in the Zeno limit. Here $T = 4\pi$ corresponds the perfect swapping case in the clean limit without any diffusion. The mean diffusion constant from the crude mean field treatment agrees with the numerical simulations for weak disorder.

$t_{hop} = 1$ and $T = 4\pi$ in our numerical results below, while we keep the variable t_{hop} and T in the our expression of the random stochastic transition matrix below (Eqn 2.21). The random stochastic transfer matrix describing two neighboring unmeasured sites \mathbf{r} and \mathbf{r}' is (surrounded by measured sites and in the Zeno limit) takes the form with R_i from Eqn 2.19 with $p_{hop,\mathbf{r}\mathbf{r}'}$ taking the form below instead (for derivation see Appendix 2.C)

$$p_{hop,\mathbf{r}\mathbf{r}'} = \frac{2t_{hop}^2 (1 - \cos\left(\frac{T}{8} \sqrt{4t_{hop}^2 + (W_{\mathbf{r}} - W_{\mathbf{r}'})^2}\right))}{4t_{hop}^2 + (W_{\mathbf{r}} - W_{\mathbf{r}'})^2}. \quad (2.21)$$

Let us unpack Eq 2.21. For low disorder, the typical chemical potential difference between adjacent lattice sites is small and the model is close to the mean hopping probability p_{hop} determined by T . As disorder strength increases, the denominator grows while the numerator stays bounded by the cosine function, leading to the hopping probability to zero (thereby freezing the dynamics) due to huge potential difference.

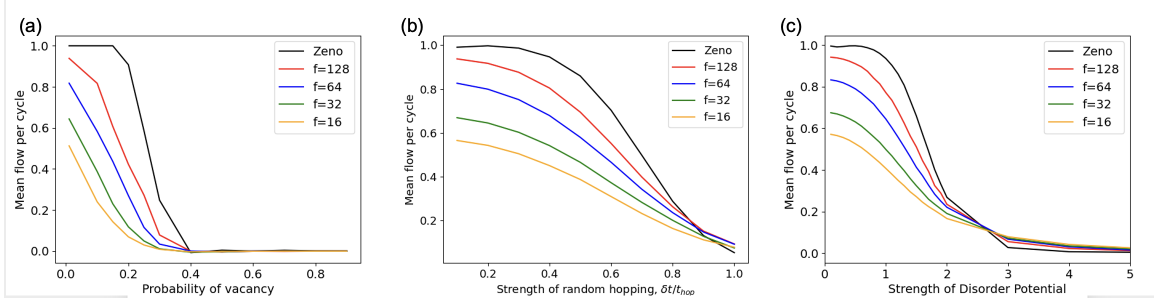


FIGURE 2.12: Comparison between flow per cycle for the case of (a) site vacancy, (b) random hopping strength, and (c) disordered potential. The comparisons are made across different measurement frequencies against the Zeno limit case and in all cases the lattice size is 33×33 and averaged across 1000 disorder realizations.

Let us interpret the numerical results on the mean chiral flow per cycle and diffusion constant for the case of random onsite potential as shown in Fig 2.10 (b) and 2.11 respectively. In the intermediate disorder strength, we have an interesting situation where chirality is partially suppressed but diffusion transport proliferates as shown in Fig 2.10 and 2.11 respectively. This can be understood in that in the intermediate disorder strength we have a random bond model where many links takes intermediate hopping probability $0 < p_{hop,rr'} < 1$. In the intermediate disorder case with random walk, diffusion is more pronounced than in the case close to perfect swapping (with deterministic walk) or freezing (with $p_{hop} \approx 0$). In the strong disorder case, we again have strong localization in both the measurement induced chiral transport and diffusive transport.

In the limit of weak disorder, we can estimate the flow by computing the spatial average of $p_{hop,rr'}$ at different links and using the resulting spatially averaged \bar{p}_{hop} as the effective hopping probability in Eqn (2.12) to compute the flow transport in a translationally invariant system to get the effective flow. In this sense, we call this approach the 'mean-field' approach, where we replace a disordered model with inhomogeneous hopping probability $p_{hop,rr'}$ at different links with homogeneous \bar{p}_{hop} over all links, and

treat it as if it has translational invariance. The inhomogeneity in the hopping probability at different links in a disordered model can be caused by random hopping strength or random onsite potential.

For the case of random hopping, the effective hopping \bar{p}_{hop} is given by averaging

$$\bar{p}_{hop}(\delta t, t_{hop}) = \int_{t_{hop}-\delta t}^{t_{hop}+\delta t} dt_{\mathbf{r}\mathbf{r}'} \sin\left(\frac{t_{\mathbf{r}\mathbf{r}'} T}{8}\right). \quad (2.22)$$

We compute F using the translational invariant formula Eqn (2.12) using \bar{p}_{hop} for various δt and compare with direct numerical simulations in Fig 2.10 (a). As expected, the agreement goes well for small and intermediate $\delta t \sim 0.3$ relative to $t_{hop} = 1$ before deviation occurs for larger δt .

In the presence of potential disorder, the average hopping probability as function of disorder strength δW and hopping t_{hop} is

$$\begin{aligned} \bar{p}_{hop}(\delta W, t_{hop}) = & \frac{1}{4\delta W^2} \int_{-\delta W}^{\delta W} \int_{-\delta W}^{\delta W} dW_{\mathbf{r}} dW_{\mathbf{r}'} \times \\ & \frac{2t_{hop}^2 (1 - \cos\left(\frac{T}{8} \sqrt{4t_{hop}^2 + (W_{\mathbf{r}} - W_{\mathbf{r}'})^2}\right))}{4t_{hop}^2 + (W_{\mathbf{r}} - W_{\mathbf{r}'})^2}. \end{aligned} \quad (2.23)$$

In Fig. 2.10(b) we show the effective ‘mean-field’ result vs numerical simulations of the disordered system, and similarly find good agreement at weak disorder. Note that both numerically and mean field approximation show that large disorder leads to an effective suppression of flow.

We also performed the ‘mean-field’ approach to evaluate the diffusion constant for the case of random onsite potential in Fig 2.11. In this case, the diffusion constant for the mean-field approach agrees with numerical simulation for weak disorder, but is not as tight for intermediate disorder compared to its use in for estimating the flow 2.10. It is interesting to note that the maximal diffusion coefficient coincides with the region where the drop in chiral flow as function of disorder strength is the steepest.

We emphasize that the actual flow depends in a complicated nonlinear way on the particular disorder realization, therefore we can only expect the above approach to work in the weak disorder limit, where fluctuations in $p_{hop,rr'}$ are small.

In the next section we turn to consider all variety of disorders considered in this paper away from the Zeno limit in the next section.

2.6 Numerical Results Away from Zeno Limit

We now investigate the effect of relaxing the Zeno limit assumption on our measurement protocol in the chiral flow transport in various disordered systems we previously simulated. In Figure 2.12, we study the cases of site vacancy, random hopping strength and random onsite potential against finite measurement frequencies of 16, 32, 64, and 128 measurements per measurement step (8 measurement steps make up a measurement cycle in our protocol).

Intuitively, the overall effect of reducing measurement frequency will tend to reduce the amount of chiral flow transport in our systems, as shown in Fig 2.12. In Figure 2.12 (a), we study site vacancy disorder where we set $T = 4\pi$, which in the Zeno limit corresponds to perfect swapping. The robustness of the chiral flow to low disorder in the Zeno limit disappears as soon as we tune the measurement frequency away from the Zeno limit and the chiral flow starts decreasing as soon as we introduce disorder. The same feature of the lack of robustness against (global) minute disorder are also seen with the random hopping strength in Fig 2.12 (b) and random onsite potential in Fig 2.12 (c).

Nonetheless, we would like to note the interesting case of random onsite potential in Fig 2.12(c). Near the clean limit, we expect that lowering the measurement frequency will lower the chiral flow. Meanwhile, strong disorder limit suppresses both diffusive

and chiral transport in our half-filled system. In a finite window of intermediate onsite disorder strength, however, decreasing the measurement frequency actually enhances the chiral flow. However, whether this effect is an artifact of finite size/time effect, or a genuine non-trivial effect arising from the interplay between chiral flow and diffusive spreading, is currently unknown and this is a possible avenue for future work.

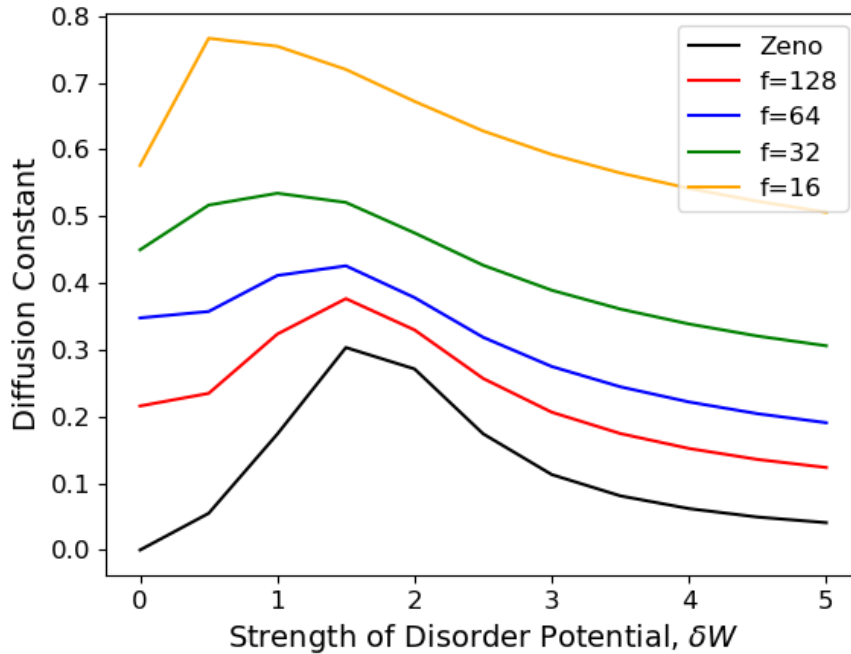


FIGURE 2.13: Diffusion constant for various measurement frequencies (and the previous Zeno limit result in 2.11) as a function of disorder potential strength δW , simulated with $T = 4\pi$ over 1000 disorder realizations.

Finally, we turn our attention to diffusive dynamics, specializing in the case of diffusion constant of the measurement-induced chiral system under random onsite potential away from the Zeno limit. The diffusion constant generally increases as the measurement frequency is decreased away from the Zeno limit, which aligns with the intuition that away from the Zeno limit particle dynamics in our measurement protocol becomes more diffusive. The result is presented in Fig 2.13, where we fix $T = 4\pi$ for all measurement frequencies.

2.7 Discussions and Outlook

In this work we presented a systematic investigation on the diffusive dynamics and the effect of disorder on measurement-induced chirality exhibited by free fermions under various disorder types. In particular, there is a putative percolation transition-like behavior exhibited by the mean chiral flow of the particles in site blockade disorder in the disorder limit. It is also noteworthy that our measurement protocol in general is reliably robust to the introduction to global disorder, with mean chiral flow rate decreasing significantly only when disorder strengths are significant. Finally, we also provided various analytical mean field picture to describe the random hopping and random onsite potential cases and the agreement holds up to significant disorder.

It is an interesting question whether the behavior we find persists if the disorder were time dependent. In standard quantum systems, a time-dependent disorder is fundamentally different from a quenched disorder (e.g. Anderson localization is absent in the dynamic case [83]). Because of the time-dependent protocol used for measurement-induced chirality, we speculate that dynamic disorder should result, in the same behavior as the quenched disorder we consider above, at least in the Zeno limit. However, as the rate of measurement drops, corrections due to coherent behavior and localization phenomena may start appearing at intermediate times. The investigation of time dependent random potentials in the low measurement frequency limit would be an interesting direction for additional work.

Several comments are in order regarding the relation of our work to recent relevant literature. This work analyzed the average transport and dynamics of densities over all possible measurement outcomes and averaged over different disorder realizations. The recent work by Pöpperl *et. al.* [72] studies particular quantum trajectories (measurement outcomes) of the particle density profile using wavefunctional approach (while we used density matrices instead) with different interesting averages for a 1D

fermion on an Anderson localized chain. [69] also studied free fermions on 1D Anderson chain, but has focused primarily on entanglement properties.

We now turn to discuss open problems and possible avenue for future work in the general direction of measurement-induced chirality. First, it would be interesting to define an effective "cyclotron frequency" $\omega_{eff} \sim 1/T$ which is proportional to an effective magnetic field B_{eff} for this kind of system. This is inspired by analogy of our measurement-induced chiral flow to the anomalous Floquet topological insulator proposed in [29] and would constitute an interesting subproblem to develop the idea further.

Various interesting investigations can also be further explored on the diffusive dynamics in for monitored fermions exhibiting measurement-induced chirality. It will be interesting to investigate to see if statements can be made about how the diffusion coefficient in the diffusion dynamics from an occupied region to the empty in our setup can be related to Fick's law. Another interesting thought to exploration is the question of describing an effective electrical resistance for our system given the diffusion constants for our system.

Finally, one could also extend the question of measurement-induced transports to measurement-induced delocalization transitions [72] and other interesting quantum walk behaviours [84, 85] caused by different types of measurements. The direction of using measurement to engineer interesting transport and dynamics is a nascent and new area of research that could potentially lead to more interesting discoveries.

Appendix

2.A Derivation for the analytical expression for the Diffusion constant

In this Appendix, we derive the expression Eq 2.17 from the definition Eq 2.16 using a translationally invariant setup in Figure 2.A.1 and working in momentum space. The setup is shown in Figure 2.A.1.

We define a set of consistent Fourier transformation by using the following conventions

$$\begin{aligned}
 R_{cyc}(\mathbf{r}, \mu; \mathbf{r}', \nu) &= \int \frac{d^2k}{(2\pi)^2} R_B(\mathbf{k}, \mu, \nu) e^{i\mathbf{k}(\mathbf{r}-\mathbf{r}')} , R_B(\mathbf{k}, \mu, \nu) \\
 &= \sum_{(\mathbf{r}-\mathbf{r}')} e^{-i\mathbf{k}(\mathbf{r}-\mathbf{r}')} R_{cyc}(\mathbf{r}, \mu; \mathbf{r}', \nu)
 \end{aligned} \tag{2.24}$$

where $V = L_x L_y$. Here, we would like to make two remarks about our convention. (1) The matrix $R_{cyc}(\mathbf{r}, \mu; \mathbf{r}', \nu)$ is only dependent on the difference $\mathbf{r} - \mathbf{r}'$, by making use of the translational invariance, hence Eq 2.24. (2) We count distance a little differently than how one would normally count distance for setup with unit cell decomposition. Normally, one only keeps track of the distance between different unit cell in the expression $(\mathbf{r} - \mathbf{r}')$ in Eq 2.24. However, as our numerical calculation keeps track of distance between lattice sites rather than unit cells, we will do likewise for our k -space calculation for consistency.

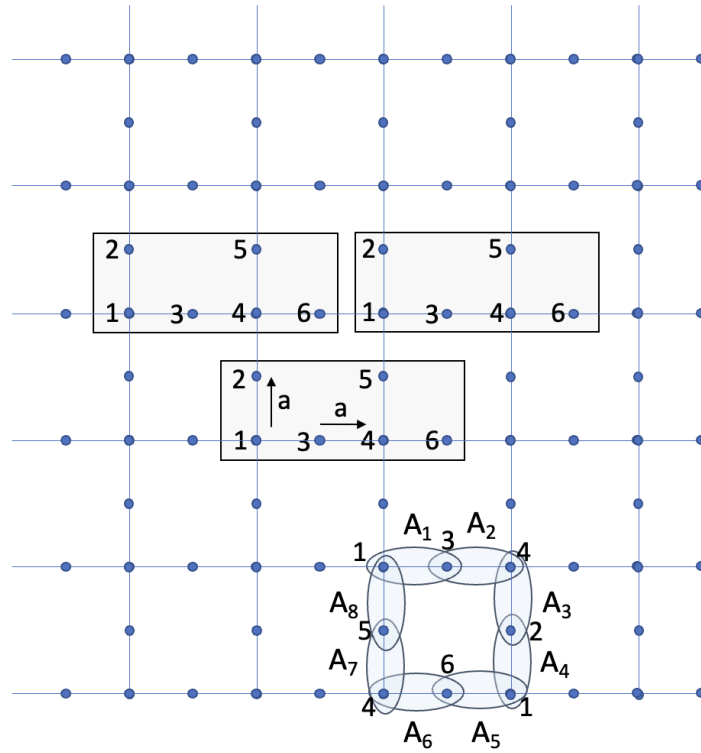


FIGURE 2.A.1: The Lieb lattice is divided into 6 lattice sites per unit cell, and the set of unmeasured sites in each step is shown as A_i in the Figure. Here, we note that we count the distance between neighbouring lattice sites with lattice constant a (conveniently set to 1) rather than counting that as the inter-unit cell distance in typical systems for consistency with numerical simulation when computing the diffusion constant D .

For example, the k -space $R_5(\mathbf{k}, \theta)$ and $R_4(\mathbf{k}, \theta)$ are 6×6 matrices of the following form respectively

$$R_5(\mathbf{k}, \theta) = \begin{pmatrix} 1-p & 0 & 0 & 0 & 0 & pe^{-ik_x} \\ 0 & 1 & 0 & 0 & 0 & 0 \\ 0 & 0 & 1 & 0 & 0 & 0 \\ 0 & 0 & 0 & 1 & 0 & 0 \\ 0 & 0 & 0 & 0 & 1 & 0 \\ pe^{ik_x} & 0 & 0 & 0 & 0 & 1-p \end{pmatrix}, R_4(\mathbf{k}, \theta) = \begin{pmatrix} 1-p & pe^{ik_y}e^{i\theta} & 0 & 0 & 0 & 0 \\ pe^{-ik_y}e^{-i\theta} & 1-p & 0 & 0 & 0 & 0 \\ 0 & 0 & 1 & 0 & 0 & 0 \\ 0 & 0 & 0 & 1 & 0 & 0 \\ 0 & 0 & 0 & 0 & 1 & 0 \\ 0 & 0 & 0 & 0 & 0 & 1 \end{pmatrix}$$

and we can construct $R_B(\mathbf{k}, \theta) = R_8 R_7 R_6 R_5 R_4 R_3 R_2 R_1$ based on this construct of the

k -space stochastic transition matrices by keeping track of the factors e^{-ik_x} whenever the particle hops to the right and $e^{-ik_y}e^{-i\theta}$ whenever the particle hops upward, and vice versa for the left and downward hopping elements, and θ is the counting field keeping track of the vertical flow alone in our setup.

Starting from Eq 2.16, which we reproduce here for convenience,

$$\begin{aligned}
\mathbf{r}_{mean}(t = 8N) &\equiv \frac{\sum_{\mathbf{r}} \mathbf{r} G_{\mathbf{r}\mathbf{r}}(t = 8N)}{\sum_{\mathbf{r}} G_{\mathbf{r}\mathbf{r}}(t = 8N)}, \\
\langle \Delta r^2(t = 8N) \rangle &\equiv \frac{\sum_{\mathbf{r}} (\mathbf{r} - \mathbf{r}_{mean}(t = 8N))^2 G_{\mathbf{r}\mathbf{r}}(t = 8N)}{\sum_{\mathbf{r}} G_{\mathbf{r}\mathbf{r}}(t = 8N)}, \\
D &= \lim_{N \rightarrow \infty} \frac{\langle \Delta r^2(t = 8N) \rangle - \langle \Delta r^2(t = 0) \rangle}{8N} \quad (2.25)
\end{aligned}$$

For the term $\sum_{\mathbf{r}} (\mathbf{r} - \mathbf{r}_{mean})^2 G_{\mathbf{r}\mathbf{r}}(t = 8N)$ term, we simplify to get

$$\sum_{\mathbf{r}} (\mathbf{r} - \mathbf{r}_{mean})^2 G_{\mathbf{r}\mathbf{r}}(t = 8N) = \sum_{\mathbf{r}} r^2 G_{\mathbf{r}\mathbf{r}}(t = 8N) - r_{mean}^2(t = 8N) \quad (2.26)$$

We Fourier transform the real space $G_{\mathbf{r}'\mathbf{r}}(t = 8N) \equiv (R_{cyc}^N)_{\mathbf{r}'\mathbf{r}} |g_{\mathbf{r}}(t = 0)\rangle$ according to Eq 2.24 in the definition $\langle \Delta r^2 \rangle$. In our current setup, we start with a single particle with unit density placed on the origin so that $\langle \Delta r^2(t = 0) \rangle = 0$, and since there is no injection and extraction, particle number is conserved and we have $\sum_{\mathbf{r}} G_{\mathbf{r}\mathbf{r}} = 1$ at all

times. Focusing on the $\sum_{\mathbf{r}} r^2 (R_{cyc}^N)_{\mathbf{r}\mathbf{r}'} |g_{\mathbf{r}'}(t=0)\rangle$ term, we have

$$\begin{aligned}
\sum_{\mathbf{r},\mu} r^2 (R_{cyc}^N)_{(\mathbf{r},\mu),(\mathbf{r}',\nu)} |g_{\mathbf{r}',\nu}(t=0)\rangle &= \sum_{\mathbf{r},\mu} r^2 (R_{cyc}^N)_{(\mathbf{r},\mu),(0,1)} = \sum_{\mathbf{r},\mu} \int \frac{d^2\mathbf{k}}{(2\pi)^2} r^2 e^{i\mathbf{k}\mathbf{r}} (R_B^N(\mathbf{k}))_{\mu,1} \\
&= \sum_{\mathbf{r},\mu} \int \frac{d^2\mathbf{k}}{(2\pi)^2} (-\nabla_{\mathbf{k}}^2 e^{i\mathbf{k}\mathbf{r}}) (R_B^N(\mathbf{k}))_{\mu,1} \\
&= \sum_{\mathbf{r},\mu} \int \frac{d^2\mathbf{k}}{(2\pi)^2} e^{i\mathbf{k}\mathbf{r}} (-\nabla_{\mathbf{k}}^2 R_B^N(\mathbf{k}))_{\mu,1} \\
&= \sum_{\mu} \int d^2\mathbf{k} \delta^2(\mathbf{k}) (-\nabla_{\mathbf{k}}^2 R_B^N(\mathbf{k}))_{\mu,1} \\
&= \sum_{\mu=1}^6 [-\nabla_{\mathbf{k}}^2 R_B^N(\mathbf{k})|_{\mathbf{k}=0}]_{\mu,1}. \tag{2.27}
\end{aligned}$$

In the first line, we make use of the fact that $|g_{\mathbf{r}',\nu}(t=0)\rangle = \delta_{\mathbf{r}',0}\delta_{\nu,1}$. In the second line, we use the fact that $r^2 e^{i\mathbf{k}\mathbf{r}} = -\nabla_{\mathbf{k}}^2 e^{i\mathbf{k}\mathbf{r}}$ and we integrate by part. From the second to the third line, we summed over \mathbf{r} with $\sum_{\mathbf{r}} e^{-i\mathbf{k}\mathbf{r}} = (2\pi)^2 \delta^2(\mathbf{k})$ and finally we integrate with the delta function to arrive at our final expression.

For the \mathbf{r}_{mean}^2 term, we perform similar computation as the one above to get

$$\begin{aligned}
\mathbf{r}_{mean}^2 &= \left[\sum_{\mathbf{r},\mu} \mathbf{r} (R_{cyc}^N)_{(\mathbf{r},\mu),(0,1)} \right] \cdot \left[\sum_{\mathbf{r}',\mu'} \mathbf{r} (R_{cyc}^N)_{(\mathbf{r}',\mu'),(0,1)} \right] \\
&= \left[\sum_{\mu=1}^6 [-i\nabla_{\mathbf{k}} R_B^N(\mathbf{k})|_{\mathbf{k}=0}]_{\mu,1} \right] \cdot \left[\sum_{\mu'=1}^6 [-i\nabla_{\mathbf{k}'} R_B^N(\mathbf{k}')|_{\mathbf{k}'=0}]_{\mu',1} \right] \\
&= - \left[\sum_{\mu=1}^6 [\partial_{k_x} R_B^N(\mathbf{k})|_{\mathbf{k}=0}]_{\mu,1} \right]^2 - \left[\sum_{\mu=1}^6 [\partial_{k_y} R_B^N(\mathbf{k})|_{\mathbf{k}=0}]_{\mu,1} \right]^2. \tag{2.28}
\end{aligned}$$

Collecting both terms Eq 2.27 and Eq 2.28, we get Eq 2.17.

2.B Extraction of the late time dynamics of the mean flow per cycle on a finite size lattice

We comment on the approach we take to extract the late time chiral mean flow per cycle in a finite size system. Given the geometry shown in Figure 2.B.1, there will be both chiral transport and diffusive transport in our measurement protocol away from the perfect swapping case or away from the Zeno limit. In an infinitely large half-filled system, both chiral and diffusive transport will continue forever without significant boundary effect from the lattice. Nonetheless, in a finite size system, the late time flow of our measurement protocol can be altered after significant amount of particle diffuses to the boundary of the Lieb lattice rather than transported solely via chiral motion (see Fig 2.B.1).

To account for this effect, we therefore extract the chiral flow rate of our lattice system by averaging about 5 cycles before the *cumulative* density of particles at the upper right half edge (see Fig 2.B.1) becomes significantly populated at some cutoff total density $\rho_{cutoff} \sim 0.1$. Here we track the *cumulative* sum of density of particles that has *ever* arrived at these sites as we immediately extract these particles after each protocol step. We then extract a t_{cutoff} that happens when ρ_{cutoff} reaches 0.1 and we averaged 5 measurement cycles around t_{cutoff} for our late time dynamics.

In the main article, except in the particular case of site vacancy disorder in the perfect swapping Zeno limit, where the protected chiral edge flow dynamics is deterministic ($p_{hop} = 1$) and not random (thereby diffusive dynamics is absent), we generally apply this approach for the extraction of the late time chiral flow dynamics. The diffusive behaviour is present in all other disorder cases (both in and out of Zeno limit).

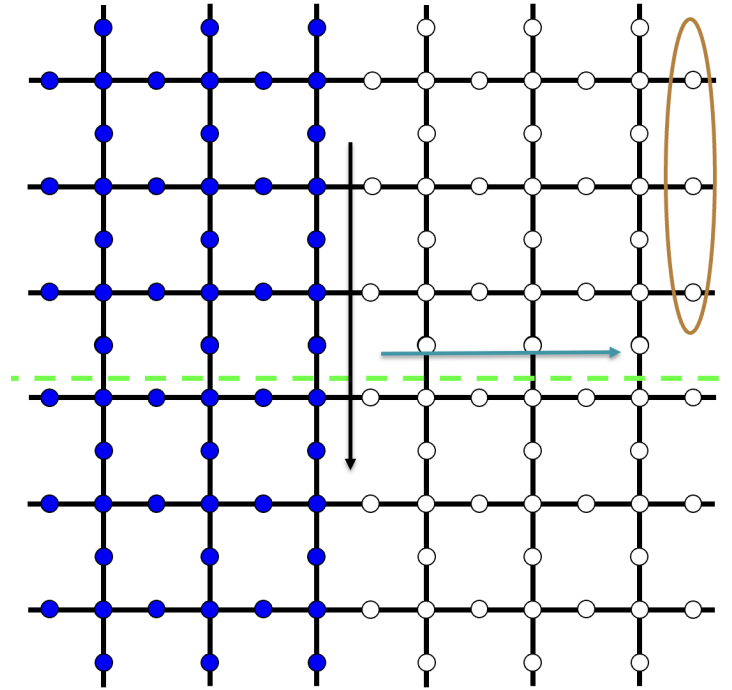


FIGURE 2.B.1: In our measurement protocol, the net chiral flow is measured by the number of particles transported along the direction of the black arrow. The diffusive transport takes place along the transverse direction (the direction of the grey arrow). We constantly inject particle on the left edge of the lattice and extract particle on the right edge. We keep track of the particle density at the top half edge of the lattice (circled sites) prior to extraction to truncate and obtain the late time chiral flow per cycle in the vicinity of the time steps.

2.C Derivation of the stochastic transition matrix for the random onsite potential disorder

We outline the derivation of Eq 2.21 in this Appendix. We start off with the matrix form of the Hamiltonian and focusing on 2 unmeasured sites r and r' in the Zeno limit, where

the Hamiltonian H_{zeno} is allowed to evolve for time $t = \frac{T}{8}$ now takes the form (calculated using Mathematica)

$$\begin{aligned}
 U_{zeno} &= \begin{pmatrix} U_{11} & U_{12} \\ U_{21} & U_{22} \end{pmatrix}, \tag{2.30} \\
 U_{11} &= \exp\left(-i\frac{T}{8}\frac{(W_{\mathbf{r}} + W_{\mathbf{r}'})}{2}\right) \left(\cos\left(\frac{1}{2}\frac{T}{8}\sqrt{4t_{hop}^2 + (W_{\mathbf{r}} - W_{\mathbf{r}'})^2}\right) \right. \\
 &\quad \left. - \frac{i \sin\left(\frac{1}{2}\frac{T}{8}\sqrt{4t_{hop}^2 + (W_{\mathbf{r}} - W_{\mathbf{r}'})^2}\right)(W_{\mathbf{r}} - W_{\mathbf{r}'})}{\sqrt{4t_{hop}^2 + (W_{\mathbf{r}} - W_{\mathbf{r}'})^2}} \right) \\
 U_{22} &= \exp\left(-i\frac{T}{8}\frac{(W_{\mathbf{r}} + W_{\mathbf{r}'})}{2}\right) \left(\cos\left(\frac{1}{2}\frac{T}{8}\sqrt{4t_{hop}^2 + (W_{\mathbf{r}} - W_{\mathbf{r}'})^2}\right) \right. \\
 &\quad \left. + \frac{i \sin\left(\frac{1}{2}\frac{T}{8}\sqrt{4t_{hop}^2 + (W_{\mathbf{r}} - W_{\mathbf{r}'})^2}\right)(W_{\mathbf{r}} - W_{\mathbf{r}'})}{\sqrt{4t_{hop}^2 + (W_{\mathbf{r}} - W_{\mathbf{r}'})^2}} \right) \\
 U_{12} = U_{21} &= \frac{2i \exp\left(-i\frac{T}{8}\frac{(W_{\mathbf{r}} + W_{\mathbf{r}'})}{2}\right) \sin\left(\frac{1}{2}\frac{T}{8}\sqrt{4t_{hop}^2 + (W_{\mathbf{r}} - W_{\mathbf{r}'})^2}\right)}{\sqrt{4t_{hop}^2 + (W_{\mathbf{r}} - W_{\mathbf{r}'})^2}}.
 \end{aligned}$$

For an initial distribution $G = \text{diag}(g_1, g_2)$, one then applies $G \rightarrow UGU^\dagger$ and a subsequent measurement to delete the resulting off-diagonal components in G . The resulting form of G after the sequence of modified Zeno evolution and subsequent measurement takes the form

$$\begin{aligned}
 \begin{pmatrix} g_1 & 0 \\ 0 & g_2 \end{pmatrix} &\rightarrow \begin{pmatrix} g'_1 & 0 \\ 0 & g'_2 \end{pmatrix} \tag{2.31} \\
 g'_1 &= \frac{g_1(2t_{hop}^2(1 + \cos\left(\frac{T}{8}\sqrt{4t_{hop}^2 + (W_{\mathbf{r}} - W_{\mathbf{r}'})^2}\right)) + (W_{\mathbf{r}} - W_{\mathbf{r}'})^2) + g_2(2t_{hop}^2(1 - \cos\left(\frac{T}{8}\sqrt{4t_{hop}^2 + (W_{\mathbf{r}} - W_{\mathbf{r}'})^2}\right)))}{4t_{hop}^2 + (W_{\mathbf{r}} - W_{\mathbf{r}'})^2} \\
 g'_2 &= \frac{g_2(2t_{hop}^2(1 + \cos\left(\frac{T}{8}\sqrt{4t_{hop}^2 + (W_{\mathbf{r}} - W_{\mathbf{r}'})^2}\right)) + (W_{\mathbf{r}} - W_{\mathbf{r}'})^2) + g_1(2t_{hop}^2(1 - \cos\left(\frac{T}{8}\sqrt{4t_{hop}^2 + (W_{\mathbf{r}} - W_{\mathbf{r}'})^2}\right)))}{4t_{hop}^2 + (W_{\mathbf{r}} - W_{\mathbf{r}'})^2}.
 \end{aligned}$$

From these, one can readily extract the elements of the stochastic transfer matrices to take the form

$$R_i = \oplus_{\langle \mathbf{r}, \mathbf{r}' \rangle \in A_i} \begin{pmatrix} 1 - p_{hop, \mathbf{r}\mathbf{r}'} & p_{hop, \mathbf{r}\mathbf{r}'} \\ p_{hop, \mathbf{r}\mathbf{r}'} & 1 - p_{hop, \mathbf{r}\mathbf{r}'} \end{pmatrix} \oplus_{\text{other sites}} I, \quad (2.32)$$

$$p_{hop, \mathbf{r}\mathbf{r}'} = \frac{2t_{hop}^2 (1 - \cos(\frac{T}{8} \sqrt{4t_{hop}^2 + (W_{\mathbf{r}} - W_{\mathbf{r}'})^2})}{4t_{hop}^2 + (W_{\mathbf{r}} - W_{\mathbf{r}'})^2}$$

which is Eq 2.21 in the main text.

Chapter 3

Confinement and Kink Entanglement Asymmetry on a Quantum Ising Chain

3.1 Introduction

Strongly-coupled theories such as QCD can possess rich structure-forming properties relevant to many domains in modern physics. Despite advances in nonperturbative methods like lattice gauge theory and phenomenological modeling, a thorough understanding of QCD remains elusive due to the phenomenon of confinement [86]. Recently, entanglement entropy has been suggested as providing a theoretical tool to investigate QCD systems, both in terms of bound states [87–89] and with respect to scattering processes [90–94].

In parallel, quantum spin chains have been proposed as analogous systems to investigate confinement analytically and numerically [24, 95–100]. In particular, the Ising spin chain has been a useful setup to study confinement in real time [23]. Here, a two-fermion system is represented by domain walls, with binding effects introduced via a longitudinal field that gives an energy penalty linearly proportional to the length of the domain wall [101–103]. This configuration simulates key aspects of the confinement of quark-antiquark pairs into mesons, or the binding of two-nucleon systems into the

deuteron. This simple model, demonstrating confinement in non-equilibrium quantum quench dynamics, has led to an avalanche of related theoretical works [104–119], and the Ising chain confinement was also recently realized on IBM’s quantum hardware [24, 120].

The theory of many-body quantum entanglement can shed insights into confinement and symmetry breaking. Indeed, signatures of confinement show up in entanglement dynamics, where the entanglement entropy is greatly suppressed upon the introduction of the confining field [23, 24, 109]. Symmetry breaking can also manifest in measures of entanglement entropy. When a wave function possesses a local symmetry, its entanglement entropy is a statistical combination of entropies associated to each local occupation number sector [25, 121, 122]. When a local symmetry is broken, however, additional contributions to entropy are generated and can be quantified using “entanglement asymmetry” [12, 123–125]. Various measures of symmetry-resolved entropy have been explored [27, 126–132].

3.2 Model and Entanglement Measures

In this paper, we study the nature of meson dynamics through the lens of entanglement entropy and its asymmetry. In particular, we address the questions: is entropy always suppressed by a confining field? How can one address entanglement asymmetry for a quasi-local conservation law? To do so, we consider the Ising model with transverse and longitudinal fields and an additional three-body term that can be tuned to render the dynamics meson-number conserving for special points in parameter space [133, 134]:

$$H = -J_0 \sum_{i=1}^{L-1} \sigma_i^z \sigma_{i+1}^z - g \sum_{i=2}^{L-1} \sigma_i^x - h \sum_{i=1}^L \sigma_i^z - J \sum_{i=1}^{L-2} \sigma_i^z \sigma_{i+1}^x \sigma_{i+2}^z. \quad (3.1)$$

This model exhibits confinement in the spreading of meson (kink/anti-kink pair) excitations for nonzero longitudinal fields, $h \neq 0$ [24, 111, 135]. When we set $J = -g$, the model is dual to a fermionic chain coupled with a \mathbb{Z}_2 gauge theory [136]; it is kink-number preserving and exhibits quantum many body scars [133, 134, 137]. We further note that the three-body term in the kink preserving regime naturally appears in applications such as the anti-blockade regime of the Rydberg simulators [138], and that quantum many-body scar eigenstates of the kink preserving model have been prepared on IBM superconducting hardware [137].

The Hamiltonian (3.1) can be mapped to a fermionic model using a combination of Kramers-Wannier and Jordan-Wigner transformations (see Sec 3.6):

$$\begin{aligned}
 H = & -2J_0 \sum_{j=2}^L c_j^\dagger c_j - (g-J) \sum_{j=2}^{L-1} (c_j^\dagger c_{j+1} + h.c.) \\
 & - (g+J) \sum_{j=2}^{L-1} (c_j^\dagger c_{j+1}^\dagger + h.c.) - h \sum_{j=1}^L \prod_{i=1}^j (2c_i^\dagger c_i - 1). \quad (3.2)
 \end{aligned}$$

Here c_j^\dagger are fermion creation operators associated with creating a kink between site j and $j-1$ in the original model. Eq. (3.2) shows that indeed kink-number preservation is exact for $J = -g$, allowing us to study regimes away from small g, J . On the other hand, when $g \neq -J$, only the kink-number parity is conserved. Throughout the rest of the paper we set $J_0 = 1, \hbar = 1$, thus time scales throughout this paper are set in the unit of J_0^{-1} .

We consider the time evolution of an initial domain wall product state of length n , i.e., of the form

$$|j, n\rangle \equiv |\dots \uparrow \downarrow_j \dots \downarrow_{j+n-1} \uparrow \dots\rangle. \quad (3.3)$$

Entanglement can be quantified via Rényi entropies,

$$S_n(\rho_A) = \log_2(\text{Tr}(\rho_A^n)) / (1 - n), \quad (3.4)$$

where $\rho_A = \text{Tr}_B \rho$ is a reduced density matrix associated with a subset of sites A when its complement, B , has been integrated out. In particular, the second-order Rényi entropy is $S_2(\rho_A) = -\log_2 \text{Tr}(\rho_A^2)$.

We evaluate $S_2(\rho_A)$ in numerical simulations below. Within time-evolving block decimation (TEBD) [139–141], this generalizes to other entropy orders. Another quantity of interest is the kink density, $\Delta_{i,i+1}^{zz} \equiv \frac{1}{2} \langle (1 - \sigma_i^z \sigma_{i+1}^z) \rangle$, with $\Delta_{i,i+1}^{zz} = 1$ (0) for a spin flip (alignment).

3.3 Kink-preserving Dynamics

As mentioned, with the choice $J = -g$, the Hamiltonian in Eq. (3.1) preserves kink number. To study the evolution of a kink, we project H onto the two-kink subspace in the kink basis, Eq. (3.3):

$$H_2 = \sum_{\substack{0 \leq j < L-1 \\ 0 < n < L-j-1}} 2hn |j, n\rangle \langle j, n| - (g - J) \left(|j-1, n+1\rangle + |j+1, n-1\rangle + |j, n-1\rangle + |j, n+1\rangle \right) \langle j, n|. \quad (3.5)$$

This projection is exact when H conserves kink number. Eq. (3.5) highlights an advantage of adding the three body term in controlling kink production compared to working without the three body interaction $\sigma_i^z \sigma_{i+1}^x \sigma_{i+2}^z$ modification of the transverse field Ising, while assuming g is small. Indeed in the later case, kinks appear perturbatively on the background of a classical Ising chain and propagate slowly, since their kinetics is governed by g . Including the three body term, Eq. (3.5) shows that the dynamics of

the two kink bound states (with $g = -J$) is characterized by the kinetic energy scale $g - J$, which can be tuned to be arbitrarily large, allowing us to study regimes of fast dynamics while preserving kink number.

We note that the exactness of H_2 offers an opportunity to benchmark tensor network methods against the corresponding computation by exact evolution in the two-kink subspace. In particular, we compare the evolution of the local kink density, as well as the 2nd Rényi entropy as computed by exact diagonalization within the two-kink subspace with corresponding computations within TEBD evolution. Interestingly, we are not aware of any previous calculation of Rényi entropy directly in the two-kink subspace Hamiltonian in Eq. (3.5), and we outline the computational approach in Appendix B. We also verify the validity of the two-kink subspace dynamics by comparing the time evolution for various observables and the Rényi entropy with identical quantities computed from small-size exact diagonalization in Appendix 3.A.

3.4 Rényi Entropy saturation, integrability and confinement

In Fig. 1, we consider the evolution of an initially small domain, focusing on the half-chain entropy, $S_2(t)$, and on the kink density. Note the remarkable agreement between the exact diagonalization and TEBD computations, validating the TEBD approach, at least for small kink numbers.

A striking feature of the Rényi entropy dynamics in Fig. 1 (a) is that when $h = 0$ and $g = -J$, the second-order Rényi entropy saturates at $S_2 \leq 2$ when we set our initial state to be a two-kink state. This is surprising at first since a generic two-kink wave function can have a much larger entropy, up to $\log_2(L/2 + 2)$. In Appendix 3.E, we prove that if $h = 0$, and given an initial two-kink state, we have $S_2 \leq 2$ when kink

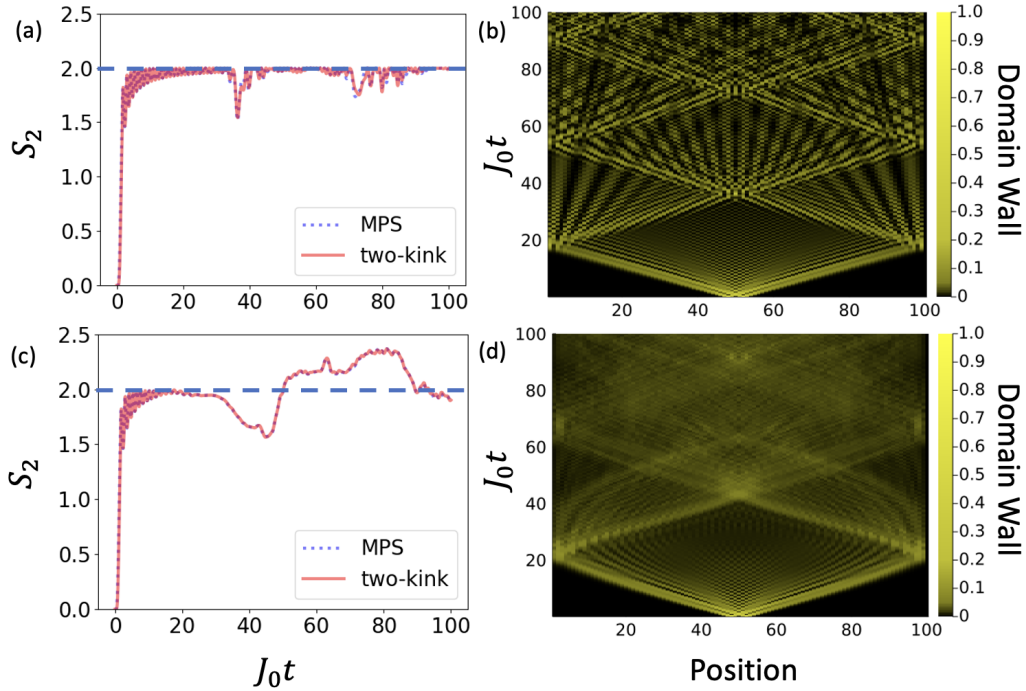


FIGURE 1: Evolution of half chain Rényi entropy for (a) $g = -J = 0.7, h = 0$ and (c) $g = -J = 0.7, h = 0.05$. The corresponding domain wall profile following a quench are (b) $g = -J = 0.7, h = 0$ and (d) $g = -J = 0.7, h = 0.05$ respectively. The initial state $|\uparrow \dots \uparrow \downarrow \downarrow \downarrow \downarrow \uparrow \dots \uparrow\rangle$ is $L = 100$ spin chain with $n = 4$ initial domain size in the middle of the spin chain.

number is conserved.

This bound can be roughly understood as follows. An initial domain wall state (3.3) corresponds, in the fermion formulation (3.2), to two initially localized fermions

$$c_j^\dagger c_{j+n}^\dagger |\text{vac}\rangle. \quad (3.6)$$

When we take $h = 0, J = -g$, the second line in (3.2), vanishes leaving us with a free fermion Hamiltonian. The subsequent evolution is of a pair of non-interacting, uncorrelated, fermions. Intuitively, each fermion can contribute at most $S_2 = \log_2(2) = 1$ due to its de-localization in the system. The uncorrelated nature of the fermions then implies $S_2 \leq 2$. A rigorous proof is given in Appendix 3.E.

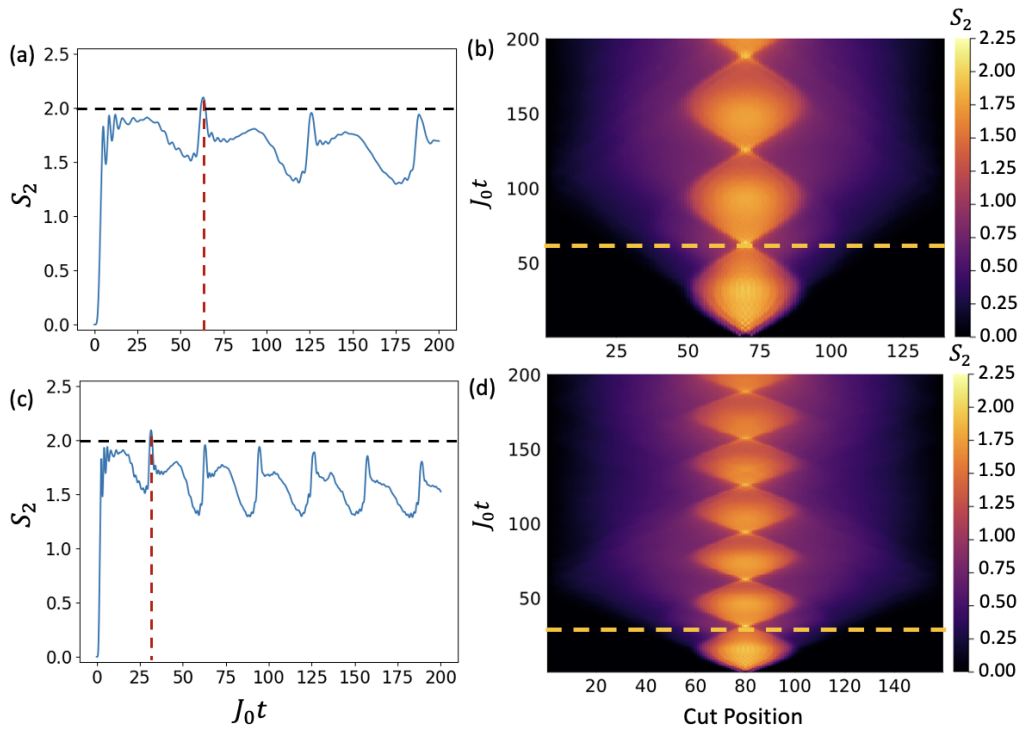


FIGURE 2: Half chain Rényi entropy for (a) $g = -J = 0.25, h = 0.05, L = 140$ and (c) $g = -J = 0.5, h = 0.1, L = 160$. The right figures are bipartite Rényi entropy at all possible cuts along the chain for (b) $g = -J = 0.25, h = 0.05, L = 140$ and (d) $g = -J = 0.5, h = 0.1, L = 160$, for which the left figures are only a slice along the middle of the spin chain. The initial states $|\uparrow \dots \uparrow \downarrow \downarrow \downarrow \downarrow \uparrow \dots \uparrow\rangle$ has $n = 4$ initial domain size in the middle of the spin chain of size of either $L = 140$ or $L = 160$. See Appendix C for accompanying kink density plot.

3.4.1 The effect of confinement and integrability breaking

What happens when $h > 0$? Naively, one may expect that entropy generation will be decreased, due to the reduction of the spread of the particles.

However, considering Fig. 1 (lower), we encounter a surprise: with a small $h = 0.05$, we find a clear violation of the free-particle ($h = 0$) bound. Indeed, the collisions and interactions with $h \neq 0$ do not correspond to non-interacting particles and are not bound by the above argument, as can be seen in the fermionic model (3.2) where the confining term h gives rise to a highly non-local interaction term, thereby allowing quantum correlations and entanglement to develop. We explore this more closely in

Fig. 2. The evolution exhibits the following features: when the string reaches its maximal extent, the entropy starts decreasing, due to a suppression of the wave function spread. However, close to the minimal string size, where collision is possible, entropy shows a rapid increase. When this collision-related increase is sufficient to overcome suppressed entropy, the $S_2 = 2$ bound is violated.

Note that in Fig. 1, the bound violation is enhanced when the size of the chain is smaller than the maximal extent of the wave function spread. In Fig. 2 and the accompanying kink density plot in Appendix 3.C, however, we find that early time collisions can still violate the bound before these boundary effects become substantial, showing that the bound violation may persist also in the thermodynamic limit, $L \rightarrow \infty$. The variations in the Rényi entropy of the system at all cut positions are plotted in the right panels of Fig. 2, showing that the oscillatory behavior of the entropy is reproduced along the internal structure of the meson.

In Fig. 3 we take advantage of the fact that, in exact diagonalization, no Trotterization error is introduced and we can simulate our time evolution dynamics to arbitrarily late times in the exact kink-preserving simulation. Consistent with Fig. 1, when we have $h = 0$, the Rényi entropy is bounded by $S_2 \leq 2$. Upon introducing a small confining field, we see that the Rényi entropy can exceed this upper bound. On the other hand, once the confining field becomes significantly stronger ($h = 0.5$), the Rényi entropy is suppressed compared to the unconfined case, and exhibits oscillatory behavior.

3.5 Entanglement Asymmetry

We now turn to our second question. What is the effect of symmetry breaking on entanglement entropy when the symmetry operator is not exactly local? Given a local symmetry operator of the form $Q = Q_A \otimes I + I \otimes Q_B$ such as charge or magnetization,

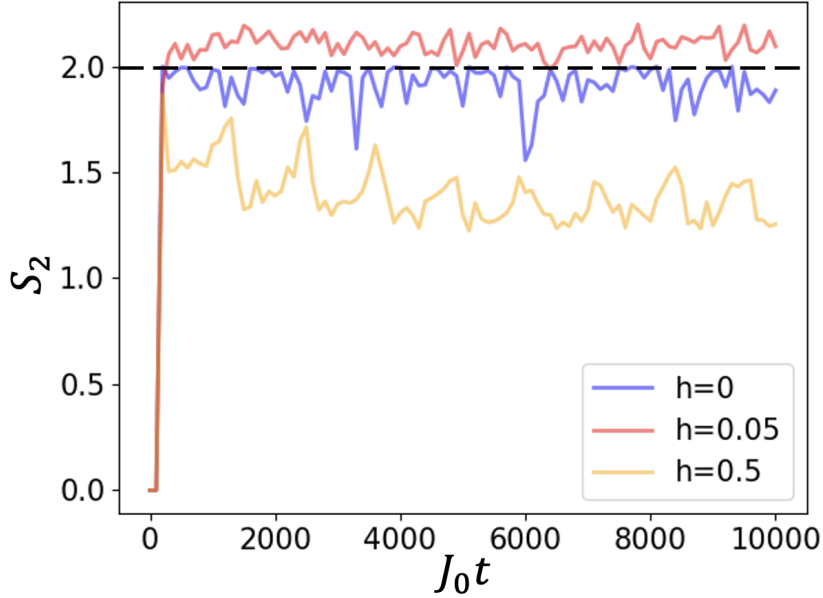


FIGURE 3: The long time dynamics of the bipartite Rényi entropy $S_2(t)$ from the exact diagonalization of the two-kink Hamiltonian H_2 in Eqn 3.5. Here, the kink kinetic energy parameter is set to $g = -J = 0.7$, the chain is of length $L = 100$, and we notice that for weak confining field h , the entropy exceeds the $S_2 = 2$ limit while strong confining field h eventually suppresses the entropy growth.

a useful quantity utilized to study symmetry breaking and its relation to entanglement entropy is the entanglement asymmetry.

The entanglement asymmetry is obtained as follows. First, we project ρ_A onto the blocks associated with different symmetry sectors of Q_A :

$$\rho_{A,Q} = \sum_q \Pi_q \rho_A \Pi_q, \quad (3.7)$$

where Π_q are projectors onto a subspace with a given eigenvalue q of Q_A . When Q_A has integer eigenvalues, the projected density matrix can be written as

$$\rho_{A,Q} = \int_{-\pi}^{\pi} \frac{d\lambda}{2\pi} e^{-i\lambda Q_A} \rho_A e^{i\lambda Q_A}. \quad (3.8)$$

Then, the projected density matrix can be used to construct the entanglement asymmetry [12], given by

$$\Delta S_n(\rho_A) = S_n(\rho_{A,Q}) - S_n(\rho_A), \quad (3.9)$$

where $S_n(\rho_{A,Q}) = \log_2 \text{Tr}(\rho_{A,Q}^n)/(1-n)$ is the symmetry-resolved Rényi entropy. The entanglement asymmetry vanishes, $\Delta S_n = 0$, if computed for a state that commutes with Q . A more detailed introduction to entanglement asymmetry is given in, e.g. [12].

3.5.1 Kink and Kramers-Wannier Entanglement Asymmetries

In contrast to the discussion above and also examples presented in existing literature, we ask the question as to how we can treat entanglement asymmetry when the symmetry operator is not fully local, i.e., the operator associated with the symmetry is not a sum of single site operators.

In our current context, the conservation of kink number is associated with a quasi-local charge (a two-body operator in our case), N_k , since kinks live on the dual lattice, with the number of kinks given by

$$N_k = \sum_{i=1}^{L-1} \Delta_{i,i+1}^{zz} = \frac{1}{2} \left(L - 1 - \sum_{i=1}^{L-1} \langle \sigma_i^z \sigma_{i+1}^z \rangle \right). \quad (3.10)$$

We break the spin chain into complementary subsystems, A and B , where A contains spins $1, \dots, L_A$; then,

$$N_k = N_{k,A} \otimes I + I \otimes N_{k,B} + \Delta_{L_A, L_A+1}^{zz}, \quad (3.11)$$

where $N_{k,A}, N_{k,B}$ count the number of kinks within A and its complement B respectively. The last term measures the presence of a kink at the interface between A and

B.

The presence of a kink at the interface between A and B is impossible to determine from within subsystem A alone. However, we may compute a coarse-grained entanglement asymmetry by projecting onto blocks with fixed kink number inside A . We define the projected density matrix, $\rho_{A,N_{k,A}}$, as

$$\rho_{A,N_{k,A}} = \int_{-\pi}^{\pi} \frac{d\lambda}{2\pi} e^{-i\lambda N_{k,A}} \rho_A e^{i\lambda N_{k,A}} . \quad (3.12)$$

This projection is depicted schematically in Fig. 4; from this, we define an asymmetry, $\Delta S_2^{kink} \equiv \Delta S_2(\rho_{A,N_{k,A}})$, as in Eq. (3.9).

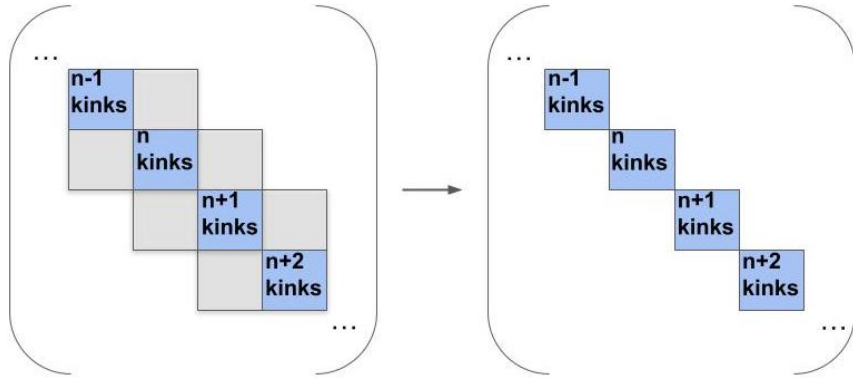


FIGURE 4: Left: The reduced density matrix ρ_A for an initial wave function with a fixed number of kinks may have terms coupling n kinks in the bulk of A with $n + 1$ or $n - 1$ kinks. Right: the projected matrix $\rho_{A,N_{k,A}}$.

We note that asymmetries computed using $\rho_{A,N_{k,A}}$ may be nonzero even if the overall wave function has a fixed kink number. This is in contrast with the entanglement asymmetry ΔS_n associated with strictly local (one-body) symmetry operator, where ΔS_n necessarily vanishes when the wave function has fixed symmetry eigenvalue. In the case of quasi-local (two-body) kink operator, owing to the presence of the kink at the interface, ΔS_n can be nonzero even when the wave function has fixed kink number.

To see this, consider the example of a very simple wave function:

$$\frac{1}{\sqrt{2}}(|\uparrow\uparrow\downarrow\downarrow\rangle + |\uparrow\downarrow\downarrow\downarrow\rangle), \quad (3.13)$$

where the first two spin sites define subsystem A , giving:

$$\rho_A = \frac{1}{2}(|\uparrow\uparrow\rangle + |\uparrow\downarrow\rangle)(\langle\uparrow\uparrow| + \langle\uparrow\downarrow|). \quad (3.14)$$

Note that ρ_A describes a pure state with no entropy, however it is *not* in block form from the point of view of internal kinks in subsystem A . On the other hand

$$\rho_{A, N_k, A} = \frac{1}{2}(|\uparrow\uparrow\rangle\langle\uparrow\uparrow| + |\uparrow\downarrow\rangle\langle\uparrow\downarrow|) \quad (3.15)$$

describes a mixed state with entropy $\log_2 2 = 1$.

Thus our generalized entanglement asymmetry will only vanish for wave functions that have a fixed number of kinks and no kink at the interface between A and B . The presence of kink at the interface, even with fixed kink number, leads to nonzero asymmetry. Nevertheless, the contribution to the asymmetry, ΔS_2^{kink} , from the boundary kink is small: it will be responsible for at most an $O(1)$ contribution to the entropy, and is thus suitable for probing entropy scaling in large systems.

How can we take into account the effect of a possible kink lying at the interface of the bipartition when one calculates quantities such as the entropy? Here, we propose an asymmetry measure that vanishes for eigenstates having total kink number N_k . To do so, we use an open boundary Kramers-Wannier (KW) transformation U_{KW} , which maps $|s_1, \dots, s_N\rangle \rightarrow |t_1, \dots, t_N\rangle$ where $t_1 = s_1$ and $t_i = s_{i-1}s_i$ for $i > 1$. The Kramers-Wannier transformation maps the link variable (in our case, the kink) to a local site variable, i.e., $\sigma_i^z \sigma_{i+1}^z \rightarrow \sigma_{i+1}^z$, and naturally deals with the kink lying in the interface of the bipartition. In particular, U_{KW} maps kink number into magnetization which is

completely local, thus in the Kramers-Wannier (KW) basis, the magnetization entanglement asymmetry should vanish for a wave function with a fixed kink number.

Let us consider the relationship between entropies in the original basis vs the KW basis. We take as the set of sites $A = 1, \dots, L_A$ to be fixed. Given a quantum state on the full system we can define $\rho^{KW} = U_{KW}\rho U_{KW}^\dagger$, and $\rho_A^{KW} = \text{Tr}_B \rho_{KW}$. We show in appendix E that U_{KW} only contains a single two-qubit gate operating between subsystems A, B , and hence $S(\rho_A)$ and $S(\rho_A^{KW})$ differ by at most the entropy that can be generated by such a gate, i.e. at most $2 \log_2 2$. Therefore we can use $S(\rho_A^{KW})$ as an alternative measure for questions of entanglement scaling, i.e., whether entropy is bounded when A is large.

Next, let us discuss the transformation of the kink entanglement asymmetry in the original basis into the magnetization entanglement asymmetry in the Kramers-Wannier basis. Note that under U_{KW} , we have $\prod_{i=1}^{l-1} e^{\pm i\lambda \sigma_i^z \sigma_{i+1}^z} \rightarrow \prod_{i=2}^l e^{\pm i\lambda \sigma_i^z}$ (see Sec 3.6). Thus, following Eqs. (3.8),(3.12), we define the KW projected density matrix as:

$$\rho_{N_k, A}^{KW} = \int_{-\pi}^{\pi} \frac{d\lambda}{2\pi} e^{-i\frac{\lambda}{2} \sum_{l=2}^{L_A} \sigma_l^z} \rho_A^{KW} e^{i\frac{\lambda}{2} \sum_{l=2}^{L_A} \sigma_l^z}, \quad (3.16)$$

and the KW kink asymmetry as $\Delta S_2^{KW} \equiv S_2(\rho_{N_k, A}^{KW}) - S_2(\rho_A^{KW})$. Note that, ΔS_2^{KW} obeys the desired property that $\Delta S_2^{KW} = 0$ if the system is in a state with a fixed number of kinks. Even in cases when kink number is not conserved in the original basis, we in general expect $\Delta S_2^{KW} \leq \Delta S_2^{kink}$, as the kink entanglement asymmetry in the original basis can miscount a kink lying at the interface [see Eq. (3.11)].

3.5.2 MPS implementation

Many 1D systems can be analyzed efficiently using matrix product states (MPS). Previous work has explored entanglement asymmetry in the context of exact diagonalization [12], where large system sizes can only be explored for non-interacting models, and

iTEBD time evolution for interacting models with integrability [142]. Another recent work [143] has explored entanglement asymmetry in matrix product states in the context of the ground state of a symmetric Hamiltonian undergoing spontaneous symmetry breaking. Here we implement the computation of the ΔS_2 entanglement asymmetry given an MPS for generic models that includes non-integrability, an interacting Hamiltonian, and a more general setting that includes non-local entanglement asymmetry.

To proceed beyond the kink conserving dynamics we have developed a Matrix Product State (MPS) procedure to compute S_2 . Given a local charge of interest (magnetization or $N_{k,A}$) we compute the asymmetry by expressing $S_2(\rho_{A,Q})$ as

$$S_2(\rho_{A,Q}) = \int_0^{2\pi} \frac{d\lambda}{\pi} \left(1 - \frac{\lambda}{2\pi}\right) \text{Tr}_A [e^{i\lambda Q_A} \rho_A e^{-i\lambda Q_A} \rho_A]. \quad (3.17)$$

We carry out the trace in Eq. (3.17) by representing ρ as a matrix product operator and doing the necessary contractions.

We will now outline the general algorithm for the straightforward computation of the bipartite entanglement asymmetry for MPS.

1. Perform the time evolution of the MPS from $|\psi(t - \Delta t)\rangle$ to $|\psi(t)\rangle$ with the choice of tMPS, tDMRG or TEBD.
2. Choose the orthogonality center of the MPS across which the bipartite 2nd Rényi entropy $S_2(\rho_A)$ is calculated (mixed canonical MPS).
3. Contract the indices efficiently (with increasing bond dimensions) from one end of the MPS to the orthogonal center to construct the reduced density matrix ρ_A (Fig. 5(a)).
4. With ρ_A , split the numerical integration of Eq. 15 in the main text into $k + 1$ steps. For each discrete λ perform the MPO application onto the ρ_A [Fig. 5(b) or (c)].

Perform the full trace after evaluating $e^{i\lambda Q}\rho_A e^{-i\lambda Q}\rho_A$. The MPO application and tracing is done $k + 1$ times to evaluate $S_2(\rho_{A,Q})$ and subsequently ΔS_2 .

In this work, we calculate two different types of entanglement asymmetry: onsite entanglement asymmetry (such as the magnetization entanglement asymmetry previously considered in [12] with $Q_A = \sum_{i=2}^l \sigma_i^z$) and link-type entanglement asymmetry (in our case, the kink entanglement asymmetry with $Q_A = \sum_{i=1}^{l-1} \sigma_i^z \sigma_{i+1}^z$, shown in Fig. 5(c)).

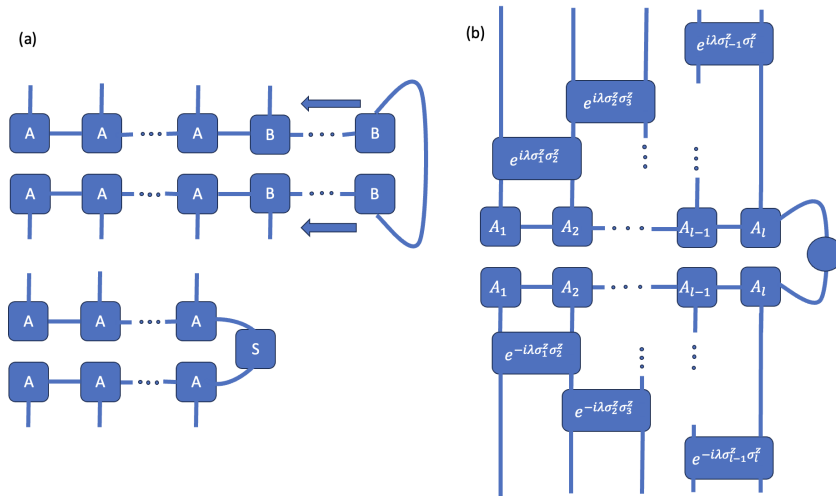


FIGURE 5: (a) The order of contraction of the legs of the tensor of the MPS wave function in the construction of the reduced density matrix $\rho_A = \text{Tr}_B(|\psi_{MPS}\rangle\langle\psi_{MPS}|)$ is shown in the arrow. (b) The MPO operators $e^{\pm i\lambda Q} = \prod_{i=1}^l e^{\pm i\lambda\sigma_i^z}$ (in site-type symmetry resolved entropy), and (c) The MPO operators $e^{\pm i\lambda Q} = \prod_{i=1}^{l-1} e^{\pm i\lambda\sigma_i^z\sigma_{i+1}^z}$ (in link-type symmetry resolved entropy) are applied successively via the DMRG algorithm. If the integral is split into $k + 1$ steps, λ takes discrete values in the interval $[-2\pi, 2\pi]$ and this calculation is done for $(k + 1)$ different λ before the Trapezoid Rule is applied to obtain $\rho_{A,Q}$

A detailed discussion of the computational complexity of the procedure is provided in Appendix 3.D.

3.6 Kramers-Wannier Unitary Transformation and the XY Model

Given the problem that the kink entanglement asymmetry at the interface cannot be tracked in our current basis, we perform a site-to-link transformation to map link variables (such as the domain wall operator $\sigma_i^z \sigma_{i+1}^z$) to site variable. This has traditionally been associated to the Kramers-Wannier duality on a 2D Ising Model. In the context of the (1+1)D Transverse Field Ising Model, one cannot construct a unitary that represents the Kramers-Wannier duality since it maps the ferromagnetic phase of the Transverse Field Ising model ($g < 1$) with ground state degeneracy and spin-flip symmetry breaking to the paramagnetic phase of the Transverse Field Ising Model ($g > 1$) with non-degenerate ground state possessing spin-flip symmetry. Hence, we wish to clarify from the onset that our unitary defined below is a Kramers-Wannier unitary transformation that is only well-defined on an open chain and serves to perform a basis transformation.

We define a Kramers-Wannier unitary U_{KW} that is distinct from the Kramers-Wannier duality in the sense that: (1) it is defined on open boundary condition, (2) it maps all links to sites except the first site, which also maps to the first site in the 'dual' lattice, and (3) the unitary is not self-dual, i.e., $U_{KW}^2 \neq I$. In this way the dimension of the Hilbert space is preserved, since an open chain with N sites only has $N - 1$ links. The unitary is defined and represented in the quantum circuit language as a series of CNOT gates, as shown in Fig. 6.

Here, we have defined $|0\rangle \equiv |\uparrow\rangle \equiv |s = +1\rangle$, $|1\rangle \equiv |\downarrow\rangle \equiv |s = -1\rangle$, and one can verify that the action of the CNOT gate on the target qubit/spin matches the value of the product of spin $t_j = s_{j-1}s_j$. In this dual lattice picture, we can perform the unitary

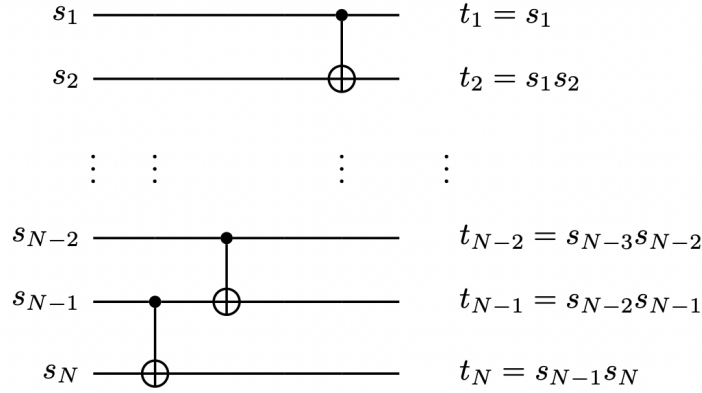


FIGURE 6: This quantum circuit implements the Kramers-Wannier Unitary on an open Ising spin chain.

transformation on the Hamiltonian $H' = U_{KW} H U_{KW}^\dagger$ to get, in this dual picture,

$$H' = - \left[J_0 \sum_{i=2}^L \sigma_i^z + g \sum_{i=2}^{L-1} \sigma_i^x \sigma_{i+1}^x + h \sum_{i=1}^L \left(\prod_{j=1}^i \sigma_j^z \right) - J \sum_{i=2}^{L-1} \sigma_i^y \sigma_{i+1}^y \right], \quad (3.18)$$

where the Kramers-Wannier unitary U_{KW} maps $\sigma_i^z \rightarrow \prod_{j=1}^i \sigma_j^z$, $\sigma_i^x \rightarrow \sigma_i^x \sigma_{i+1}^x$, and the coefficients above identify the origin of the terms of the original Hamiltonian in Eq. 1 in the main text. While the form of the Kramers-Wannier mapping for σ_i^z and σ_i^x has been given in [138], to our knowledge the explicit form of the unitary has not been given in earlier works. In this dual picture, the symmetry operator is transformed as $\prod_{i=1}^{l-1} e^{\pm i \lambda \sigma_i^z \sigma_{i+1}^z} \rightarrow \prod_{i=2}^l e^{\pm i \lambda \sigma_i^z}$, the total magnetization of the left half of the spin chain except the magnetization on site 1.

Interestingly, while the original Hamiltonian had 4 sectors associated with local boundary spins σ_1^z and σ_L^z , our transformed Hamiltonian now commutes with σ_1^z as well as with the parity operator $\prod_{i=1}^L \sigma_i^z$ which is non-local. We also note that the original Hamiltonian preserves the parity of the kink number, even when $g \neq -J$. This form also makes explicit the conservation of kink parity, where kink is now represented by the number of down spins.

When $h=0$ in the Hamiltonian Eq. (3.18), this Hamiltonian is the XY model. This

can readily be cast into the free fermion picture using the Jordan Wigner Transformation, with the resulting Hamiltonian (ignoring constant terms)

$$\begin{aligned}
 H = & - \left[2J_0 \sum_{j=2}^L c_j^\dagger c_j + (g+J) \sum_{j=2}^{L-1} (c_j^\dagger c_{j+1}^\dagger + c_{j+1} c_j) + (g-J) \sum_{j=2}^{L-1} (c_j^\dagger c_{j+1} + c_{j+1}^\dagger c_j) \right. \\
 & \left. + h \sum_{j=1}^L \left(\prod_{i=1}^j (2c_i^\dagger c_i - 1) \right) \right]. \tag{3.19}
 \end{aligned}$$

In this form, the fermions represent the domain walls, and we can read off that the hopping strength of the domain wall is $(g - J)$ while the kink number violation term comes with the strength $(g + J)$.

3.7 Numerical results

We present the numerical results for both the kink-preserving cases and the string breaking cases in Figs. 7 and 8 respectively, in both the original basis and the KW basis, and for Rényi entropy S_2 and Rényi asymmetry ΔS_2 . We begin by commenting on the kink-preserving case $g = -J$ in Fig. 7. Note that the kink Rényi asymmetry ΔS_2^{kink} does not vanish even when the kink number is conserved, consistent with our example illustrated earlier Eq. (3.13). On the other hand, we verify that in the KW basis the asymmetry ΔS_2^{KW} vanishes, as expected¹.

In Fig. 7, we study three different cases with different confining field strength while keeping the kinetic energy $g = -J$ constant: (1) the free fermion case $h = 0$, (2) weak confinement, $h = 0.05$, and (3) strong confinement $h = 0.5$. We note that $S_2(\rho_A^{KW})$ and $S_2(\rho_A)$ are quite close to each other. Moreover, we observe that $S_2(\rho_A^{KW}) > S_2(\rho_A)$ consistently. We can explain this feature as follows. For weakly correlated states, with

¹Due to the approximate nature of the TEBD time evolution on the MPS, we note that there is error of order 10^{-3} on the kink number conservation, and the magnetization asymmetry error is fluctuating in order of 10^{-3} .

low entropy, the wave-function in the vicinity of the cut region is close to a product state in the original basis. As mentioned, the transformation U_{KW} (see Sec 3.6) contains an entangling 2-qubit gate (a CNOT) acting between the sides of the system, which will generically increase the entropy when acting on a weakly correlated state. Thus, we expect that the Rényi entropy S_2 will be enhanced after the Kramers-Wannier transformation compared to the Rényi entropy S_2 in the original basis.

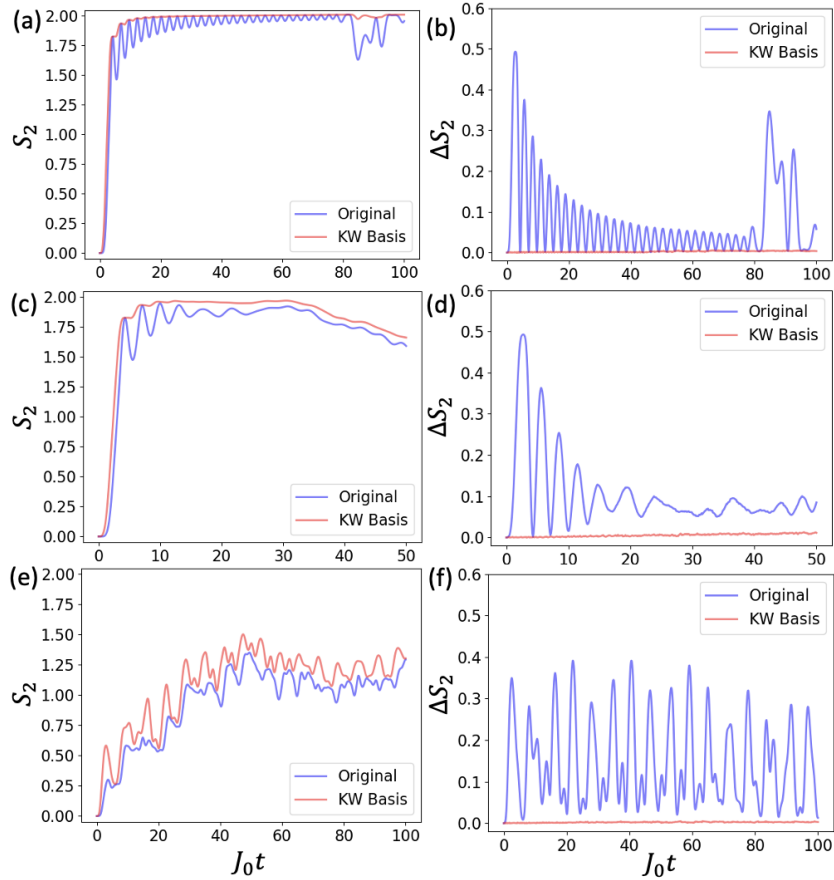


FIGURE 7: Entropy $S_2(t)$ and asymmetry $\Delta S_2(t)$ for the original basis vs Kramers-Wannier basis. Here, (a) $S_2(t)$ for $h = 0$, (b) $\Delta S_2(t)$ for $h = 0$ (c) $S_2(t)$ for $h = 0.05$, (d) $\Delta S_2(t)$ for $h = 0.05$, (e) $S_2(t)$ for $h = 0.5$, and (f) $\Delta S_2(t)$ for $h = 0.5$. Here, the transverse field and three-body strength are set at $g = 0.3 = -J$ for all figures. The initial states $|\uparrow \dots \uparrow \downarrow \downarrow \downarrow \downarrow \uparrow \dots \uparrow\rangle$ for $L = 100$ spin chain has $n = 4$ initial domain size in the middle of the spin chain and the evolution is kink conserving. Note that the shorter time scale of (c) and (d) is due to the higher computational complexity to simulate the Rényi asymmetry for the case $h = 0.05$.

Note the pronounced oscillation of the entropy in the strong confining case. Due

to the strong confinement, the kink is oscillating near the entropy cut, which is reflected in large oscillations of the asymmetry in the original basis, while, consistent with our construction, showing that the KW asymmetry vanishes $\Delta S_2^{KW} = 0$ to a good approximation.

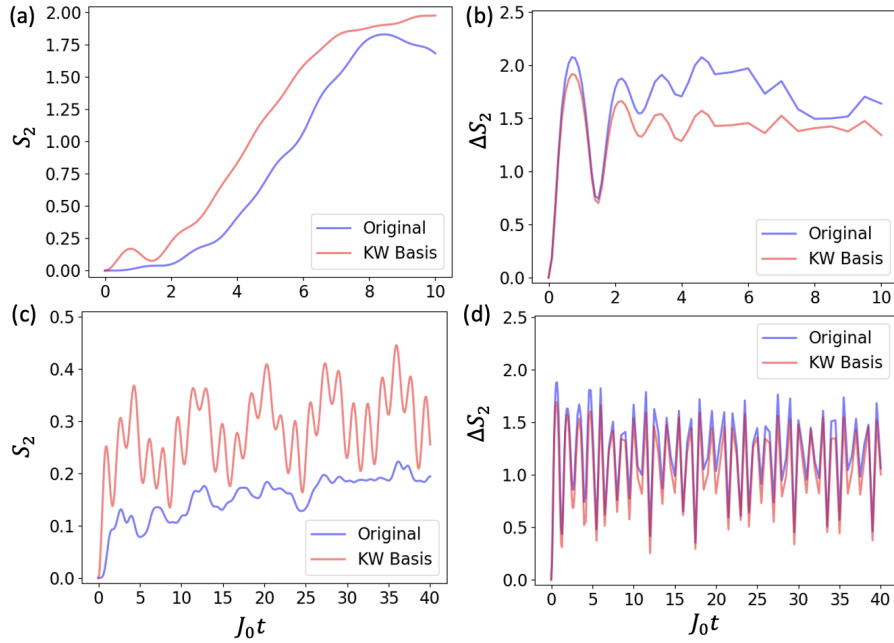


FIGURE 8: Entropy $S_2(t)$ and asymmetry $\Delta S_2(t)$ in the original vs. the Krammers-Wannier basis. Here, (a) $S_2(t)$ for $h = 0$, (b) $\Delta S_2(t)$ for $h = 0$ (c) $S_2(t)$ for $h = 0.4$ and (d) $\Delta S_2(t)$ for $h = 0.4$. Here, the transverse field and three-body strength are set at $g = 0.4$ and $J = 0.1$ respectively for all figures. The initial states $|\uparrow \dots \uparrow \downarrow \downarrow \downarrow \downarrow \uparrow \dots \uparrow\rangle$ for $L = 60$ spin chain has $n = 4$ initial domain size in the middle of the spin chain and the evolution is not kink conserving. Note that the short time scale of the asymmetry evolution owes to the limit of the computational ability to simulate the Rényi asymmetry at later time scales, especially for the $h = 0$ case.

Finally, note that the dip in Rényi entropy in the original basis around $t \approx 85$ for $h = 0$ in Fig. 7 is associated with collision of kinks, and is accompanied with a spike in kink asymmetry in the original basis. In general, we observe that dips in S_2 corresponds to spikes in kink asymmetry ΔS_2^{kink} . A kink density heatmap is provided in Appendix 3.C (see Fig 3.C.2) for reference.

Next we consider kink number violating dynamics in Fig. 8. A common feature shared by the Rényi entropy in the kink-preserving Fig. 7 and string breaking Fig. 8 is that the Rényi entropy in the original basis is in general lower than Rényi entropy in the KW basis.

On the other hand, the kink entanglement asymmetry ΔS_2^{kink} is greater than the KW kink asymmetry ΔS_2^{KW} , though the difference is more pronounced in the kink-preserving case. This behavior may be attributed to the entropy associated with the possibility of a kink at the center of the chain, exactly at the boundary between the left and right regions, as outlined in our discussion in earlier section justifying $\Delta S_2^{KW} \leq \Delta S_2^{kink}$. Comparison with Fig. 7 also shows that, as expected, as soon as kink production is increased, kink-entanglement entropy asymmetry is enhanced. In addition, we see that the KW kink asymmetry ΔS_2^{KW} is in better agreement with ΔS_2^{kink} . This feature can be understood as due to the contribution from possible kinks precisely at the interface playing a less dominant effect.

3.8 Conclusion and Outlook

In summary, we studied entanglement associated with meson dynamics via confined string evolution and effects of string breaking; we quantified these phenomena through a novel application of entanglement asymmetry in a QCD-analogue model system, a transverse-field Ising chain with three-spin interaction and longitudinal field. We performed the Rényi entropy calculation directly in the two-kink subspace. For kink-preserving dynamics, the absence of a longitudinal field gives rise to integrability that sets an upper bound on Rényi entropy. We find that the dynamics of entanglement production generically involves two stages: when the string is contracting, entropy is reduced, followed by an increase when the minimum size is reached. Turning on the confining field can break the integrability bound with weak confining field. However,

the Rényi entropy is suppressed upon further increasing the strength of the confining field. This calculation reveals the internal dynamics of a simulated bound-state system resembling the meson in QCD through the lens of entanglement entropy.

Another significant aspect of our work is the study of the interplay of entanglement and kink production in the context of entanglement asymmetry. To do so, we introduced the kink entanglement asymmetry and the Kramers-Wannier entanglement asymmetry to address the nature of kink number in our spin chain. To study these numerically, we devised a new calculation of Rényi asymmetry using MPS methods and demonstrated its application in the context of kink entanglement asymmetry.

We comment on a few future directions that are worthy of consideration. A few recent papers [126, 127, 132] explored and proposed measuring entanglement asymmetry in quantum hardware simulations, and it will be interesting to simulate new types of entanglement asymmetry on NISQ devices. In addition, there is a need to develop a more computationally efficient approach to obtain Rényi asymmetry (see e.g. [144]). Addressing this question might allow us to access later time dynamics for Rényi asymmetry, and to see if dynamical purification [126] can be observed in settings similar to our setup. Finally, lattice gauge theories with site and link variables provide natural playgrounds to explore the concept of kink entanglement asymmetry proposed in this work.

Appendix

3.A Benchmarking exact diagonalization, two-kink dynamics and tensor network simulations

In this appendix, we present numerical data benchmarking. (1) We study the time evolution dynamics of the spin, initial domain wall, and Rényi entropy for both the exact diagonalization and the two-kink Hamiltonian dynamics, both at the special point $J = -g$ (where they should match) and $J \neq -g$ (where they generally differ). (2) We compare the time evolution dynamics for the initial domain wall and Rényi entropy for tensor network simulation and two-kink dynamics for larger system size.

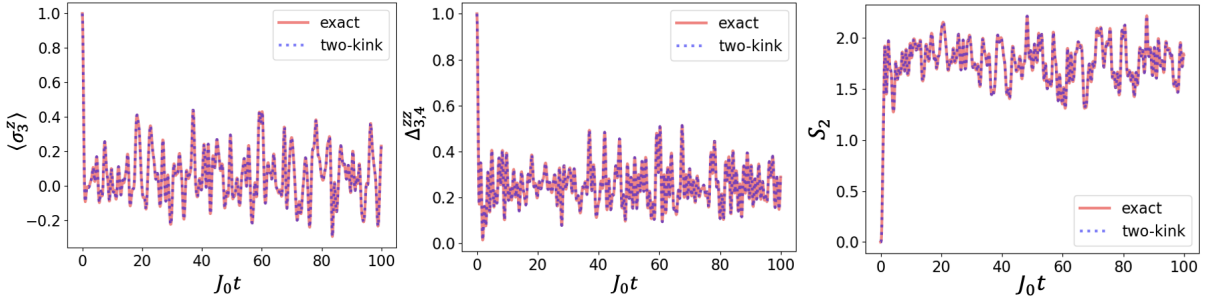


FIGURE 3.A.1: From left to right: The spin expectation value $\langle \sigma_3^z \rangle$, the domain wall expectation value $\Delta_{3,4}^{zz}$ and the half chain Rényi entropy S_2 at parameter values $g = 0.7 = -J, h = 0.1$ for both exact and two-kink dynamics. At this special point where $g = -J$, the time evolution dynamics for the exact diagonalization can be described exactly by two-kink subspace dynamics.

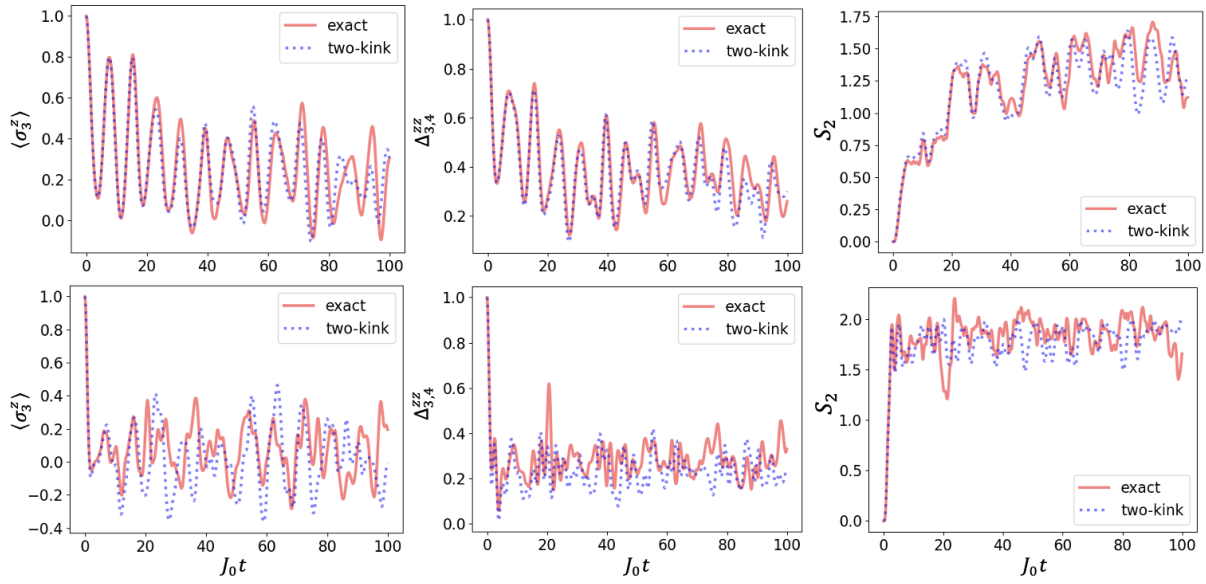


FIGURE 3.A.2: From left to right: The spin expectation value $\langle \sigma_3^z \rangle$, the domain wall expectation value $\Delta_{3,4}^{zz}$ and the half chain Rényi entropy S_2 . From top to bottom: The set of physical quantities at the top panel was simulated at $g = 0.3, h = 0.4$ and $J = -0.05$ while the bottom panel was at $g = 0.6, h = 0.1, J = -0.1$. Note that the top panel corresponds to a more confined dynamics, where the deviation of the time evolution and exact diagonalization occurs only at late time, while for parameter with less confinement (smaller h), the deviation is significant even at early times.

For the first benchmarking between exact diagonalization and two-kink dynamics (to establish the reliability of two-kink dynamics in kink-conserving cases), we initialize the quantum state of a $L = 10$ quantum Ising spin chain to $|\psi_0\rangle = |\uparrow\uparrow\uparrow\uparrow\downarrow\uparrow\uparrow\uparrow\uparrow\rangle$, and time evolve the state using (a) exact diagonalization of the Hamiltonian Eq. 1 in the main text and (b) two-kink Hamiltonian Eq. 4 in the main text. For Fig. 3.A.1 and 3.A.2, the spin expectation values $\langle \sigma_i^z(t) \rangle$ are tracked at the underlined spin $|\uparrow\uparrow\uparrow\uparrow\downarrow\uparrow\uparrow\uparrow\uparrow\rangle$ in the initial state $|\psi_0\rangle$, and the domain wall expectation values $\Delta_{i,i+1}^{zz}(t)$ are tracked at $|\uparrow\uparrow\uparrow\uparrow\downarrow\downarrow\downarrow\uparrow\uparrow\uparrow\uparrow\rangle$, and the Rényi entropy is cut at half chain bipartition respectively.

In Fig. 3.A.1, we see that the time evolution of the various different physical quantities of interest match between exact diagonalization and two-kink subspace evolution. As demanded by the symmetry of the Hamiltonian when $g = -J$, the domain wall

number at this special line is exactly conserved.

We then turn to the string breaking (more generic) cases, where kink number is not conserved. In Fig. 3.A.2, we observe that while we generally expect the dynamics of the exact Hamiltonian to differ from that from the two-kink subspace projection at $g \neq -J$, the macroscopic expectation values for spin $\langle \sigma_i^z \rangle$ and domain wall $\Delta_{i,i+1}^z$ overlaps significantly for early times and only deviate at later time for strong confining field h . In contrast, with weak confining field h the dynamics deviates significantly at early times. This establishes the general physics and intuition that with strong confinement h , two-kink approximation is reasonable for quantum quench problem with initial state $|\uparrow \dots \uparrow \downarrow \dots \downarrow \uparrow \dots \uparrow\rangle$.

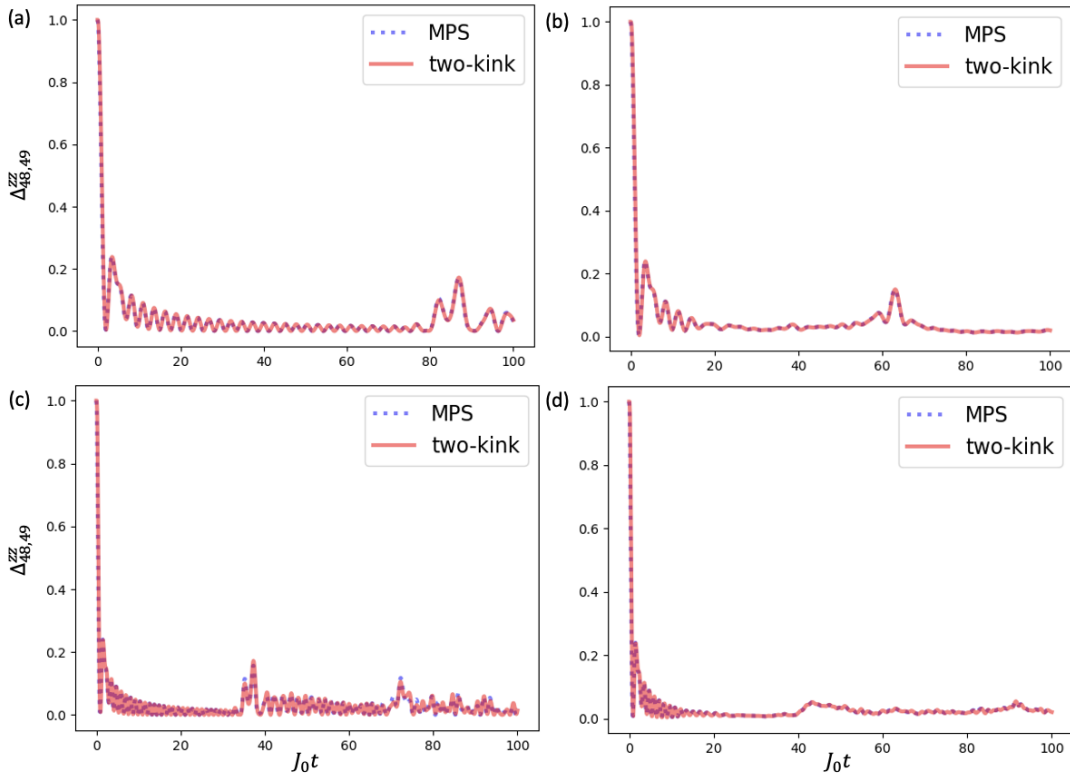


FIGURE 3.A.3: The set of parameter values used for the time evolution of the domain wall $\Delta_{48,49}^{zz}$ at position 48 and 49 following a quantum quench are (a) $g = 0.3, J = -0.3, h = 0$, (b) $g = 0.3, J = -0.3, h = 0.05$, (c) $g = 0.7, J = -0.7, h = 0.0$, (d) $g = 0.7, J = -0.7, h = 0.05$.

After verifying the validity of the two-kink dynamics for kink-conserving dynamics, we then turn to the benchmarking of the tensor network simulations with the two-kink dynamics. In the main article, we provided the benchmarking of MPS with two-kink dynamics for the time evolution of the Rényi entropy S_2 for $g = -J = 0.7$ in Fig. 1 in the main text. Here, we provide additional numerical simulations of the domain wall profile located at the initial domain wall positions at 48th and 49th sites for a spin chain of length $L = 100$ and initial state with 4 middle flipped spin $|\uparrow_1 \dots \uparrow_{48} \downarrow_{49} \downarrow_{50} \downarrow_{51} \downarrow_{52} \uparrow_{53} \dots \uparrow_{100}\rangle$, as shown in Fig. 3.A.3. This provides an additional check (besides the Rényi entropy dynamics) that the MPS time evolution from TEBD is approximated well by two-kink time evolution.

3.B Construction of the reduced density matrix in the Two-Kink Subspace

In this section, we outline the overall approach we used to construct the reduced density matrix in the two-kink subspace in order to calculate the 2nd order Rényi entropy for dynamics within the two-kink subspace. We represent all possible two-kink states in a spin chain of length L , $|\uparrow_1 \dots \uparrow_{j_L-1} \downarrow_{j_L} \dots \downarrow_{j_R} \uparrow_{j_R+1} \dots \uparrow_L\rangle$, with the two number representation $|j_L, j_R\rangle$, where j_L is the position of the left domain wall and j_R is the position of the right domain wall. In the two-kink Hilbert space, for sites $i = 1, \dots, L$, the two numbers can take the following values $1 < j_L \leq j_R < L$.

With this two-number representation, a quantum spin chain of size L will have a two-kink subspace of dimension $(L-1)(L-2)/2$. To proceed with the Rényi entropy calculation, given a bipartition bond l_B separating the spin chain into left-right bipartition with sites $1, \dots, l_B$ to the left side of the chain and sites $l_B + 1, \dots, L$ to the right,

we will proceed to perform bipartition in the two-kink states

$$\begin{aligned}
|\psi\rangle &= \sum_{1 < j_L \leq j_R \leq l_B < L} \alpha_{j_L, j_R} |\text{one/two-kink}\rangle_L |\text{no-kink}\rangle_R \\
&+ \sum_{1 < j_L \leq l_B < j_R < L} \alpha_{j_L, j_R} |\text{one-kink}\rangle_L |\text{one-kink}\rangle_R \\
&+ \sum_{1 \leq l_B < j_L \leq j_R < L} \alpha_{j_L, j_R} |\text{no-kink}\rangle_L |\text{one/two-kink}\rangle_R,
\end{aligned} \tag{3.20}$$

where we decompose the sum into three types of terms classified by the location of the bipartition cut relative to the domain wall positions. Here, the states with label $|\text{one-kink}\rangle_L |\text{no-kink}\rangle_R$ and $|\text{no-kink}\rangle_L |\text{one-kink}\rangle_R$ are cases where the bipartition cut l_B coincides with one of the left/right domain walls.

Constructing the full pure state density matrix $|\psi\rangle\langle\psi|$ and taking the partial trace over the right partition, we have

$$\begin{aligned}
\rho_L &= \text{Tr}_R(|\psi\rangle\langle\psi|) = \sum_{1 < j_L \leq j_R \leq l_B} \sum_{1 < j'_L \leq j'_R \leq l_B} \alpha_{j_L, j_R} \alpha_{j'_L, j'_R}^* |\text{one/two-kink}\rangle\langle\text{one/two-kink}| \\
&+ \sum_{1 < j_L \leq l_B} \sum_{1 < j'_L \leq l_B} \left(\sum_{l_B < j_R < L} \alpha_{j_L, j_R} \alpha_{j'_L, j'_R}^* \right) |\text{one-kink}\rangle\langle\text{one-kink}| \\
&+ \left(\sum_{l_B < j_L \leq j_R < L} \alpha_{j_L, j_R} \alpha_{j'_L, j'_R}^* \right) |\text{no-kink}\rangle\langle\text{no-kink}| \\
&+ \sum_{1 < j_L \leq l_B} \left(\sum_{l_B < j_R < L} \alpha_{j_L, j_R} \alpha_{j'_L = l_B + 1, j'_R}^* \right) |\text{one-kink}\rangle\langle\text{no-kink}| \\
&+ \sum_{1 < j'_L \leq l_B} \left(\sum_{l_B < j_R < L} \alpha_{j'_L, j'_R}^* \alpha_{j_L = l_B + 1, j_R} \right) |\text{no-kink}\rangle\langle\text{one-kink}|
\end{aligned} \tag{3.21}$$

We shall elaborate on each term below.

The first term

The first term in Eq. (3.21) is obtained from the multiplying the first terms of Eq. (3.20) in both $|\psi\rangle$ and $\langle\psi|$, followed by partial right trace over all spin-up state $|\text{no-kink}\rangle_R$. Hence, the coefficients in the first term in Eq. (3.21) can be understood to be constructed without performing any sum from partial tracing.

The second term

The second term in Eq. (3.21) is obtained by multiplying the second terms of Eq. (3.20) in both $|\psi\rangle$ and $\langle\psi|$, followed by partial right trace over $|\text{one-kink}\rangle_R$. In this case, the coefficients in the second term in Eq. (3.21) is constructed from summing over $l_B < j_R = j'_R < L$ where the right partition states $|\text{one-kink}\rangle$ and $\langle\text{one-kink}|$ must agree in the partial trace process.

We also note here that terms labelled as 'the second term' is actually a subset of 'the first term' and not a new set of distinct terms (which we label separately only because they had different origin), so the coefficients here should add to the coefficients of the first term when the states are the same.

The third term

The third term in Eq. (3.21) is actually a single state, and its coefficient is constructed from a sum over the modulo square $|\alpha_{j_L, j_R}|^2$ for $l_B < j_L \leq j_R < L$. Here j_L and j_R both lie on the right partition basis states, for which the indices must match (hence mod square) when one performs the partial trace.

The fourth and fifth terms

The fourth and the fifth term in Eq. (3.21) are the complex conjugate of each other, so it suffices to explain one of them. The fourth term comes from the cross multiplication of the second term $|\text{one-kink}\rangle|\text{one-kink}\rangle$ and the third term of type $\langle\text{no-kink}|\langle\text{one-kink}|$ in Eq. (3.20).

Note that the third term of the form $\langle\text{no-kink}|\langle\text{two-kink}|$ cannot contribute since the right partition partial cannot match those from $|\text{one-kink}\rangle|\text{one-kink}\rangle$. This explains the setting of $j'_L = l_B + 1$ in the coefficient of the fourth term (likewise the corresponding term in the fifth term). We also understand that there is a single sum matching the indices $j_R = j'_R$ over the range $l_B < j_R < L$ when one constructs the coefficients of the fourth and the fifth term.

Matrix representation of the reduced density matrix

Collecting these terms, it helps to visualize these various terms on a matrix representation. We label row sectors according to $|\text{two-kink}\rangle$, $|\text{one-kink}\rangle$ and $|\text{no-kink}\rangle$ and likewise for the column sectors. The matrix representation is as below.

$$\rho_L = \left(\begin{array}{c|c|c} \text{First term} & \text{First term} & 0 \\ \hline |\text{two-kink}\rangle\langle\text{two-kink}| & |\text{two-kink}\rangle\langle\text{one-kink}| & \\ \hline \text{First term} & \text{First + Second term} & \text{Fourth term} \\ |\text{one-kink}\rangle\langle\text{two-kink}| & |\text{one-kink}\rangle\langle\text{one-kink}| & |\text{one-kink}\rangle\langle\text{no-kink}| \\ \hline 0 & \text{Fifth term} & \text{Third term} \\ & |\text{no-kink}\rangle\langle\text{one-kink}| & |\text{no-kink}\rangle\langle\text{no-kink}| \end{array} \right)$$

Here, the third row is a single row and the third column is a single column. The reduced density matrix can then be used to calculate the Rényi entropy for the two-kink

dynamics.

3.C Rényi Entropy Evolution and Collisions: Early time and Entropy bound violation with large system size

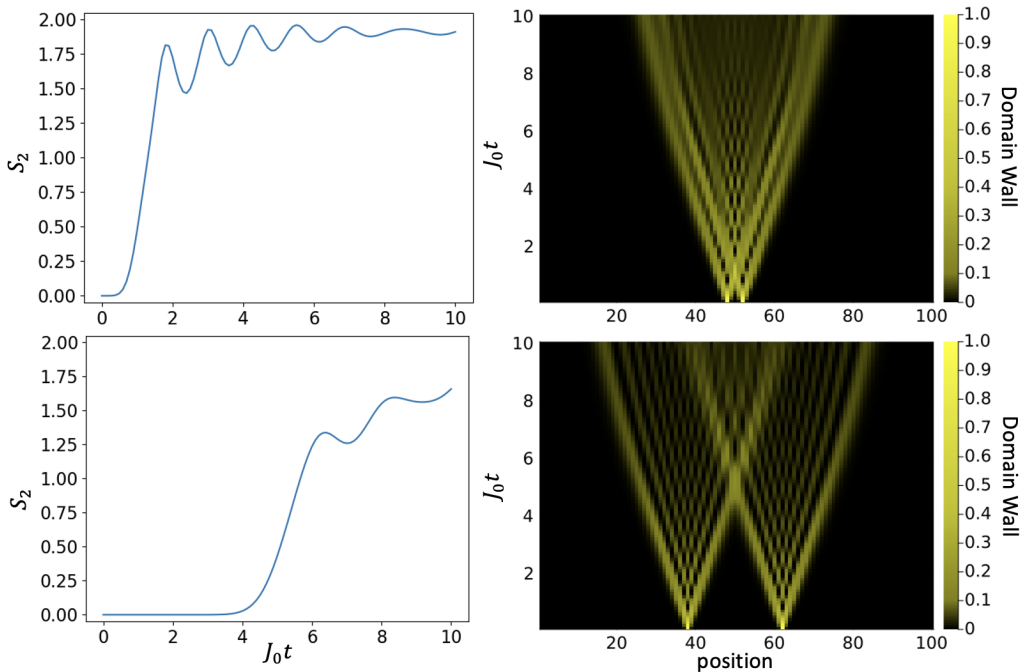


FIGURE 3.C.1: The half-chain Rényi entropy S_2 (left) and the domain wall profile across link positions (right) for the parameter value set $g = -J = 0.7, h = 0.1$. Here the top diagrams are results from initial state with domain wall separation $l = 4$ (4 down spins in the middle) while the bottom diagrams are results with initial domain wall separation $l = 24$. The increase in S_2 in the early time roughly coincides with the time scale of collision for kink-conserving dynamics. The spin chain is of length $L = 100$.

In this appendix, we cover two points. (1) We outline several qualitative features of the Rényi entropy evolution that highlight several interesting features that are not discussed in the main article. (2) In addition, we show that the entropy bound violation with confining field is independent of the finite system size effect. We will mainly concern ourselves with the kink-preserving dynamics in this appendix.

For generic model parameters, as the initial product state domain wall starts evolving, entanglement immediately appears, dominated by the dynamics of kink-anti kink pair creation and motion. In contrast, for kink-number preserving dynamics, the half-chain entanglement can only begin emerging when the kinks collide. To see this, we compute the Rényi entropy of half of the chain. In Fig. 3.C.1, we show how a rapid increase in the half-chain Rényi entropy S_2 for small domain wall and large domain wall separation is associated to the time of the domain wall spreading and collision. Here, a small initial domain wall separation ($l = 4$) has a collision around $t \approx 1$ while that of the large separation $l = 24$ has collision around $t \approx 5$.

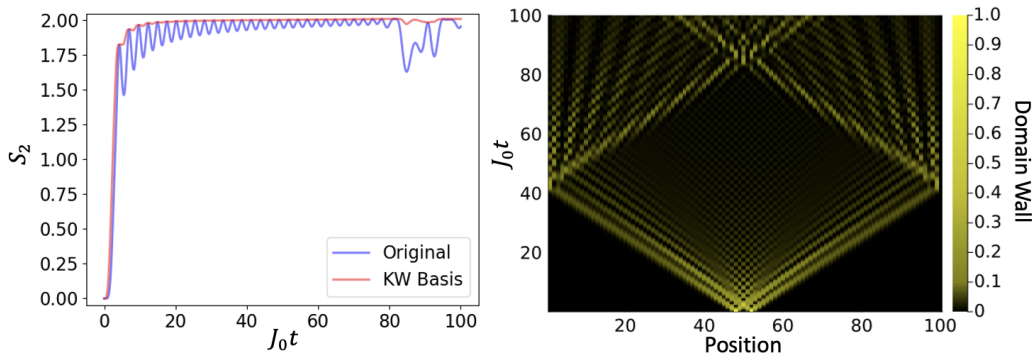


FIGURE 3.C.2: The half-chain Rényi entropy S_2 (left) and domain wall heat (right) for $g = -J = 0.3, h = 0, L = 100$, and initial domain wall separation size $l = 4$. The dip around $t \approx 85$ corresponds to kink collisions. The color scale has been magnified near $\Delta_{i,i+1}^{zz} = 0$ as the kink density becomes diluted upon spreading.

We provide additional details for the Rényi entropy dips found in Fig. 5 in the main text. Here, the dip around $t \approx 85$ is directly associated with kink collision after bouncing off the open boundary chain. We provide the associated domain wall/kink heatmap in Fig. 3.C.2.

We now turn to demonstrate that the violation of the $S_2 = 2$ bound is independent of the system size, along with other qualitative features of the entropy evolution. In Fig. 3.C.3, we vary various parameters within the kink-conserving dynamics: (1) the kinetic energy ($g - J$), (2) the confining potential field h , and (3) the system size L .

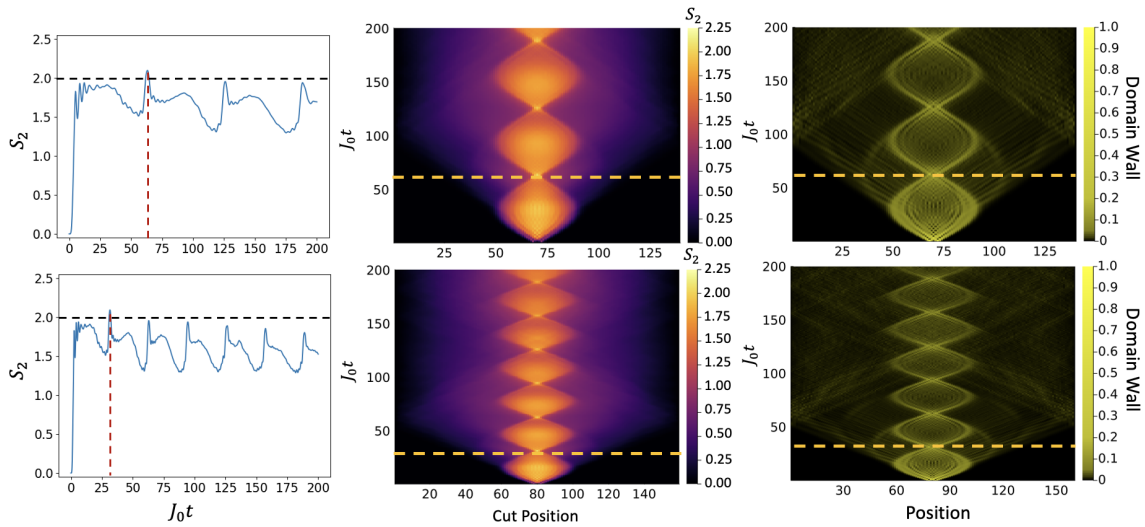


FIGURE 3.C.3: The half-chain Rényi entropy S_2 (left), the Rényi entropy map with different bipartite cut position (middle), and the domain wall profile across link positions (right) for $g = -J = 0.25, h = 0.05, L = 140$ (top) and $g = -J = 0.5, h = 0.1, L = 160$ (bottom).

In Fig. 3.C.3, we see the S_2 entropy bound is violated upon the second collision of the kinks. The first collision happens at early time and is discussed in detail earlier in this appendix. Here, we verify that the total kink density near the ends of the chain is negligible when the second collision occurs upon the acceleration of the kink dynamics back to the middle of the chain owing to the confining potential.

Another feature of the kink-conserving dynamics is the dip in the Rényi entropy before the periodic collisions of the kinks after expanding to maximal extent set by the strength of the confining potential. This can be observed in the half-chain Rényi entropy, as well as in the Rényi entropy heatmap diagram, where the color code shows a lower Rényi entropy dip right before the periodic collisions of the kinks.

3.D Computational Complexity of the MPS Implementation

We will comment on the computational complexity of our algorithm above, and possible speed up that could possibly be implemented in a future work. In iTensor, working with density matrices is actually sub-optimal since it creates MPO with bond dimension D^2 , which we illustrate in Fig. 3.D.1. Depending on the details of how iTensor package handles the contraction of two (different) reduced density matrices, this computation can either scale as $\mathcal{O}(Ld^3D^8)$ in the worst case or $\mathcal{O}(Ld^3D^6)$ in the most optimal case. Dealing with reduced density matrices directly is more straightforward in code development with existing methods in iTensor, but severely limits the simulability of Rényi entropy evolution to later times when bond dimension is large everywhere on the spin chain. This is the case for string breaking (kink number violating, generic case) situation when $g \neq -J$, as shown in Fig. 6 in the main text when we attempt to calculate Rényi asymmetry directly with density matrix contractions and issue with computational cost only allows time evolution for early times ($t = 10$).

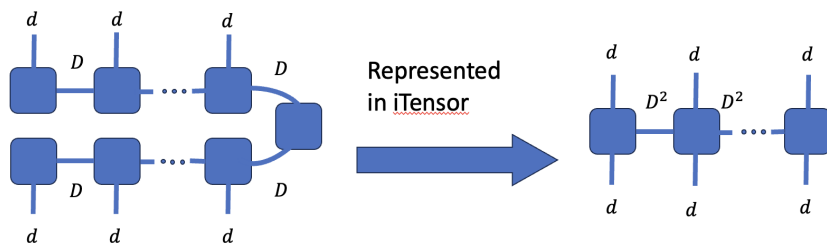


FIGURE 3.D.1: In iTensor, taking an outer product of an MPS $|\psi\rangle$ with itself (with bond dimension D) automatically forms an MPO density matrix with bond dimensions D^2 .

Instead, an optimal approach is shown in Fig. 3.D.2. The algorithm represented pictorially in Fig. 3.D.2 will necessitate contractions without constructing reduced density matrices directly. In this approach, we contract tensors individually and avoid the dealing with the full D^2 bond dimensions of each ρ_A MPO link. The algorithm in this

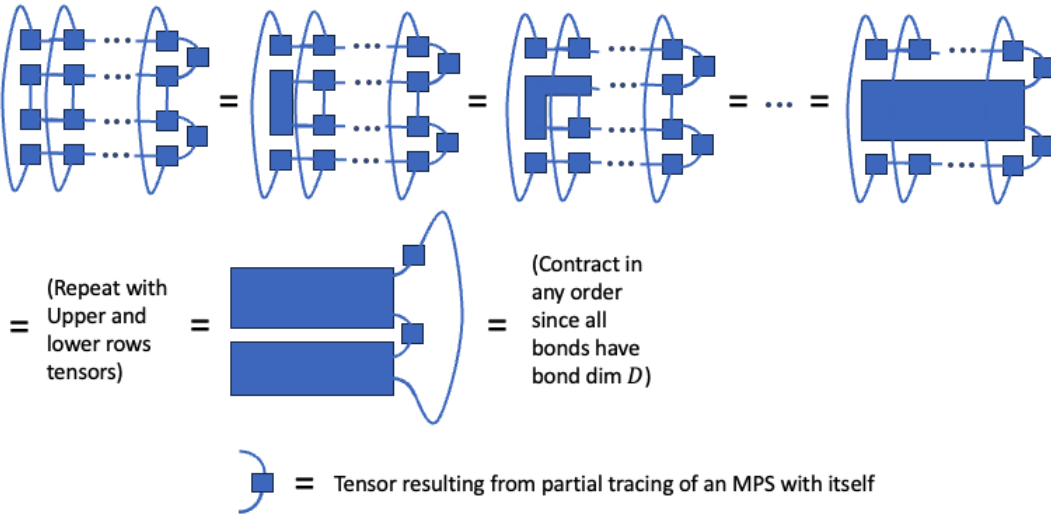


FIGURE 3.D.2: Minimal contraction order for individual tensors to compute $\text{Tr}(e^{i\lambda Q} \rho_A e^{-i\lambda Q} \rho_A)$. Here the top 2 and bottom 2 rows of tensors can come from different reduced density matrix. The strategy for implementation here is to perform contractions of individual tensor component in MPS wave functions without first forming the density matrix MPOs, and the size tensor from partial trace can also be formed partial inner product of MPS wave function with itself.

case will dramatically improves the complexity to $\mathcal{O}(LdD^3)$, but it comes with a more complicated code development. We will leave the development of a more efficient entanglement asymmetry computation as a future research avenue.

3.E Upper bound on Rényi Entropy for $h = 0$ and kink-number preservation.

In this appendix, we prove that starting with a domain wall, and evolving with our Hamiltonian with $J = -g$ and $h = 0$ the second order half chain Rényi entropy $S_2 = -\log_2(\text{Tr}(\rho_A^2))$ is bound by 2 at all times. Concretely, we consider an initial state of the form:

$$|\psi(0)\rangle = |\uparrow \dots \uparrow \downarrow_x \dots \downarrow_{y-1} \uparrow_y \dots \uparrow\rangle \tag{3.22}$$

To compute the evolution, we first apply the Kramers-Wannier U_{KW} , mapping the state to:

$$U_{KW}|\psi(0)\rangle = |1\dots(-1)_x111(-1)_y11\dots1\rangle. \quad (3.23)$$

Via a Jordan Wigner transformation this state will become the two particle state

$$U_{KW}|\psi(0)\rangle = c_x^\dagger c_y^\dagger |\text{vac}\rangle. \quad (3.24)$$

As explained above, the evolution of the state in the Jordan-Wigner picture is governed by the quadratic fermion Hamiltonian (3.6). In particular, when $g = -J$, the Hamiltonian does not involve pair creation terms. Under such evolution, the creation operators in (3.24) transform as:

$$c_\alpha^\dagger \longrightarrow \sum_j u_{\alpha j} c_j^\dagger \quad (3.25)$$

with a unitary $L \times L$ matrix u . Therefore the evolved state is of the form:

$$U_{KW}|\psi(t)\rangle = \sum_{i,j} u_{xi} u_{yj} c_i^\dagger c_j^\dagger |\text{vac}\rangle = \sum_{i<j} (u_{xi} u_{yj} - u_{xj} u_{yi}) c_i^\dagger c_j^\dagger |\text{vac}\rangle \quad (3.26)$$

We now undo the Kramers-Wannier transformation to get:

$$|\psi(t)\rangle = \sum_{i<j} (u_{xi} u_{yj} - u_{xj} u_{yi}) |\uparrow \dots \uparrow \downarrow_i \dots \downarrow_{j-1} \uparrow_j \dots \uparrow\rangle \quad (3.27)$$

We now proceed by bounding the Schmidt rank of the state (3.27). We expand the summation explicitly as:

$$\begin{aligned}
 |\psi(t)\rangle &= \sum_{i \leq L_A} \sum_{j > L_A} (u_{xi}u_{yj} - u_{xj}u_{yi}) |\uparrow \dots \uparrow \downarrow_i \dots \downarrow_{j-1} \uparrow_j \dots \uparrow_N\rangle \\
 &+ \sum_{i > L_A} \sum_{j > i} (u_{xi}u_{yj} - u_{xj}u_{yi}) |\uparrow \dots \uparrow \downarrow_i \dots \downarrow_{j-1} \uparrow_j \dots \uparrow_N\rangle \\
 &+ \sum_{i < j} \sum_{j \leq L_A} (u_{xi}u_{yj} - u_{xj}u_{yi}) |\uparrow \dots \uparrow \downarrow_i \dots \downarrow_{j-1} \uparrow_j \dots \uparrow_N\rangle \\
 &= (\sum_{i \leq L_A} u_{xi} |\uparrow \dots \uparrow \downarrow_i \dots \downarrow_{L_A}\rangle) \otimes (\sum_{j > L_A} u_{yj} |\downarrow_{L_A+1} \dots \downarrow_{j-1} \uparrow_j \dots \uparrow_N\rangle) \\
 &- (\sum_{i \leq L_A} u_{xj} |\uparrow \dots \uparrow \downarrow_i \dots \downarrow_{L_A}\rangle) \otimes (\sum_{j > L_A} u_{yi} |\downarrow_{L_A+1} \dots \downarrow_{j-1} \uparrow_j \dots \uparrow_N\rangle) \\
 &+ |\uparrow \dots \uparrow \uparrow_{L_A}\rangle \otimes (\sum_{i > L_A} \sum_{j > i} (u_{xi}u_{yj} - u_{xj}u_{yi}) |\uparrow \dots \uparrow \downarrow_i \dots \downarrow_{j-1} \uparrow_j \dots \uparrow_N\rangle) \\
 &+ (\sum_{i < j} \sum_{j \leq L_A} (u_{xi}u_{yj} - u_{xj}u_{yi}) |\uparrow \dots \uparrow \downarrow_i \dots \downarrow_{j-1} \uparrow_j \dots \uparrow_{L_A}\rangle) \otimes |\uparrow \dots \uparrow \uparrow_N\rangle. \tag{3.28}
 \end{aligned}$$

Observe that in the last line we have explicitly separated $|\psi(t)\rangle$ into a combination of the form:

$$|\psi(t)\rangle = \sum_{\alpha=1}^4 |\phi_\alpha\rangle \otimes |\tilde{\phi}_\alpha\rangle. \tag{3.29}$$

Note that for the rest of the argument, it doesn't matter if $\phi_\alpha, \tilde{\phi}_\alpha$ are normalized or represent orthogonal sets. Indeed, the form (3.29) immediately implies that the Schmidt rank of the state $|\psi(t)\rangle$ with respect to this partition is at most $\text{Sch}(\psi(t)) \leq 4$ (see Problem 2.2 in [26]). Since the logarithm of the Schmidt number is a bound on entropy (Von Neumann entropy, and as consequence also Rényi entropy) we have that:

$$S_2 \leq \log_2 \text{Sch}(\psi(t)) \leq \log_2 4 = 2. \tag{3.30}$$

Chapter 4

Conclusion

Recent theoretical and experimental progress has allowed for unprecedented ability to simulate the dynamics of quantum many-body systems out of thermal equilibrium in recent years. Many theoretical formalisms and numerical methods have been developed to tackle the difficult problem of simulating non-equilibrium quantum dynamics in both open and closed quantum systems. In this thesis, we have introduced and analyzed both open and closed systems where the surprising behavior of non-equilibrium dynamics is showcased.

Specifically, in Chapter 2, the closed hierarchy formalism has been applied to the problem of non-interacting fermions under repeated measurements with diffusive transport and various experimentally realistic disorders. The first part of the chapter is devoted to understanding both analytically and numerically the diffusion constant associated to the diffusion transport in the measurement-induced chiral current. The second part then turned to understanding analytical and numerically the influence of disorder on the flow rate of the measurement-induced chiral current. The flow rate of the chiral current induced by repeated measurements is generally reduced by the introduction of various types of disorder. In the case where both Zeno measurement limit (where time intervals between measurements get infinitesimally small) and deterministic walk (achieved by tuning the time interval of each of the 8 measurement steps in

the cycle to be of certain values), the site dilution disorder case displays a geometric percolation threshold. Analytical treatment is amendable to cases strictly in the Zeno measurement limit only, and most of the investigation is numerically in nature.

Attention is then turned to the quenched dynamics of closed quantum system in Chapter 3. Specifically, the goal is to understand and investigate confinement by mapping confinement into the quenched dynamics of domain walls in quantum Ising model in one dimension. By tuning the model, the majority of Chapter 3 is focused on understanding domain wall dynamics where domain wall number is conserved. The model of interest displays integrability in the kink-preserving Ising model when no longitudinal field exists and this integrability sets a bound of the entanglement entropy of the quantum state. This bound is then broken when one introduces confinement into the problem. The second part of Chapter 3 then turned to investigate a new type of entanglement asymmetry that is two-body in nature, and reveal surprising properties about the entanglement asymmetry. Along the way, we developed a tensor network algorithm to compute entanglement asymmetry in the most generic setting, and also uncover a unitary quantum circuit that realizes the the Kramers-Wannier transformation for a one-dimensional problem with open boundary condition.

Overall, this dissertation has made theoretical advances on the simulation of quantum dynamics in quantum many-body systems outside of equilibrium. New methods have been proposed and utilized to tackle the problems of (1) open, non-interacting quantum system under measurements, and (2) closed, interacting quantum system. The study of entanglement dynamics in Chapter 3 is especially of interest to various quantum simulation experiments conducted by Google Quantum AI, IBM Quantum, and other quantum industry as recent classical shadow methods has been proposed to extract Renyi entropy in real quantum simulations via very few measurements [145, 146].

Bibliography

¹M. Wampler, B. J. J. Khor, G. Refael, and I. Klich, “Stirring by staring: measurement-induced chirality”, *Phys. Rev. X* **12**, 031031 (2022).

²B. J. J. Khor, M. Wampler, G. Refael, and I. Klich, “Measurement-induced chirality: diffusion and disorder”, *Phys. Rev. B* **108**, 214305 (2023).

³B. J. J. Khor, D. M. Kürkçüoğlu, T. J. Hobbs, G. N. Perdue, and I. Klich, “Confinement and Kink Entanglement Asymmetry on a Quantum Ising Chain”, *Quantum* **8**, 1462 (2024).

⁴M. Wampler, B. J. J. Khor, G. Refael, and I. Klich, “Stirring by staring: measurement-induced chirality”, *Phys. Rev. X* **12**, 031031 (2022).

⁵N. Swain, H. -. Tang, D. C. W. Foo, B. J. J. Khor, G. Lemarié, F. F. Assaad, P. Sengupta, and S. Adam, Engineering many-body quantum hamiltonians with non-ergodic properties using 2024.

⁶M. H. Anderson, J. R. Ensher, M. R. Matthews, C. E. Wieman, and E. A. Cornell, “Observation of bose-einstein condensation in a dilute atomic vapor”, *Science* **269**, 198–201 (1995).

⁷B. Keimer, S. A. Kivelson, M. R. Norman, S. Uchida, and J. Zaanen, “From quantum matter to high-temperature superconductivity in copper oxides”, *Nature* **518**, 179–186 (2015).

⁸X.-G. Wen, “Colloquium: zoo of quantum-topological phases of matter”, *Rev. Mod. Phys.* **89**, 041004 (2017).

- ⁹C. Nayak, S. H. Simon, A. Stern, M. Freedman, and S. Das Sarma, “Non-abelian anyons and topological quantum computation”, *Rev. Mod. Phys.* **80**, 1083–1159 (2008).
- ¹⁰G. Mahan, *Many-particle physics*, 3rd ed. (Springer, New York, NY, 2000).
- ¹¹I. Klich, “Closed hierarchies and non-equilibrium steady states of driven systems”, *Annals of Physics* **404**, 66–80 (2019).
- ¹²F. Ares, S. Murciano, and P. Calabrese, “Entanglement asymmetry as a probe of symmetry breaking”, *Nature Communications* **14**, 2036 (2023).
- ¹³U. Schollwöck, “The density-matrix renormalization group in the age of matrix product states”, *Annals of Physics* **326**, 96–192 (2011).
- ¹⁴R. Orús, “A practical introduction to tensor networks: matrix product states and projected entangled pair states”, *Annals of Physics* **349**, 117–158 (2014).
- ¹⁵A. Rivas and S. Huelga, *Open quantum systems: an introduction*, 1st ed. (Springer, Berlin, Heidelberg, 2012).
- ¹⁶J. Preskill, *Lecture notes on quantum information and computation*, <http://theory.caltech.edu/~preskill/ph229/>, [Online; accessed 11-April-2023], 2015.
- ¹⁷D. J. Gross and F. Wilczek, “Asymptotically free gauge theories. i”, *Phys. Rev. D* **8**, 3633–3652 (1973).
- ¹⁸F. Wilczek, “Nobel lecture: asymptotic freedom: from paradox to paradigm”, *Rev. Mod. Phys.* **77**, 857–870 (2005).
- ¹⁹D. J. Gross and F. Wilczek, “Ultraviolet behavior of non-abelian gauge theories”, *Phys. Rev. Lett.* **30**, 1343–1346 (1973).
- ²⁰J. Kogut and L. Susskind, “Hamiltonian formulation of wilson’s lattice gauge theories”, *Phys. Rev. D* **11**, 395–408 (1975).
- ²¹J. B. Kogut, “An introduction to lattice gauge theory and spin systems”, *Rev. Mod. Phys.* **51**, 659–713 (1979).

- ²²A. Kitaev, “Fault-tolerant quantum computation by anyons”, *Annals of Physics* **303**, 2–30 (2003).
- ²³M. Kormos, M. Collura, G. Takács, and P. Calabrese, “Real-time confinement following a quantum quench to a non-integrable model”, *Nature Physics* **13**, 246–249 (2017).
- ²⁴J. Vovrosh and J. Knolle, “Confinement and entanglement dynamics on a digital quantum computer”, *Sci. Rep.* **11**, 11577 (2021).
- ²⁵I. Klich and L. S. Levitov, Scaling of entanglement entropy and superselection rules, 2008.
- ²⁶M. A. Nielsen and I. L. Chuang, Quantum computation and quantum information: 10th anniversary (Cambridge University Press, 2011).
- ²⁷S. Murciano, F. Ares, I. Klich, and P. Calabrese, “Entanglement asymmetry and quantum mpemba effect in the xy spin chain”, *Journal of Statistical Mechanics: Theory and Experiment*, 013103 (2024).
- ²⁸L. K. Joshi, J. Franke, A. Rath, F. Ares, S. Murciano, F. Kranzl, R. Blatt, P. Zoller, B. Vermersch, P. Calabrese, C. F. Roos, and M. K. Joshi, “Observing the quantum mpemba effect in quantum simulations”, *Phys. Rev. Lett.* **133**, 010402 (2024).
- ²⁹M. S. Rudner, N. H. Lindner, E. Berg, and M. Levin, “Anomalous edge states and the bulk-edge correspondence for periodically driven two-dimensional systems”, *Physical Review X* **3**, 031005 (2013).
- ³⁰J. W. McIver, B. Schulte, F.-U. Stein, T. Matsuyama, G. Jotzu, G. Meier, and A. Cavalleri, “Light-induced anomalous hall effect in graphene”, *Nature Physics* **16**, 38–41 (2019).
- ³¹M. Nuske, L. Broers, B. Schulte, G. Jotzu, S. A. Sato, A. Cavalleri, A. Rubio, J. W. McIver, and L. Mathey, “Floquet dynamics in light-driven solids”, *Phys. Rev. Res.* **2**, 043408 (2020).

- ³²N. H. Lindner, G. Refael, and V. Galitski, “Floquet topological insulator in semiconductor quantum wells”, *Nature Physics* **7**, 490–495 (2011).
- ³³P. Titum, N. H. Lindner, M. C. Rechtsman, and G. Refael, “Disorder-induced floquet topological insulators”, *Phys. Rev. Lett.* **114**, 056801 (2015).
- ³⁴A. Kundu, M. Rudner, E. Berg, and N. H. Lindner, “Quantized large-bias current in the anomalous floquet-anderson insulator”, *Phys. Rev. B* **101**, 041403 (2020).
- ³⁵F. Nathan, D. Abanin, E. Berg, N. H. Lindner, and M. S. Rudner, “Anomalous floquet insulators”, *Phys. Rev. B* **99**, 195133 (2019).
- ³⁶H. C. Po, L. Fidkowski, T. Morimoto, A. C. Potter, and A. Vishwanath, “Chiral floquet phases of many-body localized bosons”, *Phys. Rev. X* **6**, 041070 (2016).
- ³⁷D. V. Else, C. Monroe, C. Nayak, and N. Y. Yao, “Discrete time crystals”, *Annual Review of Condensed Matter Physics* **11**, 467–499 (2020).
- ³⁸K. Wintersperger, C. Braun, F. N. Ünal, A. Eckardt, M. D. Liberto, N. Goldman, I. Bloch, and M. Aidelsburger, “Realization of an anomalous floquet topological system with ultracold atoms”, *Nature Physics* **16**, 1058–1063 (2020).
- ³⁹C. Braun, R. Saint-Jalm, A. Hesse, J. Arceri, I. Bloch, and M. Aidelsburger, “Real-space detection and manipulation of topological edge modes with ultracold atoms”, *Nature Physics* **20**, 1306–1312 (2024).
- ⁴⁰F. Nathan, D. A. Abanin, N. H. Lindner, E. Berg, and M. S. Rudner, “Hierarchy of many-body invariants and quantized magnetization in anomalous Floquet insulators”, *SciPost Phys.* **10**, 128 (2021).
- ⁴¹M. Wampler and I. Klich, “Arrested development and fragmentation in strongly-interacting floquet systems”, Accepted at Scipost: scipost_202210_00045v2 (2023).
- ⁴²M. Wampler and I. Klich, “Fragmentation and prethermal dynamical phases in disordered strongly interacting floquet systems”, *Phys. Rev. B* **108**, 104315 (2023).

- ⁴³U. Agrawal, A. Zabalo, K. Chen, J. H. Wilson, A. C. Potter, J. H. Pixley, S. Gopalakrishnan, and R. Vasseur, “Entanglement and charge-sharpening transitions in $u(1)$ symmetric monitored quantum circuits”, *Phys. Rev. X* **12**, 041002 (2022).
- ⁴⁴A. Biella and M. Schiró, “Many-Body Quantum Zeno Effect and Measurement-Induced Subradiance Transition”, *Quantum* **5**, 528 (2021).
- ⁴⁵M. Block, Y. Bao, S. Choi, E. Altman, and N. Y. Yao, “Measurement-induced transition in long-range interacting quantum circuits”, *Phys. Rev. Lett.* **128**, 010604 (2022).
- ⁴⁶A. Chan, R. M. Nandkishore, M. Pretko, and G. Smith, “Unitary-projective entanglement dynamics”, *Phys. Rev. B* **99**, 224307 (2019).
- ⁴⁷E. V. H. Doggen, Y. Gefen, I. V. Gornyi, A. D. Mirlin, and D. G. Polyakov, “Generalized quantum measurements with matrix product states: entanglement phase transition and clusterization”, *Phys. Rev. Res.* **4**, 023146 (2022).
- ⁴⁸M. Ippoliti, M. J. Gullans, S. Gopalakrishnan, D. A. Huse, and V. Khemani, “Entanglement phase transitions in measurement-only dynamics”, *Phys. Rev. X* **11**, 011030 (2021).
- ⁴⁹C.-M. Jian, Y.-Z. You, R. Vasseur, and A. W. W. Ludwig, “Measurement-induced criticality in random quantum circuits”, *Phys. Rev. B* **101**, 104302 (2020).
- ⁵⁰B. Ladewig, S. Diehl, and M. Buchhold, “Monitored open fermion dynamics: exploring the interplay of measurement, decoherence, and free hamiltonian evolution”, *Phys. Rev. Res.* **4**, 033001 (2022).
- ⁵¹Y. Li, X. Chen, and M. P. A. Fisher, “Quantum zeno effect and the many-body entanglement transition”, *Phys. Rev. B* **98**, 205136 (2018).
- ⁵²T.-C. Lu and T. Grover, “Spacetime duality between localization transitions and measurement-induced transitions”, *PRX Quantum* **2**, 040319 (2021).

- ⁵³O. Lunt, M. Szyniszewski, and A. Pal, “Measurement-induced criticality and entanglement clusters: a study of one-dimensional and two-dimensional clifford circuits”, *Phys. Rev. B* **104**, 155111 (2021).
- ⁵⁴T. Minato, K. Sugimoto, T. Kuwahara, and K. Saito, “Fate of measurement-induced phase transition in long-range interactions”, *Phys. Rev. Lett.* **128**, 010603 (2022).
- ⁵⁵Y. Minoguchi, P. Rabl, and M. Buchhold, “Continuous gaussian measurements of the free boson cft: a model for exactly solvable and detectable measurement-induced dynamics”, *SciPost Phys.* **12**, 009 (2022).
- ⁵⁶O. Shtanko, Y. A. Kharkov, L. P. Garcia-Pintos, and A. V. Gorshkov, “Classical models of entanglement in monitored random circuits”, arXiv preprint arXiv:2004.06736 (2020).
- ⁵⁷B. Skinner, J. Ruhman, and A. Nahum, “Measurement-induced phase transitions in the dynamics of entanglement”, *Phys. Rev. X* **9**, 031009 (2019).
- ⁵⁸M. Szyniszewski, A. Romito, and H. Schomerus, “Entanglement transition from variable-strength weak measurements”, *Phys. Rev. B* **100**, 064204 (2019).
- ⁵⁹P. Sierant, G. Chiriaco, F. M. Surace, S. Sharma, X. Turkeshi, M. Dalmonte, R. Fazio, and G. Pagano, “Dissipative Floquet Dynamics: from Steady State to Measurement Induced Criticality in Trapped-ion Chains”, *Quantum* **6**, 638 (2022).
- ⁶⁰X. Turkeshi, R. Fazio, and M. Dalmonte, “Measurement-induced criticality in $(2 + 1)$ -dimensional hybrid quantum circuits”, *Phys. Rev. B* **102**, 014315 (2020).
- ⁶¹A. Zabalo, M. J. Gullans, J. H. Wilson, S. Gopalakrishnan, D. A. Huse, and J. H. Pixley, “Critical properties of the measurement-induced transition in random quantum circuits”, *Phys. Rev. B* **101**, 060301 (2020).
- ⁶²M. P. Fisher, V. Khemani, A. Nahum, and S. Vijay, “Random quantum circuits”, *Annual Review of Condensed Matter Physics* **14**, 335–379 (2023).

- ⁶³O. Alberton, M. Buchhold, and S. Diehl, “Entanglement transition in a monitored free-fermion chain: from extended criticality to area law”, *Phys. Rev. Lett.* **126**, 170602 (2021).
- ⁶⁴M. Buchhold, Y. Minoguchi, A. Altland, and S. Diehl, “Effective theory for the measurement-induced phase transition of dirac fermions”, *Phys. Rev. X* **11**, 041004 (2021).
- ⁶⁵X. Cao, A. Tilloy, and A. D. Luca, “Entanglement in a fermion chain under continuous monitoring”, *SciPost Phys.* **7**, 024 (2019).
- ⁶⁶X. Chen, Y. Li, M. P. A. Fisher, and A. Lucas, “Emergent conformal symmetry in nonunitary random dynamics of free fermions”, *Phys. Rev. Res.* **2**, 033017 (2020).
- ⁶⁷L. Fidkowski, J. Haah, and M. B. Hastings, “How dynamical quantum memories forget”, *Quantum* **5**, 382 (2021).
- ⁶⁸G. Kells, D. Meidan, and A. Romito, “Topological transitions in weakly monitored free fermions”, *SciPost Phys.* **14**, 031 (2023).
- ⁶⁹M. Szytniszewski, O. Lunt, and A. Pal, “Disordered monitored free fermions”, *Phys. Rev. B* **108**, 165126 (2023).
- ⁷⁰J. Merritt and L. Fidkowski, “Entanglement transitions with free fermions”, *Phys. Rev. B* **107**, 064303 (2023).
- ⁷¹Q. Yang, Y. Zuo, and D. E. Liu, “Keldysh nonlinear sigma model for a free-fermion gas under continuous measurements”, *Phys. Rev. Res.* **5**, 033174 (2023).
- ⁷²P. Pöpperl, I. V. Gornyi, and Y. Gefen, “Measurements on an anderson chain”, *Phys. Rev. B* **107**, 174203 (2023).
- ⁷³E. P. Yamaguchi, H. M. Hurst, and I. B. Spielman, “Feedback-cooled bose-einstein condensation: near and far from equilibrium”, *Phys. Rev. A* **107**, 063306 (2023).
- ⁷⁴S. J. Garratt, Z. Weinstein, and E. Altman, “Measurements conspire nonlocally to restructure critical quantum states”, *Phys. Rev. X* **13**, 021026 (2023).

- ⁷⁵D. Ristè, M. Dukalski, C. A. Watson, G. de Lange, M. J. Tiggelman, Y. M. Blanter, K. W. Lehnert, R. N. Schouten, and L. DiCarlo, “Deterministic entanglement of superconducting qubits by parity measurement and feedback”, *Nature* **502**, 350–354 (2013).
- ⁷⁶S. Roy, J. T. Chalker, I. V. Gornyi, and Y. Gefen, “Measurement-induced steering of quantum systems”, *Phys. Rev. Res.* **2**, 033347 (2020).
- ⁷⁷S. Trugman, “Localization, percolation, and the quantum hall effect”, *Physical Review B* **27**, 7539 (1983).
- ⁷⁸J. T. Chalker and P. D. Coddington, “Percolation, quantum tunnelling and the integer hall effect”, *Journal of Physics C: Solid State Physics* **21**, 2665–2679 (1988).
- ⁷⁹M. Wampler, P. Schauss, E. B. Kolomeisky, and I. Klich, “Quantum wakes in lattice fermions”, *Phys. Rev. Res.* **3**, 033112 (2021).
- ⁸⁰W. S. Oliveira, J. P. de Lima, N. C. Costa, and R. R. dos Santos, “Percolation on lieb lattices”, *Phys. Rev. E* **104**, 064122 (2021).
- ⁸¹D. Stauffer and A. Aharony, *Introduction to percolation theory* (Taylor and Francis, London, 1994).
- ⁸²Y. Gefen, A. Aharony, and S. Alexander, “Anomalous diffusion on percolating clusters”, *Phys. Rev. Lett.* **50**, 77–80 (1983).
- ⁸³L. Levi, T. Schwartz, M. Segev, and S. Fishman, “Breakdown of anderson localization due to dynamic disorder”, *2009 Conference on Lasers and Electro-Optics and 2009 Conference on Quantum electronics and Laser Science Conference*, 1–2 (2009).
- ⁸⁴A. Didi and E. Barkai, “Measurement-induced quantum walks”, *Phys. Rev. E* **105**, 054108 (2022).
- ⁸⁵S. Tornow and K. Ziegler, “Measurement-induced quantum walks on an ibm quantum computer”, *Phys. Rev. Res.* **5**, 033089 (2023).
- ⁸⁶K. G. Wilson, “Confinement of quarks”, *Phys. Rev. D* **10**, 2445–2459 (1974).

- ⁸⁷D. E. Kharzeev and E. M. Levin, “Deep inelastic scattering as a probe of entanglement”, *Phys. Rev. D* **95**, 114008 (2017).
- ⁸⁸H. Lamm, S. Lawrence, and Y. Yamauchi (NuQS Collaboration), “Parton physics on a quantum computer”, *Phys. Rev. Res.* **2**, 013272 (2020).
- ⁸⁹P. J. Ehlers, “Entanglement between valence and sea quarks in hadrons of 1+1 dimensional QCD”, *Annals Phys.* **452**, 169290 (2023).
- ⁹⁰A. Cervera-Lierta, J. I. Latorre, J. Rojo, and L. Rottoli, “Maximal Entanglement in High Energy Physics”, *SciPost Phys.* **3**, 036 (2017).
- ⁹¹S. R. Beane, D. B. Kaplan, N. Klco, and M. J. Savage, “Entanglement suppression and emergent symmetries of strong interactions”, *Phys. Rev. Lett.* **122**, 102001 (2019).
- ⁹²Y. Afik and J. R. M. de Nova, “Entanglement and quantum tomography with top quarks at the LHC”, *The European Physical Journal Plus* **136**, 907 (2021).
- ⁹³Q. Liu, I. Low, and T. Mehen, “Minimal entanglement and emergent symmetries in low-energy qcd”, *Phys. Rev. C* **107**, 025204 (2023).
- ⁹⁴M. Carena, I. Low, C. E. M. Wagner, and M.-L. Xiao, Entanglement Suppression, Enhanced Symmetry, July 2023.
- ⁹⁵B. M. McCoy and T. T. Wu, “Two-dimensional ising field theory in a magnetic field: breakup of the cut in the two-point function”, *Phys. Rev. D* **18**, 1259–1267 (1978).
- ⁹⁶G. Delfino, G. Mussardo, and P. Simonetti, “Non-integrable quantum field theories as perturbations of certain integrable models”, *Nuclear Physics B* **473**, 469–508 (1996).
- ⁹⁷S. B. Rutkevich, “Decay of the metastable phase in $d = 1$ and $d = 2$ ising models”, *Phys. Rev. B* **60**, 14525–14528 (1999).
- ⁹⁸M. Bhaseen and A. Tsvetik, “Aspects of confinement in low dimensions”, *From Fields to Strings: Circumnavigating Theoretical Physics: Ian Kogan Memorial Collection (In 3 Volumes)*, 661–683 (2005).

- ⁹⁹S. Rutkevich, “Energy spectrum of bound-spinons in the quantum ising spin-chain ferromagnet”, *Journal of Statistical Physics* **131**, 917–939 (2008).
- ¹⁰⁰N. Ranabhat, A. Santini, E. Tirrito, and M. Collura, Dynamical deconfinement transition driven by de 2023.
- ¹⁰¹R. Coldea, D. Tennant, E. Wheeler, E. Wawrzynska, D. Prabhakaran, M. Telling, K. Habicht, P. Smeibidl, and K. Kiefer, “Quantum criticality in an ising chain: experimental evidence for emergent e_8 symmetry”, *Science* **327**, 177–180 (2010).
- ¹⁰²Z. Zhang, K. Amelin, X. Wang, H. Zou, J. Yang, U. Nagel, T. Rööm, T. Dey, A. A. Nugroho, T. Lorenz, J. Wu, and Z. Wang, “Observation of E_8 particles in an ising chain antiferromagnet”, *Phys. Rev. B* **101**, 220411 (2020).
- ¹⁰³H. Zou, Y. Cui, X. Wang, Z. Zhang, J. Yang, G. Xu, A. Okutani, M. Hagiwara, M. Matsuda, G. Wang, G. Mussardo, K. Hódsági, M. Kormos, Z. He, S. Kimura, R. Yu, W. Yu, J. Ma, and J. Wu, “ E_8 spectra of quasi-one-dimensional antiferromagnet $\text{BaCo}_2\text{V}_2\text{O}_8$ under transverse field”, *Phys. Rev. Lett.* **127**, 077201 (2021).
- ¹⁰⁴A. J. A. James, R. M. Konik, and N. J. Robinson, “Nonthermal states arising from confinement in one and two dimensions”, *Phys. Rev. Lett.* **122**, 130603 (2019).
- ¹⁰⁵N. J. Robinson, A. J. A. James, and R. M. Konik, “Signatures of rare states and thermalization in a theory with confinement”, *Phys. Rev. B* **99**, 195108 (2019).
- ¹⁰⁶F. Liu, R. Lundgren, P. Titum, G. Pagano, J. Zhang, C. Monroe, and A. V. Gorshkov, “Confined quasiparticle dynamics in long-range interacting quantum spin chains”, *Phys. Rev. Lett.* **122**, 150601 (2019).
- ¹⁰⁷R. Verdel, F. Liu, S. Whitsitt, A. V. Gorshkov, and M. Heyl, “Real-time dynamics of string breaking in quantum spin chains”, *Phys. Rev. B* **102**, 014308 (2020).
- ¹⁰⁸R. Verdel, G.-Y. Zhu, and M. Heyl, “Dynamical localization transition of string breaking in quantum spin chains”, *Phys. Rev. Lett.* **131**, 230402 (2023).

- ¹⁰⁹S. Scopa, P. Calabrese, and A. Bastianello, “Entanglement dynamics in confining spin chains”, *Phys. Rev. B* **105**, 125413 (2022).
- ¹¹⁰O. A. Castro-Alvaredo, M. Lencsés, I. M. Szécsényi, and J. Viti, “Entanglement oscillations near a quantum critical point”, *Phys. Rev. Lett.* **124**, 230601 (2020).
- ¹¹¹A. Milsted, J. Liu, J. Preskill, and G. Vidal, “Collisions of false-vacuum bubble walls in a quantum spin chain”, *PRX Quantum* **3**, 020316 (2022).
- ¹¹²P. P. Mazza, G. Perfetto, A. Lerose, M. Collura, and A. Gambassi, “Suppression of transport in nondisordered quantum spin chains due to confined excitations”, *Phys. Rev. B* **99**, 180302 (2019).
- ¹¹³A. Bastianello, U. Borla, and S. Moroz, “Fragmentation and emergent integrable transport in the weakly tilted ising chain”, *Phys. Rev. Lett.* **128**, 196601 (2022).
- ¹¹⁴A. Lerose, F. M. Surace, P. P. Mazza, G. Perfetto, M. Collura, and A. Gambassi, “Quasilo- calized dynamics from confinement of quantum excitations”, *Phys. Rev. B* **102**, 041118 (2020).
- ¹¹⁵P. I. Karpov, G.-Y. Zhu, M. P. Heller, and M. Heyl, “Spatiotemporal dynamics of particle collisions in quantum spin chains”, *Phys. Rev. Res.* **4**, L032001 (2022).
- ¹¹⁶O. Pomponio, M. A. Werner, G. Zarand, and G. Takacs, “Bloch oscillations and the lack of the decay of the false vacuum in a one-dimensional quantum spin chain”, *SciPost Phys.* **12**, 061 (2022).
- ¹¹⁷G. Lagnese, F. M. Surace, M. Kormos, and P. Calabrese, “False vacuum decay in quantum spin chains”, *Phys. Rev. B* **104**, L201106 (2021).
- ¹¹⁸G. Lagnese, F. M. Surace, S. Morampudi, and F. Wilczek, Detecting a long lived false vacuum with 2023.
- ¹¹⁹J. Knaute, M. Feuerstein, and E. Zohar, “Entanglement and confinement in lattice gauge theory tensor networks”, *Journal of High Energy Physics* **2024**, 174 (2024).

- ¹²⁰A. Sopena, M. H. Gordon, G. Sierra, and E. López, “Simulating quench dynamics on a digital quantum computer with data-driven error mitigation”, *Quantum Science and Technology* **6**, 045003 (2021).
- ¹²¹D. Dasenbrook and C. Flindt, “Dynamical generation and detection of entanglement in neutral leviton pairs”, *Phys. Rev. B* **92**, 161412 (2015).
- ¹²²H. Barghathi, C. M. Herdman, and A. Del Maestro, “Rényi generalization of the accessible entanglement entropy”, *Phys. Rev. Lett.* **121**, 150501 (2018).
- ¹²³F. Ares, S. Murciano, E. Vernier, and P. Calabrese, “Lack of symmetry restoration after a quantum quench: An entanglement asymmetry study”, *SciPost Phys.* **15**, 089 (2023).
- ¹²⁴F. Ferro, F. Ares, and P. Calabrese, “Non-equilibrium entanglement asymmetry for discrete groups: the example of the xy spin chain”, *Journal of Statistical Mechanics: Theory and Experiment* **2024**, 023101 (2024).
- ¹²⁵L. Capizzi and M. Mazzoni, “Entanglement asymmetry in the ordered phase of many-body systems: the Ising field theory”, *Journal of High Energy Physics* **2023**, 144 (2023).
- ¹²⁶V. Vitale, A. Elben, R. Kueng, A. Neven, J. Carrasco, B. Kraus, P. Zoller, P. Calabrese, B. Vermersch, and M. Dalmonte, “Symmetry-resolved dynamical purification in synthetic quantum matter”, *SciPost Phys.* **12**, 106 (2022).
- ¹²⁷A. Rath, V. Vitale, S. Murciano, M. Votto, J. Dubail, R. Kueng, C. Branciard, P. Calabrese, and B. Vermersch, “Entanglement barrier and its symmetry resolution: theory and experimental observation”, *PRX Quantum* **4**, 010318 (2023).
- ¹²⁸M. Goldstein and E. Sela, “Symmetry-resolved entanglement in many-body systems”, *Phys. Rev. Lett.* **120**, 200602 (2018).
- ¹²⁹S. Murciano, P. Calabrese, and L. Piroli, “Symmetry-resolved page curves”, *Phys. Rev. D* **106**, 046015 (2022).

- ¹³⁰S. Murciano, G. Di Giulio, and P. Calabrese, “Entanglement and symmetry resolution in two dimensional free quantum field theories”, *Journal of High Energy Physics* **2020**, 73 (2020).
- ¹³¹R. Bonsignori, P. Ruggiero, and P. Calabrese, “Symmetry resolved entanglement in free fermionic systems”, *Journal of Physics A: Mathematical and Theoretical* **52**, 475302 (2019).
- ¹³²A. Neven, J. Carrasco, V. Vitale, C. Kokail, A. Elben, M. Dalmonte, P. Calabrese, P. Zoller, B. Vermersch, R. Kueng, and B. Kraus, “Symmetry-resolved entanglement detection using partial transpose moments”, *npj Quantum Information* **7**, 152 (2021).
- ¹³³Z.-Y. Ge, Y.-R. Zhang, and F. Nori, “Nonmesonic quantum many-body scars in a 1d lattice gauge theory”, *Phys. Rev. Lett.* **132**, 230403 (2024).
- ¹³⁴T. Iadecola and M. Schechter, “Quantum many-body scar states with emergent kinetic constraints and finite-entanglement revivals”, *Phys. Rev. B* **101**, 024306 (2020).
- ¹³⁵J. Vovrosh, R. Mukherjee, A. Bastianello, and J. Knolle, “Dynamical hadron formation in long-range interacting quantum spin chains”, *PRX Quantum* **3**, 040309 (2022).
- ¹³⁶U. Borla, R. Verresen, F. Grusdt, and S. Moroz, “Confined phases of one-dimensional spinless fermions coupled to Z_2 gauge theory”, *Phys. Rev. Lett.* **124**, 120503 (2020).
- ¹³⁷E. J. Gustafson, A. C. Y. Li, A. Khan, J. Kim, D. M. Kurkcuoglu, M. S. Alam, P. P. Orth, A. Rahmani, and T. Iadecola, “Preparing quantum many-body scar states on quantum computers”, *Quantum* **7**, 1171 (2023).
- ¹³⁸M. Ostmann, M. Marcuzzi, J. P. Garrahan, and I. Lesanovsky, “Localization in spin chains with facilitation constraints and disordered interactions”, *Phys. Rev. A* **99**, 060101 (2019).
- ¹³⁹S. R. White and A. E. Feiguin, “Real-time evolution using the density matrix renormalization group”, *Phys. Rev. Lett.* **93**, 076401 (2004).

-
- ¹⁴⁰G. Vidal, “Efficient simulation of one-dimensional quantum many-body systems”, *Phys. Rev. Lett.* **93**, 040502 (2004).
- ¹⁴¹F. Verstraete, J. J. García-Ripoll, and J. I. Cirac, “Matrix product density operators: simulation of finite-temperature and dissipative systems”, *Phys. Rev. Lett.* **93**, 207204 (2004).
- ¹⁴²B. Bertini, K. Klobas, M. Collura, P. Calabrese, and C. Rylands, “Dynamics of charge fluctuations from asymmetric initial states”, *Phys. Rev. B* **109**, 184312 (2024).
- ¹⁴³L. Capizzi and V. Vitale, A universal formula for the entanglement asymmetry of matrix product states, 2024.
- ¹⁴⁴N. Feldman, A. Kshetrimayum, J. Eisert, and M. Goldstein, “Entanglement estimation in tensor network states via sampling”, *PRX Quantum* **3**, 030312 (2022).
- ¹⁴⁵T. Brydges, A. Elben, P. Jurcevic, B. Vermersch, C. Maier, B. P. Lanyon, P. Zoller, R. Blatt, and C. F. Roos, “Probing rényi entanglement entropy via randomized measurements”, *Science* **364**, 260–263 (2019).
- ¹⁴⁶H.-Y. Huang, R. Kueng, and J. Preskill, “Predicting many properties of a quantum system from very few measurements”, *Nature Physics* **16**, 1050–1057 (2020).